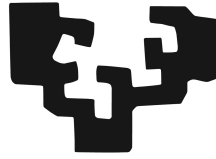


eman ta zabal zazu



Universidad  
del País Vasco

Euskal Herriko  
Unibertsitatea

PhD Thesis

# **Vapour Phase Modification of Kevlar Fibres**

Itxasne Azpitarte Iraculis

Supervised by Prof. Mato Knez

2018



This PhD thesis has been carried out at:



CIC nanoGUNE

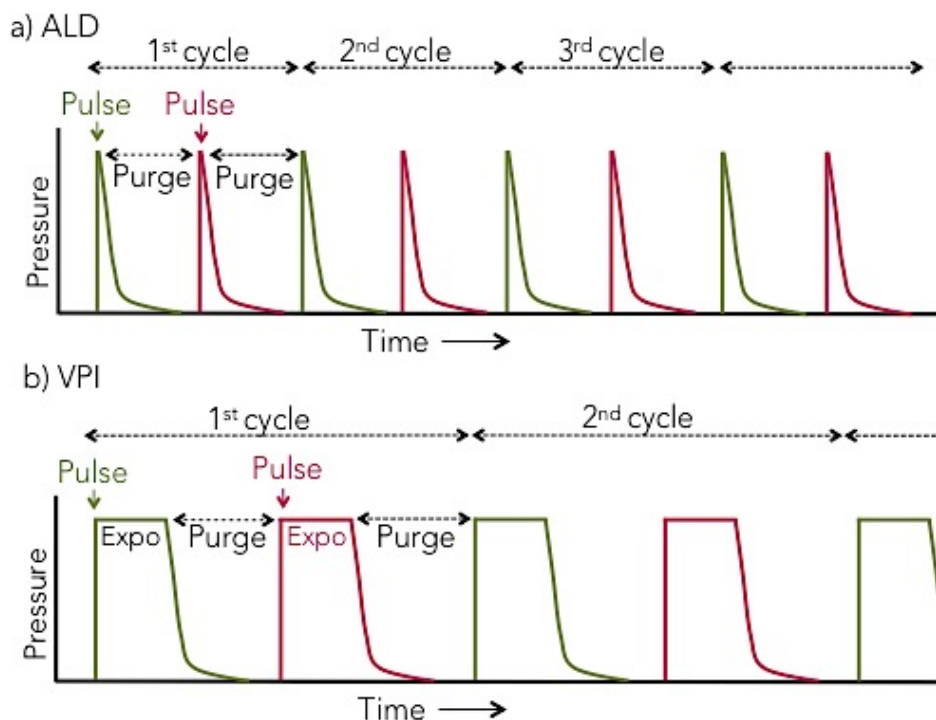
Nanomaterials group

Donostia, Spain



## Laburpena

Natura beti izan da inspirazio iturri izakiarentzat eta, batez ere, material zientzialarientzat. Milioika urtetan zehar, naturak estrategia ezberdinak garatu ditu biomaterialak behar espezifikoetara moldatzeko. Estrategia horien artean, frakzio inorganikoak matrize organikoetan tartekatzeak funtsezko rola betetzen du biomaterial askoren jarduera onean. Material hibrido organiko-inorganiko hauek, zientzialarien arreta bereganatu dute azken urtetan. Material hibridoek ezaugarri bereziak dituzte, material organikoen (polimeroak) eta inorganikoen (metalak eta zeramikoak) arteko tarte betez. Material hibridoak sintetizatzeke erabiltzen diren estrategia gehienak fase likidoan ematen dira. Estrategia horiek desabantaila ugari dituzte, disolbatzaile hondarrak kentzeko sintesi osteko prozesuen beharra adibidez. Fase gaseosoan gertatzen diren estrategiak, material hibridoen sintesirako aukera egokia direla frogatu dute. Vapour Phase Infiltration (VPI), Atomic Layer Deposition (ALD) teknikaren eraldaketa dena, modu arrakastatsuan erabili da oxido metalikoak matrize polimerikoetan infiltratzeko, horrela material hibridoak sortuz. Ikuspegi honen helburu nagusia materialen propietate mekanikoak hobetzea zen. Hala ere, polimeroak oxido metalikoekin hibridatzea beste hainbat propietate eraldatzeko gai dela frogatu da beranduago aurkeztutako lanetan.

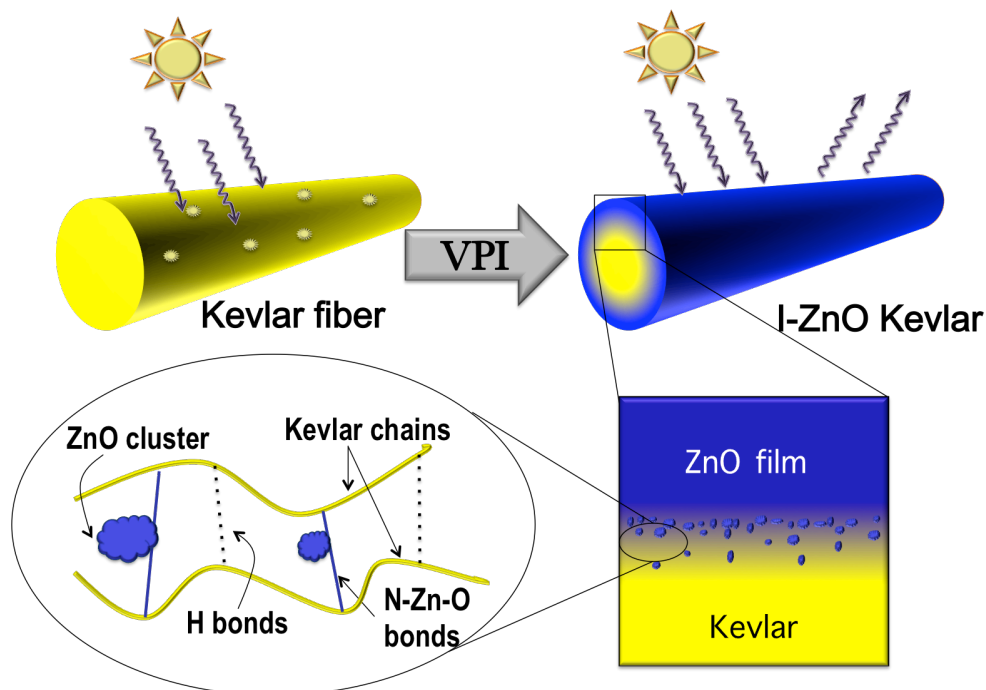


a) Atomic Layer Deposition (ALD) eta b) Vapor Phase Infiltration (VPI) tekniken harteko presio profilaren ezberdintasuna. VPI-an, prekursoreren pulsoaren eta erreaktorearen purgaren artean gehitzen den esposizio denborari esker, substratuak estaltzeaz gain infiltratu ere egiten dira.

Erresistentzia handiko polimeroak, Kevlar-a adibidez, hautagai ezin-hobeak dira fase gaseosoan oxido metalikoekin hibridatzeko. Polimero hauen egitura kristalino ordenatuak, aurkezten dituzten propietate berezien iturria izan arren, sintesi ondoko funtzionalizazioa asko zailtzen du. Hala ere, erresistentzia altuko polimero gehienak argi ultra-bioleta eta tenperatura altuekiko oso sentikorrek dira eta degradazioa ekiditeko babestu egin behar dira. Orain arte erabilitako estrategiak (polimeroak oxido metaliko edo erresina batekin estalduz) polimeroaren ahultzea bezalako desabantailak dakartza.

Tesi honen lehen zatian Kevlar zuntzen hibridazioa ZnO-rekin, VPI erabiliz, aurkezten da. Infiltrazio prozesua 200 ziklo errepikatuz eta 150 °C-tan egiten da, dietilzink eta ura prekursorere moduan erabilia. Hibridazio prozesuaren ondorioz, Kevlar-ZnO material hibrido bat sortzen da zuntzen gainazaletik gertu. Material hibridoaren egitura, ZnO klusterrak kobalenteki lotutako Kevlar kateen artean, teorikoki aurrean eta esperimentalki karakterizatzen da. Jatorrizko hidrogeno

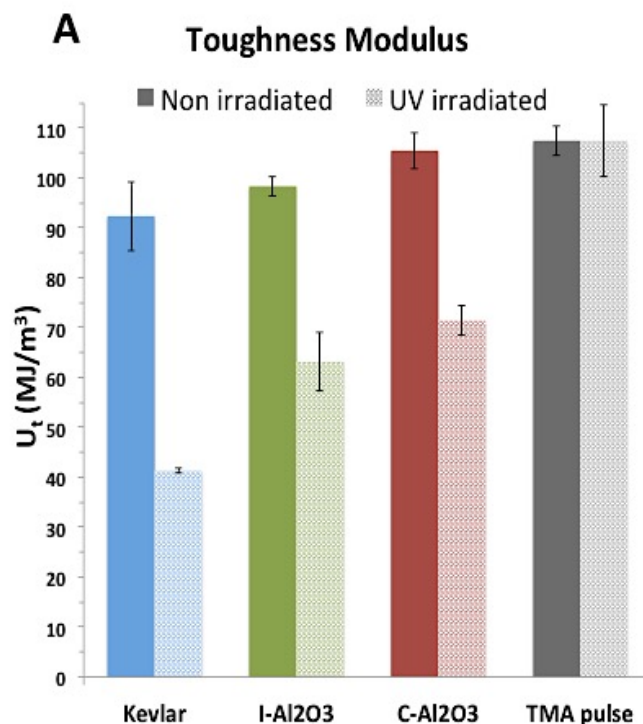
zubiak N-Zn-O lotura kobalenteekin ordezkatzean zuntz infiltratuek degradazio temperaturan 8 °C-ko igoera erakusten dute. Gainera, zuntzen propietate mekanikoak eta UV sentikortasuna ere neurtzen dira. Zuntz infiltratuek Kevlar-aren propietate mekanikoen %90-a mantentzen dute. Tratatu gabeko Kevlar zuntzak UV argipean jarri ondoren propietate mekanikoen %50-a galtzen dute. ZnO-az estalitako zuntzak, konparatzeko prestatutakoak, argi ultra-bioletarekiko sentikortasun handiagoa erakusten dute, ZnO filmaren propietate foto-katalitikoek ondorioz. Hala ere, ZnO infiltratutako zuntzek ez dute inolako degradaziorik erakusten UV argiarekin erradiatu ondoren. Beraz, Kevlar zuntzak ZnO-az hibridatzearen ondorioz, polimeroaren egonkortasuna handitu dela frogatzen da.



Kevlar zuntz polimerikoak VPI erabiliz zink oxidoaz infiltratzean, beraien propietate termikoak hobetu eta argi ultravioletarekiko erresistentzia handitzen da.

Tesi honen bigarren zatian ALD/VPI prozesu konbinatu berri bat aurkezten da, aurreko atalean lortutako emaitzak hobetzeko. ALD/VPI prozesu konbinatu honekin, substratu polimeriko bat oxido metaliko batekin estali daiteke beste oxido metaliko ezberdin batekin infiltratzen den prozesu berean. Kasu honetan, Kevlar zuntzak  $\text{Al}_2\text{O}_3$ -rekin estali eta ZnO-az infiltratu dira. Zuntzak  $\text{Al}_2\text{O}_3$ -rekin estaltzean propietate mekanikoak %10-ean hobetzen dira eta ZnO infiltratzean UV argiarekiko

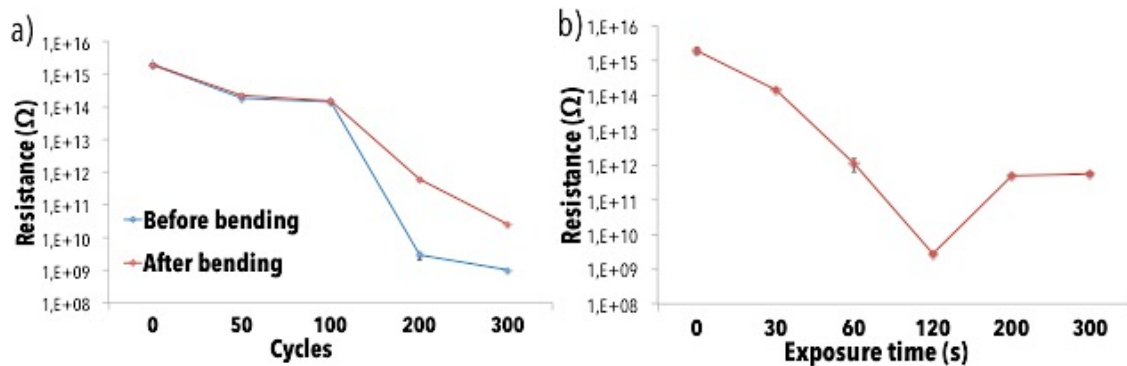
sentikortasuna ezabatzen da. Beraz, UV argia jasaten duten eta propietate mekaniko hobeak dituzten Kevlar zuntzak sortu dira.



Kevlar zuntzak zink oxidoaz infiltratuz gain aluminio oxidoaz estaltzean, argi ultravioletarekiko erresistentzia handitzeaz gain zuntzen irmotasuna %17an hobetzen da

Tesi honen azken zatian ZnO infiltrazioak Kevlar-aren propietate elektronikoetan duen eragina aztertu da. ZnOa infiltratu ondoren, DFT kalkulu teorikoek Kevlar-aren eraztun bentzenikoak eraztun kinoide bihurtuko direla aurrean dute, energia tarte elektronikoa txikituz. Eraztun aromatikoaren konbertsioa nano-FTIR teknikaz aztertzen da eta energia tartearen txikitzea UV-Vis espektroskopiaz. Tarte elektronikoaren txikitzeak konduktibitate elektrikoaren handitzea dakar, zuntzak tolestu eta estalduraren kontribuzioa ezabatu ondoren mantentzen dena. Zuntz hibridoaren konduktibitatea infiltrazio ziklo kopuruaren eta esposizio denboraren arabera kontrolatu daiteke. Gainera, zuntzak argi ikusgai argizatzean foto korrontearen sorrera ere aztertzen da. Bukatzeko, ZnO-az infiltratutako Kevlar zuntzek propietate foto-katalitikoak aurkezten dituzte argi ikusgai argizatzean, tarte elektronikoaren txikitzea konfirmatuz. Aktibitate foto-

katalitiko, infiltrazio ziklo kopuruarekin aldatzen dena, Rodamina B molekularen degradazioa jarraituz aztertzen da.



a) Zink oxidoaz infiltratutako Kevlar zuntzen erresistentzia elektrikoaren dependentzia infiltrazio ziklo kopuraren arabera b) Zuntz hibridoaren erresistentzia elektrikoaren dependentzia esposizio denboraren arabera



## Abstract

Nature has always been a great source of inspiration for the human being in general and for material scientists in particular. Over millions of years of evolution, nature has developed different strategies to adapt the properties of biomaterials to different specific needs. Among these strategies, the intercalation of inorganic fractions into organic matrices plays a critical role in the performance of many biomaterials. These hybrid organic-inorganic materials have attracted researchers interest over the past years. Hybrid materials present unique properties, bridging the gap between the organic materials (such as polymers) and inorganics (metals and ceramics). Most of the existing approaches for the synthesis of hybrid materials are carried out in liquid phase, which has some drawbacks such as the need of post processing treatments for the elimination of the residual solvent. The vapour phase approaches have demonstrated to be an efficient and reliable alternative for the synthesis of hybrid materials. Vapour Phase Infiltration (VPI), a modification of Atomic Layer Deposition (ALD), has been successfully used for the infiltration of metal oxides into polymeric matrices, thus creating hybrid materials. The initial target of this approach was the improvement of the mechanical properties. However, it has later been demonstrated that the hybridization of polymers with metal oxides leads to the modification of many other properties.

Among others, high strength polymers, such as Kevlar, are great candidates for the vapour phase hybridization with a metal oxide. These polymers have a highly ordered crystalline structure, which is responsible for their outstanding properties. This makes their post synthetic functionalization difficult. However, high strength polymers are extremely sensitive to UV and high temperatures, so they need to be protected. Coating the polymeric fibres with a resin or a metal oxide, which is the so far used strategy, shows several drawbacks such as induced brittleness of the polymer and possible detachment of the coating.

In the first part of this thesis, the hybridization of Kevlar fibres with ZnO through VPI is studied and compared to ZnO ALD coated fibres. The VPI process is

carried out with 200 deposition cycles at 150 °C, using diethylzinc and water as precursors. As a consequence of the hybridization, a hybrid Kevlar-ZnO material is created in the subsurface area of the fibres. The structure of this hybrid material is theoretically and experimentally characterized, consisting of ZnO clusters grown among covalently cross-linked Kevlar chains. Thanks to the substitution of the original hydrogen bonds by N-Zn-O bonds, the infiltrated fibres show an increase of 8 °C in their degradation temperature. Besides, the mechanical properties of the fibres are tested together with their stability against UV irradiation. The infiltrated fibres maintain 90% of the modulus of toughness of untreated Kevlar. When exposed to UV light, the untreated Kevlar fibres lose more than 50% of their toughness. The ZnO coated fibres, prepared for comparison, suffer an enhanced photodegradation when exposed to UV light as a consequence of the photocatalytic activity of the ZnO film deposited on the surface of the polymer. However, the ZnO infiltrated fibres do not show any degradation of their mechanical properties after being irradiated with UV light. Therefore, it is demonstrated that thanks to the hybridization of Kevlar fibres with ZnO through VPI the thermal and UV stability of the polymer is enhanced.

In the second part of this thesis a new ALD/VPI combined process is used for the optimization of the results presented in the previous part. With this combined ALD/VPI process a polymeric substrate can be coated with a metal oxide and infiltrated with a different metal oxide within a single process. In this case, Kevlar fibres coated with Al<sub>2</sub>O<sub>3</sub> and infiltrated with ZnO are prepared and studied. The Al<sub>2</sub>O<sub>3</sub> coating resulted in the enhancement of the modulus of toughness by 10%, while the ZnO-Kevlar hybrid created in the subsurface area suppressed the UV sensitivity of the fibres. Thus, Kevlar fibres with an enhanced modulus of toughness and UV radiation resistance are created.

In the last part of this thesis, the effect of the ZnO infiltration on the electronic properties of Kevlar is analysed. Theoretical DFT calculations predict a conversion of the benzenoid rings of Kevlar to quinoid rings resulting in a shift of the energy band gap towards lower energies. The change in the ring structures is experimentally proven by nano-FTIR and the band gap shift by UV-Vis spectroscopy. The shift in

the band gap results in enhanced electrical conductivity of the ZnO infiltrated fibres, which is maintained even after bending the fibres and removal of the contribution from the coating to the conductivity. The conductivity of the hybrid fibres can be tuned by changing the exposure time or the number of infiltration cycles. However, in both cases a threshold value has to be overcome to observe a significant improvement. Moreover, the generation of photocurrent when illuminating the hybrid fibres with visible light is also studied. Finally, the ZnO infiltrated Kevlar fibres show also photocatalytic activity when illuminated with visible light, further confirming the shift of the electronic band gap with the creation of the hybrid material. The photocatalytic activity, which is tuneable with the number of infiltration cycles, is studied by following the degradation of Rhodamine B.



## Contents

<b>Laburpena</b>	<b>I</b>
<b>Abstract</b>	<b>VII</b>
<b>Chapter 1</b>	<b>1</b>
<b>Introduction</b>	<b>1</b>
<b>1.1.- Background</b>	<b>1</b>
<b>1.2.- Atomic Layer Deposition</b>	<b>6</b>
<b>1.3.- Vapour Phase Infiltration (VPI)</b>	<b>10</b>
<b>1.4.- Kevlar®</b>	<b>15</b>
<b>1.5.- Objective and structure of the thesis</b>	<b>19</b>
<b>Chapter 2</b>	<b>21</b>
<b>Experimental techniques and methods</b>	<b>21</b>
<b>2.1.- Fourier Transform Infrared Spectroscopy (FTIR)</b>	<b>21</b>
2.1.1.- Attenuated total reflectance FTIR (ATR-FTIR)	21
2.1.2.- Fourier transform infrared nanospectroscopy (nano-FTIR)	22
<b>2.2.- Electron microscopy</b>	<b>24</b>
2.2.1.- Scanning electron microscopy (SEM)	24
2.2.2.- Transmission electron microscopy (TEM)	25
2.2.3.- Energy-dispersive X-ray spectroscopy (EDS)	25
<b>2.3.- X-ray diffractometry (XRD)</b>	<b>25</b>
<b>2.4.- Uniaxial tensile tests</b>	<b>26</b>
<b>Chapter 3</b>	<b>29</b>
<b>Improving Kevlar's stability through vapour phase infiltration of ZnO</b>	<b>29</b>
<b>3.1.- Introduction</b>	<b>31</b>
<b>3.2.- Experimental</b>	<b>32</b>
3.2.1.- Sample preparation	32
3.2.2.- Characterization	32
<b>3.3.- Results and discussion</b>	<b>34</b>
<b>3.4.- Conclusions</b>	<b>45</b>

<b>Chapter 4</b>	<b>47</b>
<b>Combined ALD/VPI process for multiscale functionalization of Kevlar</b>	<b>47</b>
<b>4.1.- Introduction</b>	<b>49</b>
<b>4.2.- Experimental</b>	<b>49</b>
4.2.1.-Sample preparation	49
4.2.2.- Characterization	50
<b>4.3.- Results and discussion</b>	<b>51</b>
<b>4.4. Conclusions</b>	<b>60</b>
<b>Chapter 5</b>	<b>61</b>
<b>Development and characterization of a Kevlar-ZnO hybrid conductive photocatalyst</b>	<b>61</b>
<b>5.1.- Introduction</b>	<b>61</b>
<b>5.2.- Experimental</b>	<b>63</b>
5.5.1.- Sample preparation	63
5.2.2.- Computational simulations	64
5.2.3.- Spectroscopic analysis	64
5.2.4- Electrical resistance measurements	65
5.2.5.- Photocatalytic activity study	65
<b>5.3.- Results and discussion</b>	<b>67</b>
5.3.1.- Band gap engineering through VPI	67
5.3.2.- Tuning the resistance of the Kevlar-ZnO hybrid	73
5.3.3.- Photoconductivity	78
5.3.4.- Photocatalytic activity	80
<b>5.4.- Conclusions</b>	<b>82</b>
<b>Chapter 6</b>	<b>85</b>
<b>Summary and outlook</b>	<b>85</b>
<b>Bibliography</b>	<b>87</b>
<b>List of publications</b>	<b>101</b>
<b>Acknowledgements</b>	<b>103</b>

“I was working with these very long-chain, where you had a lot of benzene rings in them. It was very strong and very stiff, unlike anything we had made before. I knew that I had made a discovery. I didn’t shout “Eureka!” but I was very excited, as was the whole laboratory excited, because we were looking for something new. Something different. And this was it.”

**Stephanie Kwolek**

“Basically, I have been compelled by curiosity.”

**Mary Leakey**



# Chapter 1

## Introduction

### 1.1.- Background

Nature has always been a source of inspiration for materials scientists. Driven by the need of living organisms to adapt to various and changing environments, biomaterials have been incrementally optimized over millions of years of evolution. As a consequence of the tremendous amount of existing organisms, combined with the very specific needs of each of them, many different optimization strategies can be found in nature. These approaches vary from the adaptation of structural features (hierarchically ordered nanostructures<sup>1</sup>, self-assembled structures<sup>2</sup>, etc.) to the modification of compositional features. Among the modification of compositional features, there is a route which has specially attracted the attention of materials researchers, the creation of hybrid organic-inorganic materials.

A hybrid organic-inorganic material is defined as a material that includes an organic and an inorganic moiety blended on the molecular scale<sup>3</sup>. Commonly, a distinction of hybrid materials in *Class I* and *Class II* is made, based on the kind of interaction between the two moieties. *Class I* hybrid materials are those composed of components with rather weak interactions, including Van-der-Waals, hydrogen bonds or weak electrostatic interactions. In contrast, the components of *Class II* hybrid materials show strong chemical interactions, such as, covalent, coordination or ionic bonds.

Many natural materials are composed of a soft organic matrix (proteins, polysaccharides, etc.) and hard inorganic moieties (metals, minerals, etc.). Thanks to such combination, hybrid materials combine the elasticity and lightness of the organic matrix with the stability and toughness of the inorganic moieties. Bones are one of the most characteristic examples of hybrid natural materials. Composed by a

collagen matrix intermixed with hydroxyapatite nanocrystals, bones are tough, giving bodies a structure, but they are elastic enough to compensate the stress that acts on the body upon movements. The proportion of the components varies depending on the type of bone and so do the properties. As a further example, mollusc shells consist of a strong and resilient hybrid organic-inorganic material, nacre. In nacre, hexagonal inorganic  $\text{CaCO}_3$  platelets are glued together by a mixture of chitin and proteins. Its unique composition and architecture makes nacre as tough as an inorganic material, simultaneously exhibiting an extraordinarily high bending strength for sculpting and protecting the molluscs.

However, apart from the mentioned combination of properties, hybrid materials can also present some new or improved functionalities as a consequence of the physical or chemical interactions between the components. For example, Broomell *et al.* discovered that the toughness of the *Nereis* sea worm jaw arises from a metal-protein coordination in the hybrid material<sup>4,5</sup>. They observed that the toughest areas of the jaw were characterized by a high concentration of  $\text{Zn}^{2+}$  cations. These metal ions coordinate to the protein matrix, stiffening the tips of the jaw. Later on, similar metal-protein hybrid materials were observed in the toughest parts of some other insects, such as dry wood termites' mandibles<sup>6</sup> and spider fangs<sup>7</sup>. As a consequence of those investigated examples, it was initially assumed that the incorporation of inorganic moieties into organic matrices is a bioadaptation strategy exclusively for mechanically demanding environments. However, it was soon discovered that hybrid materials also play a key role in other critical properties of biomaterials, such as adhesion<sup>8,9</sup> or self-healing<sup>10</sup>.

In a conscious or non-conscious way, humans frequently mimic nature to fulfil their needs. Hybrid organic-inorganic materials are not an exception and the creation of synthetic hybrid materials goes even back to cave paintings. According to present knowledge, cavemen mixed some organic fluids, such as blood or grease, with inorganic pigments for drawing cave walls. However, other ancient paintings led to the discovery of which is considered the first synthetic hybrid material: Maya Blue. The Maya used to represent dairy or special events in bright colour paintings. For the surprise of the archaeologists, some Mayan paintings discovered in Yucatan maintained the bright and shining blue colour over centuries (Figure 1.1a). The

impressive temporal stability of the later called Maya Blue arises from its hybrid structure: organic indigo pigments intercalated into inorganic palygorskite clay channels<sup>11</sup>. Similarly, in the medieval age different metal salts were mixed with organic fatty acids to obtain fluid and stable bright colour paints. It has been later demonstrated that the creation of a hybrid material consisting of a metal coordinated network of diacids is responsible for the good preservation of the paints over centuries<sup>12,13</sup>. In all those early times examples, the fortuitous creation of a hybrid material led to improved properties. However, this natural adaptation strategy was not intentionally mimicked until the twentieth century. The first reported intentional synthesis of a hybrid organic-inorganic material dates from 1996, when Belfiore *et al.*<sup>14,15</sup> mixed two organic polymers (1,2-polybutadiene and 3,4-polyisoprene) with Pd salts in solution. The resulting polymer-Pd hybrid presented extremely different physicochemical properties compared to those of the pristine polymers. The Young's Modulus of the hybrid increased 50 times and the solubility was significantly altered. The strong interaction between the Pd and the polymer backbone was identified as responsible for the huge properties changes. Nowadays, metal-organic frameworks (MOFs) are among the most relevant synthetic hybrid materials (Figure 1.1b). These compounds are formed by metallic ions or clusters coordinated with organic ligands forming one, two or three-dimensional porous structures that can be used for hydrogen storage, catalysis, etc. These examples demonstrate that the hybridization can be artificially mimicked, resulting in new materials with outstanding properties.

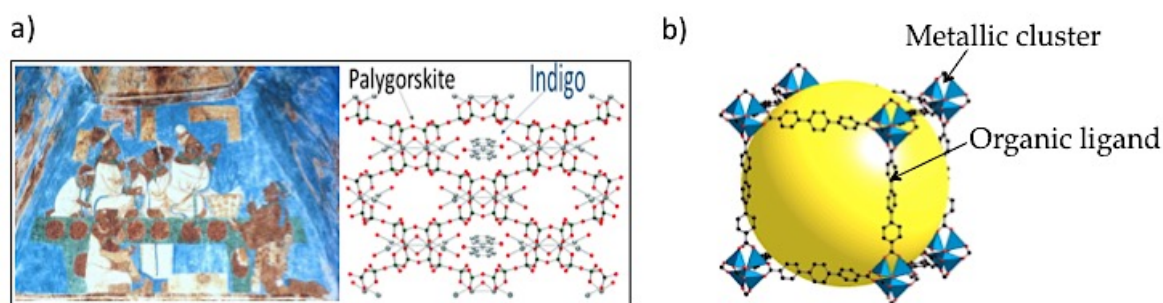


**Figure 1.1:** Examples of synthetic hybrid organic-inorganic materials a) Mayan wall painting maintaining the bright blue colour (left) and the structure of the hybrid material that generates the coloration (right)<sup>16</sup> b) Structure of a MOF<sup>17</sup>.

Since then, lots of efforts have been invested into synthesis and studies of new organic-inorganic hybrid materials. However, still nowadays, the most commonly used synthetic routes do not differ much from the initial attempt done in 1996. In general, two different approaches (Figure 1.2) are used to synthesize a hybrid material<sup>3</sup>:

- **Building block approach:** In this approach preformed and well defined building blocks are mixed and react with each other creating the hybrid material. Therefore, the building blocks maintain at least partially their molecular integrity and can be found as such in the final hybrid material.
- ***In situ* formation of the components:** Opposite to the previous approach, in this case one or both structural units are formed from precursors during the hybridization reaction. Thus, the precursors are transformed into a novel structure that will be part of the hybrid material.

Both strategies present advantages and disadvantages. For example, the performance of the final hybrid material is easier predicted and controlled by the building block approach. However, the resulting properties of the hybrid materials synthesized by this approach are not very well tuneable. The properties of the hybrid materials synthesized by the second approach, on the other hand, are extremely sensitive to the reaction conditions, making a prediction of the performance of the final hybrid material more difficult. Nevertheless, the properties can be easily tuned by controlling the reaction parameters.

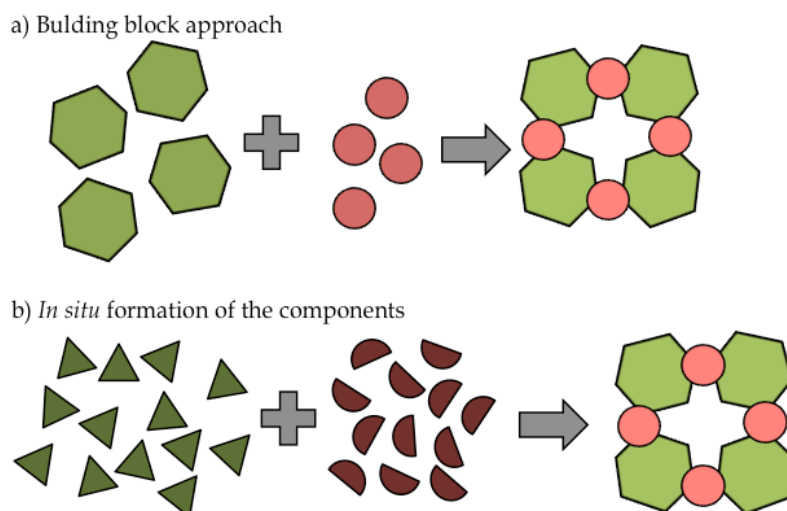


**Figure 1.2:** Approaches to synthesize hybrid organic-inorganic materials. a) In the building block approach the integrity of the precursors is maintained in the final material. b) In the *in-situ* formation the precursors are converted into a novel material.

The *in-situ* formation of one of the component is the most commonly used strategy to create hybrid materials. If the *in-situ* formed component is the organic fraction, polymerization in presence of inorganic clusters is carried out. In contrast, for an *in-situ* formation of the inorganic component, sol-gel strategies in presence of an organic polymer are used. However, such approaches have several drawbacks:

- Sol-gel processes are often used for the thermal limitations the presence of organic polymers pose. The inorganic solids synthesized following this process are often the kinetically, but not the thermodynamically most stable structures. Consequently, the obtained inorganic materials are usually amorphous or with nanoscale crystalline areas.
- The distribution of the inorganic agglomerates within those hybrid materials is often not homogeneous.
- The reaction is carried out in a solvent that plays a key role in the stability and properties of the final material. The solvent has to dissolve both components (and the respective precursors) and it has to be easily removable without compromising the stability and properties of the synthesized hybrid material, which may not be straightforward.

Such drawbacks make researchers keep on looking for different strategies to create high performance hybrid materials. In this pursuit, the work presented in 2009 by Lee *et al.* enabled many new processing possibilities<sup>18</sup>. As opposed to the previously studied strategies, in this work the synthesis of the hybrid material was not carried out in liquid phase but from the vapour phase. Using a modification of Atomic Layer Deposition (ALD), Lee *et al.* infiltrated spider silk with vapours of metal organic molecules. The creation of a hybrid metal-protein material in the subsurface area of the silk greatly enhanced the mechanical properties of the silk, proving the adequacy of the approach for the synthesis of hybrid organic-inorganic materials.

### **1.2.- Atomic Layer Deposition**

Even if already in the 1960s some initial experiments were done by Russian and Finish groups, the real development of Atomic Layer Deposition (ALD) occurred in the mid-1970s. The basis of the reactor and the process technology of ALD were developed driven by the need of producing high quality ZnS thin films for thin film electroluminescent (TFEL) flat panel displays. When T. Suntola and coworkers<sup>19</sup> first patented the technology in 1974 it was named Atomic Layer Epitaxy (ALE). However, scientist soon realized the films did not follow an epitaxial growth, but they were mostly amorphous or polycrystalline. Thus, the name was changed to Atomic Layer Deposition (ALD) that became generally accepted by the end of the twentieth century. However, the real breakthrough of ALD came at the beginning of the twenty first century. The continuous and exponential scaling of the microelectronic devices created a need for the mass production of rather thin conformal coatings in high aspect ratio structures. As a suitable technology to fulfil this need, ALD attracted the interest of the major semiconductor companies and academic groups who introduced more and more ALD reactors in their laboratories.

ALD is a cyclic and sequential vapour phase technique to create thin films and coatings. Similar to Chemical Vapour Deposition (CVD), the process is based in the chemical reaction of two or more gaseous precursors. In the most common ALD

processes, one of the precursors is an organometallic, metal organic or halide as metal source and the other one is a reactive counter precursor, such as water, ammonia or similar. In contrast to CVD, where the substrate is simultaneously exposed to all the precursors, in ALD the precursors are temporally separated. As a consequence, in ALD the chemical reaction does not occur in the space above the substrate, but at the solid-gas interface, where the precursors independently react with the surface of the substrate. Each precursor dosing is followed by a purging step to remove the excess of the precursor upon saturation and reaction by-products. This assures that a maximum of one monolayer of precursor is bound to the surface in each cycle. Figure 1.3 illustrates the steps in an ALD deposition of zinc oxide (ZnO) with diethylzinc (DEZ) and water as precursors. The process consists of 4 steps:

- 1.- Pulsing of DEZ vapours into the chamber. In this first step, DEZ is carried into the chamber by an inert gas (usually N<sub>2</sub>). This first precursor chemisorbs onto the substrate surface by reacting with the functional groups on the surface of the substrate (for example hydroxyl groups).

- 2.- Purging. The chamber is evacuated and purged by the carrier gas. The excess of DEZ and the reaction by-product ethane are removed in this step.

- 3.- Pulsing of water vapour into the chamber. The water molecules react with the chemisorbed DEZ hydrolysing the Zn-Ethyl bonds. More ethane is created as by-product and the first layer of ZnO is formed, exposing hydroxyl functionalities at the surface and thus restoring the chemical functionality of the surface for the next cycle.

- 4.- Purging. The second purging step finalizes the ALD cycle. In this last step, the excess water and the by-products are removed.

By repeating this cycle an additional layer of ZnO is grown on top of the substrate with the thickness of the film being a function of the number of applied cycles.

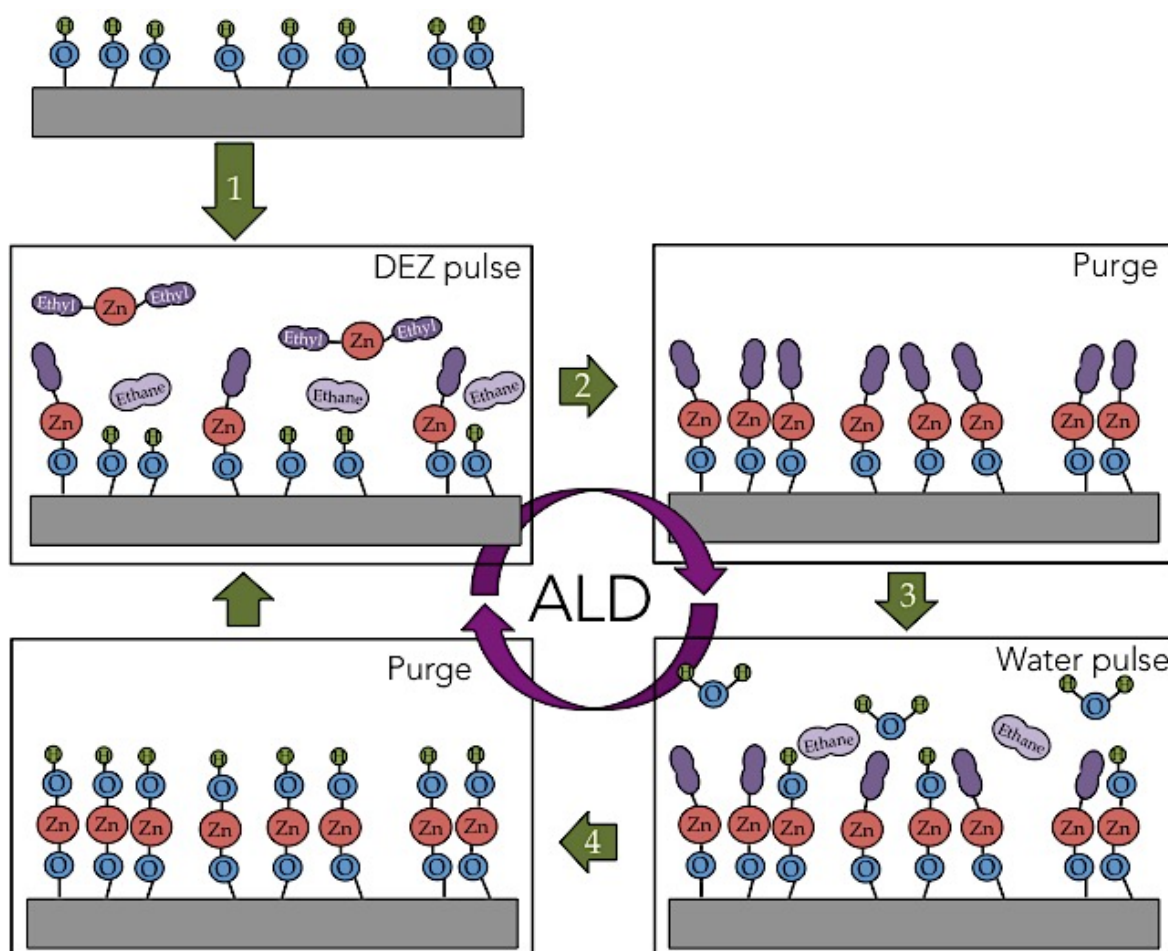


**Figure 1.3:** Schematic of the ALD deposition of ZnO using diethylzinc and water as precursors.

As a consequence of its special working mechanism, ALD has great advantages over other coating techniques. For example, the thin films obtained by ALD are characterized by their conformal, pinhole free and uniform nature. Besides, as already mentioned, the thickness of the film depends on the number of ALD cycles and Ångstrom-scale control is achieved. Finally, the gaseous precursors will diffuse and chemisorb to any available surface site, leading to coatings with very uniform thickness even in structures with extreme aspect ratios.

Since the beginning of use of ALD, much effort has been invested in the development of processes and precursors that will enable the deposition of a broad range of materials. Nowadays, a large variety of materials has been already deposited by ALD<sup>20-26</sup>: metal oxides, metal nitrides, metal sulfides, transition metals, perovskites or even noble metals. Also, organic molecules can be used as precursors,

resulting in a growth of polymer thin films. Such processes are named molecules layer deposition (MLD). Mixed processes of ALD and MLD have also been demonstrated, which result in the bottom-up growth of hybrid thin films<sup>27,28</sup>.

As a consequence of the high conformality and great control over the thickness of the deposited films, ALD became a method-of-choice for various applications<sup>29</sup>. In the past decade, microelectronic applications dominated the ALD process development. Initially, the use of ALD was limited to the fabrication of insulating metal oxide layers in microelectronic devices, such as dynamic random-access memory (DRAM) or metal-insulator-metal (MIM) capacitors. In the beginning of the 2000s, the production of high-*k* oxides, especially HfO<sub>2</sub>, dominated the R&D of ALD. More recently, ALD has found applications in further areas such as photovoltaics fabrication<sup>30</sup> or protective coatings<sup>31</sup>. Besides, with the boom of nanotechnology, ALD is no longer just a thin film deposition technique but it has also become a leading technique in the synthesis of nanomaterials: ALD has been used for the synthesis of various nanoscale structures from nanoparticles<sup>32,33</sup> or nanotubes<sup>34,35</sup> to complex nanostructured materials<sup>36</sup>.

The substrate in most of the examples mentioned so far is a dense solid, such as a Si wafer. However, when ALD is applied to a soft or porous material (organic polymers, membranes...) the gaseous precursors will not only react with the surface functional groups but also can diffuse into and infiltrate the substrate, often even reacting with the functional groups of the bulk polymer<sup>37</sup>. As a result, apart from the thin film creation on top of the substrate, a subsurface growth of the deposited material is observed. Thus, when an organic polymer is processed with a metal oxide by ALD, a hybrid organic-inorganic material is created in the subsurface area of the polymer. The presence of this intermixed area was considered a negative side effect at the beginning. However, it was soon discovered that this hybrid layer dramatically alters the properties of some polymers. Moreover, it is at the same time also a great novel approach for the synthesis of new hybrid materials. In order to more controllably promote the creation of this hybrid layer, the ALD process was modified resulting in a new technique: Vapour Phase Infiltration (VPI).

### 1.3.- Vapour Phase Infiltration (VPI)

Vapour Phase Infiltration (VPI) is an emerging vapour phase technique for the synthesis of organic-inorganic hybrid materials. Similar to ALD, in VPI the synthesis of the hybrid material is based on alternating dosing of two vapour phase precursors. However, in this case an additional exposure step is introduced between precursor dose and purge (Figure 1.4). In this exposure step, the substrate is exposed to the precursor for a variable time period (from 1 second to hours) to allow sufficient time for the precursors to diffuse into the substrate and in this way infiltrate it.

Contrary to ALD, the growth of the hybrid material inside the substrate is not self-limiting. However, the depth and density of the hybrid area can be controlled by some processing parameters, such as the temperature, exposure time, and number of cycles. Thus, by choosing the correct parameters even a complete conversion of the substrate into a hybrid material can be obtained. Being a vapour phase technique, the already mentioned problems associated with the use of solvents are eliminated. Besides, the VPI process can often be carried out at low temperatures and even at atmospheric pressures, making it compatible with a vast range of organic substrates.

As a consequence of the potential of VPI for the synthesis of hybrid materials, various research groups have simultaneously developed their own variations with slightly different process parameters and names; Multiple Pulse Infiltration (MPI), Sequential Infiltration Synthesis (SIS) and Sequential Vapour Infiltration (SVI). However, as the atomic-scale mechanisms are identical in all the variations, they can be grouped under the more general term VPI<sup>38</sup>.

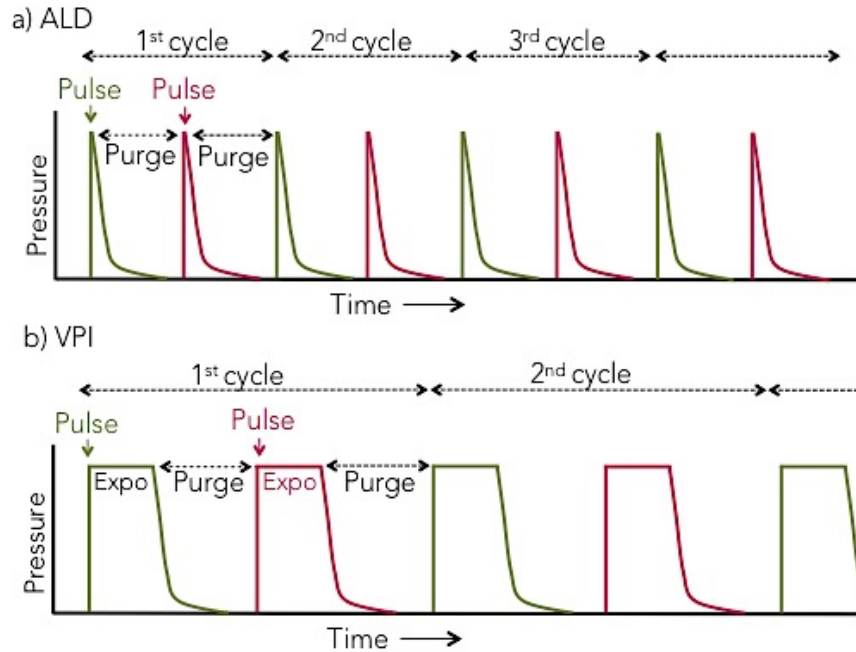


**Figure 1.4:** Schematic of the pressure profiles of a) an ALD process and b) a VPI process.

The role hybrid materials play in nature has been widely studied. Thus, it is not surprising that the first targets for studying the synthesis of hybrid materials through VPI were biomaterials. The study of the VPI of biopolymers has mainly focused on its impact on the mechanical properties. As already mentioned, Lee *et al.* were the first ones demonstrating that the mechanical properties of a material were greatly increased after a VPI treatment<sup>18</sup>. They observed that the infiltration of Zn, Ti or Al greatly increased the mechanical toughness of spider silk due to the incorporation of the metal ions into the protein matrix<sup>39</sup>. As observed in nature, the impressive change in silk's properties arose from the simultaneous cross-linking of the protein chains and reduction of the protein crystallite size caused by the infiltrated metal ions. Once the potential of the technique for the modification of biomaterials was demonstrated, the modification of many other biomaterials through VPI was studied: collagen membranes<sup>40</sup>, cellulose fibres<sup>41</sup>, porphyrin structures<sup>42</sup>, etc.

Observing the impact of VPI in the properties of different biomaterials, some research groups started to apply the same process to synthetic polymers. Similar to biopolymers, the first studies focused on the impact of VPI on the mechanical

properties of the technical polymers. However, in later works the effect of VPI on both the chemical and physical properties of the polymers was studied. Thus, apart from the enhancement of the mechanical properties<sup>43-45</sup>, the modification of technical polymers by VPI has led to a wide range of potential applications.

For example, by introducing area-selectivity in the VPI process, patterned materials can be synthesized. Three main strategies are followed for this purpose: using a nanomaterial as a sacrificial template, using block copolymers with different reactivity towards the precursors, and lithography. The use of a sacrificial template is an efficient and easy way to create patterned nanomaterials through VPI. Even if different types of templates and processes have been described<sup>46-49</sup>, the procedure is common for all of them. A polymer is infiltrated with an inorganic material by VPI. During the VPI process the organic template will be converted into a hybrid organic-inorganic material that maintains the morphology of the template. Finally, the hybrid material is calcinated and an inorganic replica of the template is obtained. Similarly, the use of phase-segregating block copolymers for the synthesis of patterned materials is based on the hybridization of a polymer through VPI followed by its calcination. However, in this case the most reactive constituent of the block copolymer is selectively hybridized thus, after removing the template, the nanoscopic domains of this constituent are reproduced. The morphology and size of the nanoscopic domains can be tuned by adequately choosing the constituents, which allows the creation of a huge variety of patterned materials by VPI<sup>50-57</sup>. Finally, the VPI treatment of photoresist polymers used in lithography significantly changes their resistance to etching. Thus, VPI can be combined with lithography to eliminate the need of intermediate hard masks and reduce the cost and pattern fidelity losses of the lithographic process<sup>58-60</sup>.

A further application field that was approached with the VPI-fabricated hybrid materials is optics<sup>61-66</sup>. The chemical stability and good control over the morphology of the hybrid materials synthesized by VPI has also attracted the attention of several groups investigating photovoltaic devices<sup>67,68</sup>.

However, one of the most promising application fields of VPI is electronics. Most of the organic polymers treated by VPI in the last years were electronic insulators, so little attention was paid to the impact of VPI processes on their

electrical properties. However, very recent publications exploring this potential clearly demonstrate that VPI is a powerful technique for tuning polymer-based electronics. As an example, Yu *et al.* improved the performance of a triboelectric nanogenerator by VPI of  $\text{Al}_2\text{O}_3$  into the three different polymers polydimethyl siloxane (PDMS), Kapton and PMMA<sup>69</sup>. The metalation of the polymers resulted in an internal  $\text{AlO}_x$  doping. The  $\text{AlO}_x$  clusters repelled the electrons reducing the ability of the doped polymer to retain them, thus increasing the output power of the generator.

A more direct way to alter the electronic properties of polymers by VPI is possible as well. Among the different approaches to dope organic semiconductor polymers, oxidative treatment with strong acids and the application of transition metal oxides or Lewis acids as dopants is common. In this way charge carriers are created, which can delocalize along the polymer chain. However, all these processes are carried out in a liquid state, which may involve the already described drawbacks in processing or post-processing. Thanks to a new doping strategy based on VPI processing of polymers developed by Wang *et al.*, doping of organic semiconductors without the use of solvents became possible for the first time. In their works they increased the conductivity of poly(3-hexylthiophene) (P3HT) films by 5 orders of magnitude after infiltrating  $\text{MoCl}_5$  into the polymer<sup>70</sup> and outperformed the conductivity values of polyaniline (PANI) doped in the traditional wet-chemical way with HCl using  $\text{MoCl}_5$  or  $\text{SnCl}_4$  as VPI dopant<sup>71</sup>. Moreover, the process allowed for tuning the conductivity by simply controlling the number of infiltration cycles.

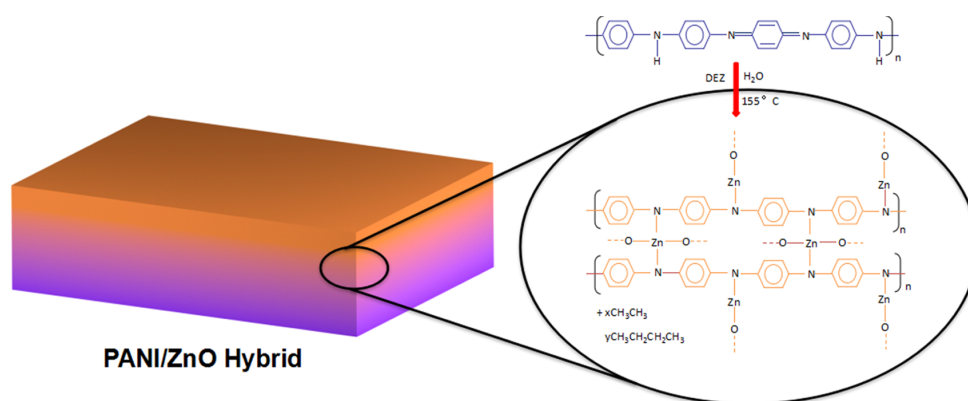


**Figure 1.5:** Schematic of a PANI substrate after doping with ZnO by VPI. The ZnO cross-links the polymer chains oxidizing the polymer backbone and at the same time becomes doped through the N from PANI. In this way, both components, the PANI and ZnO synergistically contribute to the conductivity of the hybrid. Reprinted with permission from <sup>72</sup>. Copyright 2017 American Chemical Society.

In both the described processes only the metal-containing precursor was supplied and allowed to diffuse and react with the polymer. The same group applied a traditional two-precursor VPI process for the infiltration of PANI with ZnO with really surprising results<sup>72</sup>. After the infiltration, the resulting PANI-ZnO hybrid material consisted of PANI chains that were cross-linked by Zn-N and Zn-O bonds (Figure 1.5). Simultaneously, and in consequence, quinoid groups within the polymeric chain were turned benzenoid groups, which clearly showed that the Lewis acid was able to dope PANI. However, the unexpected high values of the conductivity (18,42 S/cm) pointed towards a synergy through mutual doping of both constituents, the polymer and the embedded ZnO. Namely, the infiltrated ZnO acts as dopant for the PANI, while at the same time, through binding of Zn to the nitrogen in PANI, the infiltrated ZnO becomes nitrogen-doped. This work is a breakthrough in the electronic modification of polymers and opens up new possibilities, for example the electronic conversion of insulating high performance technical polymers, such as Kevlar<sup>®</sup>.

#### 1.4.- Kevlar®

Commonly known as Kevlar, poly (p-phenylene terephthalamide) (PPTA) is a high-strength, high modulus and thermally stable synthetic polymer. Kevlar's outstanding properties arise from its unique chemical structure discovered by Stephanie Kwolek in 1965 at Du Pont laboratories.

The invention of Nylon and polyesters in the 1960s opened the market for synthetic polymeric fibres. The use of these man-made polymers rapidly spread over different application fields, from industrial to daily life applications. However, the strength and toughness of these polymers were not particularly high. In order to obtain the maximum breaking strength and toughness modulus, the polymer chains had to be in extended-chain configuration and almost perfectly crystalline packed. In the case of Nylon and polyesters, post spinning mechanical treatment was required for the detangling and orientation of their flexible chains. However, the mechanical properties obtained after this treatment were far from the theoretically predicted values. This pushed the researchers towards the synthesis of extended rigid chain polymers and Kevlar was created.

Chemically, Kevlar is composed of *para*-di-substituted benzene rings, interconnected with amide groups (Figure 1.6). Due to the rigidity of the polymer backbone, Kevlar is present in an almost perfect extended chain configuration. The repetitiveness of the molecular backbone and the *para* position of the amide groups enable the creation of intermolecular hydrogen bonds and arrangement of the polymeric chains in ordered domains, known as lamellae. The lamellae are around 600 nm wide and have an average length of 35 nm<sup>73</sup>. These ordered domains are stacked along the fibre axis, separated by defect zones, forming fibrils. Finally, the fibrils are joined together by tie points creating plated sheets, radially stacked to form the Kevlar fibre<sup>74-76</sup>.

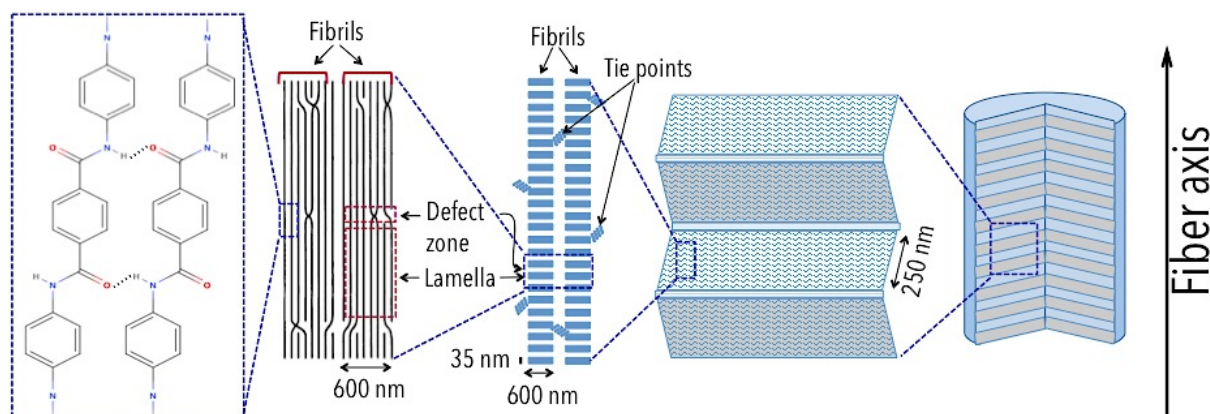


**Figure 1.6:** Chemical structure and morphology of Kevlar fibres.

Due to its highly ordered morphology, Kevlar acts as a lyotropic liquid crystalline polymer. The crystalline structure of Kevlar is described as monoclinic (pseudo-orthorhombic) with the unit cell parameters being  $a=7,87 \text{ \AA}$ ,  $b=5,18 \text{ \AA}$  and  $c$  (fibre axis) $=12,9 \text{ \AA}$ <sup>77</sup>. This unique structure is responsible for the outstanding physicochemical properties of the polymer.

As the alignment of the polymeric chains is promoted during the spinning process, Kevlar is almost exclusively produced in form of fibres or woven fabrics. However, the crystallinity can be controlled by tuning the polymer chain length and the processing parameters. Thus, various types of Kevlar with very different properties are available on the market. Kevlar 29 is the most widely used variation of Kevlar and is used for ballistic applications, ropes and cables, cut-resistant gloves, helmets, tire reinforcement, etc. Another commonly used variation is Kevlar 49 or high-modulus Kevlar. This type of Kevlar is used in more specific applications, including fibre optic cable or composites for marine sporting goods or aerospace applications. A comparison of the most characteristic mechanical properties of Kevlar 29 and Kevlar 49 is shown in Table 1.1.

**Table 1.1:** Comparison of the characteristic mechanical properties of Kevlar 29 and Kevlar 49<sup>78</sup>.

Property	Kevlar 29	Kevlar 49
Breaking strength (N)	338	264
Tensile Modulus (MPa)	70.500	112.400
Elongation at break (%)	3,6	2,4

Apart from the great mechanical properties, Kevlar also possesses a really high chemical stability. As a consequence of the large amount of intermolecular interactions and the tight crystalline packaging, hot and concentrated sulphuric acid is needed to dissolve Kevlar. Besides, extended exposure (up to 100 hours) to strong acids or bases, such as sodium hypochlorite or hydrochloric acid, are needed for appreciable degradation of the mechanical properties of the fibres<sup>78</sup>. Similarly, the resistance of Kevlar to hydrolysis is notable as only 10% of the strength is lost after 70 hours of exposure to saturated steam. Regarding the thermal stability, Kevlar does not melt but it decomposes at high temperatures (around 540°C in nitrogen atmosphere and 430°C in air). Finally, Kevlar is a good thermal insulator and inherently flame resistant.

However, as Kevlar's properties arise from its highly ordered structure, any external factor altering this order will have an impact on the mechanical properties. Among these external factors temperature and UV radiation have the strongest impact. In the case of temperature, exposure of Kevlar fibres to 250°C during 60 or more hours causes a reduction of its tensile strength by 70%. The reason of this enormous impact on the mechanical properties is the change in the crystal dimensions. As already mentioned, Kevlar resembles a liquid crystal and its ordered structure is obtained from the liquid crystalline state. However, as the intramolecular interactions overcome the intermolecular forces (hydrogen bonding and Van-der-Waals forces), a Kevlar crystal is merely packing of frozen chains and not in an equilibrium state. Thus, when the fibres are exposed to high temperatures water molecules trapped within the polymer are released and in addition the polymeric chains gain mobility with introduction of thermal energy. As a consequence, more hydrogen bonds are formed and the b lattice parameter is

shortened, decreasing the crystallite size<sup>75,79</sup>. Regarding UV radiation, Kevlar shows a strong absorption peak in the 300-400 nm range. The light of this wavelength range has sufficient energy to break chemical bonds within the polymer chain. Thus, exposure of Kevlar to UV light causes chain-scission and end group oxidation reactions, which degrades the fibres<sup>80</sup>. As a consequence of its thermal and UV sensitivity, Kevlar fibres and fabrics have to be protected from sunlight, limiting the practicability of Kevlar for some applications.

Being a polymer created out of the need of high modulus fibres, it is not surprising that the use of Kevlar has mainly being limited to mechanically demanding applications. As a consequence, the vast majority of the studied modifications of Kevlar target a better mechanical performance. The modifications of Kevlar studied so far can be divided into modifications of the chemical structure on the one hand and the post-synthetic modifications on the other hand. Since an extended chain configuration is key for the mechanical properties, new liquid crystal-like polymers aiming to outperform Kevlar's properties (Nomex®, Vectran®...) have been developed by modifying the functional groups of Kevlar while maintaining a rigid aromatic backbone. Regarding post-synthetic modifications, the formation of a composite material, that is, Kevlar fibres embedded in a matrix, is still the most common approach. Besides, the functionalization of Kevlar by treatment of its surface or coating of the fibres is also performed. The surface of Kevlar fibres is usually treated for a better adhesion of the fibres to the matrix in a composite material<sup>81,82</sup>. Coating the fibres with a resin or a metal oxide protects the fibres from UV radiation, thus preventing the degradation of the mechanical properties<sup>83-86</sup>. However, little to none research has been done in the modification of further properties of Kevlar, such as thermal or electrical properties.

Lately, since flexible and wearable electronics are gaining importance, functionalization of polymeric fibres for the integration of electronic devices into textile or other applications is attracting great interest<sup>87-91</sup>. As electrical conductivity is needed, conducting organic polymers such as PANI or PEDOT:PSS are most used as polymeric substrates. Nevertheless, some works have been already published, showing Kevlar can be successfully used as the base materials for e-textile devices<sup>92-</sup>

<sup>95</sup>. In all those cases, Kevlar is selected because of its great mechanical properties and it is coated with a conducting material for introducing conductivity.

## **1.5.- Objective and structure of the thesis**

This thesis aims to explore the potential of VPI for the synthesis of multifunctional hybrid organic-inorganic materials. Using Kevlar as a case study, the synthesis of hybrid materials through ALD and VPI of metal oxides and technical polymers as substrates is studied. The thesis aims to demonstrate that not only mechanical properties of technical polymers can be improved by VPI, but also new functionalities, such as electrical conductivity, can be introduced. The effect of the hybridization of polymer with inorganics on different properties is explained thanks to the elucidation and understanding of the structure and interactions of the synthesized hybrid materials.

Chapter 2 overviews the experimental techniques and methods used in this thesis for the chemical and physical characterization of the samples.

Chapter 3 describes the improvement of the stability of Kevlar against exposure to elevated temperature and UV light thanks to the VPI of ZnO. The structure of the synthesized Kevlar-ZnO hybrid material is theoretically predicted and experimentally proven.

Chapter 4 presents a novel combination of ALD and VPI for the synthesis of multiscale hybrid materials. The improvement of the toughness of Kevlar fibres resulting from the application of this combined ALD/VPI process is analysed.

Chapter 5 focuses on the synthesis and characterization of a conductive and photoactive Kevlar. The electrical conductivity of the hybrid Kevlar after various infiltration cycles is characterized. The photocatalytic activity of the samples under visible light is studied analysing the degradation of Rhodamine B in contact with the modified Kevlar and under exposure to visible light.

Finally, the main conclusions and the future perspective are presented in Chapter 6.



## Chapter 2

### Experimental techniques and methods

#### 2.1.- Fourier Transform Infrared Spectroscopy (FTIR)

Infrared spectroscopy (IR) is a non-destructive technique for the qualitative analysis of gaseous, liquid or solid samples. This technique provides information about the chemical functional groups present in the analysed sample. The sample is irradiated with an infrared (IR) light beam, with wavelengths between 1000 and 50000 nm, even if usually a smaller region between 2500 and 25000 nm is used. When exposed to the infrared light beam, an excitation of molecular bonds to a higher vibrational energy state occurs by absorption of photons with a specific energy that varies depending on the chemical groups. The wavelengths that are absorbed by the sample are characteristic of its molecular structure. As a result of the analysis, a plot of the absorbance or transmittance versus wavenumber is obtained, where the absorptions appear as bands characteristic for various types of molecular bonds.

In the case of Fourier Transform Infrared spectroscopy (FTIR), the absorption is simultaneously measured at all the infrared frequencies. For that, a Michelson interferometer is used that splits the IR light beam into two beams. One of the beams is directed to a fixed mirror while the other is directed to a movable mirror. Finally, the two beams are recombined and, as they have followed different paths, their interference is measured. As a result, an interferogram is obtained which depends on the time or the moving mirror position. In order to obtain a frequency spectrum, where the absorption is shown as a function of frequency, a mathematical technique called Fourier transformation is applied.

##### 2.1.1.- Attenuated total reflectance FTIR (ATR-FTIR)

The attenuated total reflectance (ATR) accessory is frequently used for FTIR measurements. By means of this accessory the near surface region of the sample is

analysed rather than the bulk. In ATR, the IR beam is coupled into a crystal with a high refractive index by directing the IR beam to the crystal in a specific angle. Once coupled in, as a consequence of the high refractive index of the crystal, multiple total internal reflection of the beam occurs before it can be coupled out again. Resulting from the total internal reflection of the beam an evanescent wave is created that extends around 0,5-3  $\mu\text{m}$  beyond the crystal surface and into the sample, when a sample is in direct contact with the crystal (Figure 2.1a). The evanescent wave will be attenuated or altered in the regions of the IR where the sample absorbs energy. The attenuated IR beam exits the opposite end of the crystal towards the detector, containing information of the functional groups present in the region of the sample closest to the crystal.

For all ATR-FTIR experiments performed in this thesis a Perkin Elmer Frontier FT-IT spectrometer was used. The analysed samples were woven fabric pieces.

### 2.1.2.- Fourier transform infrared nanospectroscopy (nano-FTIR)

The resolution of any spectroscopic method is limited by the diffraction limit of the used light. An ideal optical system would image an object point perfectly as a spot. However, due to the wave nature of light, diffraction occurs, and the image of a point is a blurred spot, regardless of how well the system is focused. As Ernest Abbe discovered in 1873, light with wavelength  $\lambda$  travelling through a material with a refractive index  $n$  makes a spot with a diameter  $d = \lambda/2NA$ , NA being the numerical aperture ( $NA = n \sin\theta$ , where  $n$  is the refractive index and  $\theta$  is the maximal half-angle of the cone of light that can enter or exit the lens). Considering an average numerical aperture ( $NA=1$ ), the smallest distance between two points that can be image would be  $\lambda/2$ . Thus, the diffraction limit in FTIR spectroscopy is around 400 nm, which is too large to analyse nanometre scale structures.

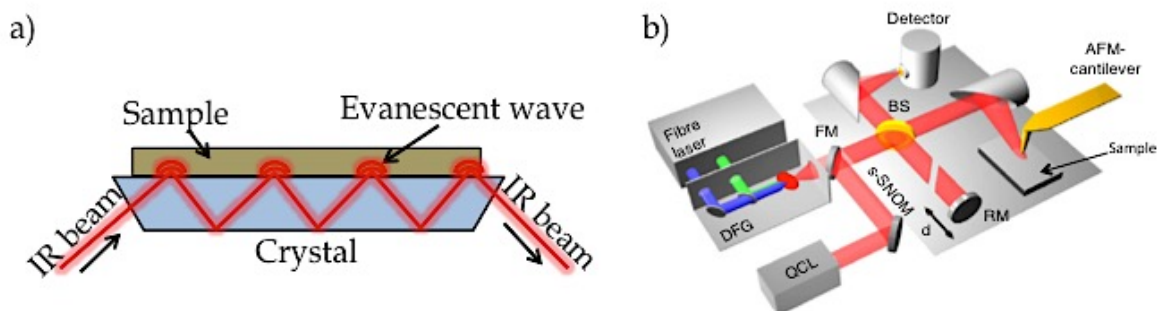


**Figure 2.1:** Schematic diagrams of a) the attenuated total reflectance (ATR) FTIR principle b) s-SNOM and nano-FTIR set-up<sup>96</sup>. The light source for tip illumination can be chosen with a flip mirror (FM) between a tuneable single line laser (quantum cascade laser, QCL) for s-SNOM and a mid-infrared continuum source (fibre laser plus difference frequency generator, DFG) for nano-FTIR. The beam splitter (BS, uncoated ZnSe), the reference mirror (RM) and the detector form a Michelson interferometer that analyses the light backscattered from the tip. The interferometer operates either in pseudoheterodyne mode (for s-SNOM imaging) or as a Fourier transform spectrometer (for nano-FTIR spectroscopy). Adapted with the permission from Springer Nature <sup>96</sup>. Copyright 2013

However, the diffraction limit can be bypassed using near-field techniques that operate less than 1 wavelength away from the image plane. Fourier transform infrared nanospectroscopy (nano-FTIR) is among these near-field techniques<sup>96</sup>. Nano-FTIR is based on another near-field imaging technique, the scattering-type scanning near-field optical microscopy (s-SNOM) (Figure 2.1b). In s-SNOM infrared images with nanoscale spatial resolution are obtained by recording the infrared light scattered at a metallized atomic force microscopy (AFM) tip. The tip acts as an antenna, concentrating the incident field at the apex, for local probing of molecular vibrations. In nano-FTIR, the AFM tip is illuminated by broadband infrared radiation and FTIR spectroscopy of the scattered light is done yielding infrared spectra with spatial resolution down to 20 nm.

## 2.2.- Electron microscopy

As already explained, the resolution of spectroscopic analyses and optical imaging techniques is diffraction limited. Besides the near-field techniques, changing the illumination source to smaller wavelengths is another common strategy to overcome this limitation. In electron microscopy techniques a beam of accelerated electrons is used as an illumination source. In this case, the wavelength of the electron beam depends on its acceleration, namely the higher the acceleration, the shorter the wavelength and the higher the resolution. The resolution of modern electron microscopes is nowadays limited to around 0,1 nm due to the objective lens system. Therefore, electron microscopy is one of the most important techniques for imaging nanomaterials.

When the sample is exposed to an accelerated electron beam, various kinds of interactions occur between the electrons and the sample. These interactions produce a loss of energy that is converted into heat, emission of low energy secondary electrons, high energy backscattered electrons, X-ray emission, etc., all of which can be used to characterize a sample microscopically or spectroscopically. The most common setups for this purpose include scanning electron microscopy (SEM) and transmission electron microscopy (TEM).

### 2.2.1.- Scanning electron microscopy (SEM)

In scanning electron microscopy (SEM) an electron beam scans across the sample surface and interacts with the sample. Typically, secondary electrons that emit from the sample surface upon excitation or elastically backscattered electrons, are detected. The amount of emitted secondary electrons depends on the topography of the surface of the sample, while the intensity of the backscattered electrons depends on the atomic number  $Z$ . Thus, the detection of these electrons enables the topological or compositional imaging of the sample surface. Further modes in SEM imaging involve detection of characteristic X-rays, cathodoluminescence, transmitted electrons or charge of the sample.

For the SEM experiments performed in this thesis, a Quanta TM 250 FEG (FEI) SEM was used. The imaging of the samples was carried out using a large field detector (LFD), at 70 Pa and with 10 kV as accelerating voltage.

### 2.2.2.- Transmission electron microscopy (TEM)

In the case of transmission electron microscopy (TEM) the transmitted electrons are detected to generate an image of the sample. As the electrons have to pass across the sample, only thin samples can be analysed. The transmission of the electron beam depends on the interaction of the beam with the sample and thus on the atomic number  $Z$ . The resolution obtained in TEM is typically higher than in SEM and with a well-adjusted TEM, even crystalline lattices of materials or single atoms can be observed.

### 2.2.3.- Energy-dispersive X-ray spectroscopy (EDS)

This analytical technique is used for the elemental analysis of a sample. In this case, the accelerated electron beam excites an electron from an inner electron shell of the atoms in a sample, that it is ejected leaving a hole behind. This hole is filled with an electron from an outer shell, releasing the energy difference in form of X-ray radiation. The energy of the emitted X-rays is characteristic and thus specific of an emitting atom. Therefore, EDS allows precise determination of the elemental composition of the sample. Generally, EDS is carried out together with TEM or SEM imaging so the elemental composition can be correlated with the topographical information.

In all the TEM-EDS experiments performed in this thesis, a FEI Titan microscope operating at 300 kV in scanning transmission electron microscopy (STEM) mode, equipped with an EDAX SDD detector, was used. The analysed lamellae were prepared by cutting cross sections of the fibres by a Focus ion beam (FIB) and thinned to transparency using a 5 kV gallium ion beam.

## 2.3.- X-ray diffractometry (XRD)

X-ray diffractometry (XRD) is a technique to analyse the crystallinity of a sample. In addition, XRD can be used for the identification of a crystalline material, determination of different phases in a polymorphic material, quantification of the crystalline phase, etc. This technique is based on the analysis of constructive interferences of monochromatic X-rays interacting with a crystalline sample. A monochromatic X-ray beam irradiates the sample at a grazing incident angle  $\theta$  and

the detector collects the reflected beam at an angle  $2\theta$  with respect to the incident beam, as indicated in Figure 2.2. The interaction of the incident X-ray with the sample will produce constructive interferences. When the conditions satisfy Bragg's law ( $2d \sin\theta = n\lambda$ ,  $d$  being the spacing between the diffracting planes,  $\theta$  the incident angle of the beam and  $\lambda$  the wavelength of the beam) a peak will occur in the reflected beam. From the analysis of these reflected peaks information about the different crystalline planes present in the sample is obtained.

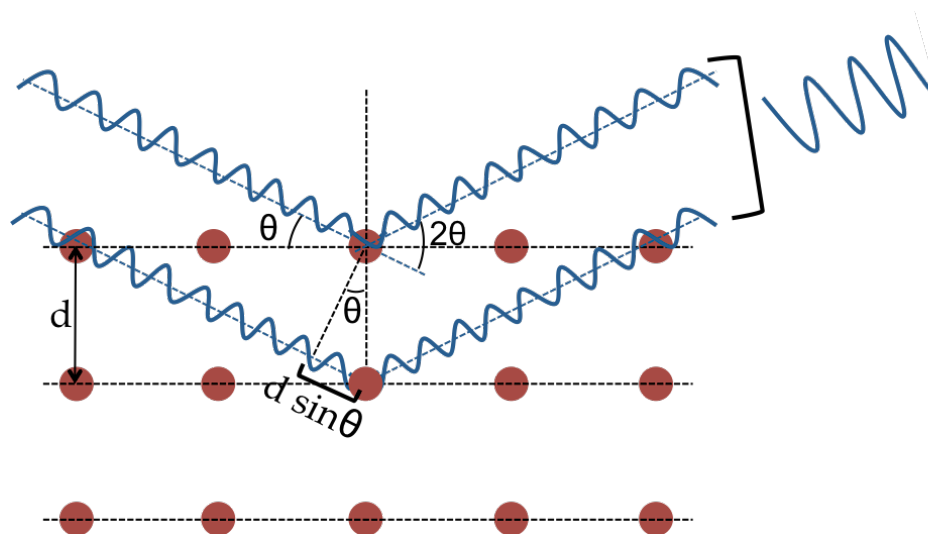


Figure 2.2: Schematic of the principle of XRD, showing the interaction of an X-ray beam with a crystal. When the Bragg's condition is fulfilled, constructive interferences create a reflected peak characteristic of the crystalline material.

The XRD measurements carried out in this thesis were done in an X'Pert PANalytical diffractometer, with a Cu Ka ( $\lambda=0,154$  nm) radiation source. During the measurements, the working voltage and current were 45 kV and 40 mA, respectively. The analysed samples were in form of woven fabric.

#### 2.4.- Uniaxial tensile tests

The study of the mechanical properties of a material supplies information about the behaviour of the material when subjected to forces. Knowing the mechanical properties of materials before implementation into an application is of great importance to ensure a reliable performance. Depending on the final

application of the material, different mechanical tests can be performed and parameters studied.

Uniaxial tensile tests are the most common mechanical tests and involve application of a stretching force to a sample until its rupture. To carry out a tensile test, one of the ends of the sample is clamped in a loading frame while the other end is clamped to a sliding frame. The sliding frame displaces in a constant velocity parallel to the sample axis, while the displacement and the applied force are measured simultaneously. The result of a tensile test is a stress-strain curve, as schematically shown in Figure 2.3a, where the elongation of the sample is represented as a function of the applied load. The strain ( $\epsilon$ ) is defined as the relative elongation of the sample in the direction of the applied force. The engineering stress ( $\sigma$ ) is calculated by dividing the applied load by the cross sectional area of the sample ( $A$ ). A common strain-stress curve can be divided into two sections; elastic area and plastic area. In the initial stage or elastic area, the curve shows a linear relationship between strain and stress, the slope of which is known as Young's modulus ( $E$ ). Within this elastic part of the curve, upon unloading no permanent deformation of the material is observed. At the yield point, the curve reaches the area of plastic deformation of the material, which is permanent even after unloading. The maximum stress that a material can withstand is known as ultimate tensile strength (UTS). Continued stress beyond this point results in fracture of the material. The area under the strain stress curve is defined as the Modulus of Toughness ( $U_t$ ) and corresponds to the energy the material can absorb before rupture.

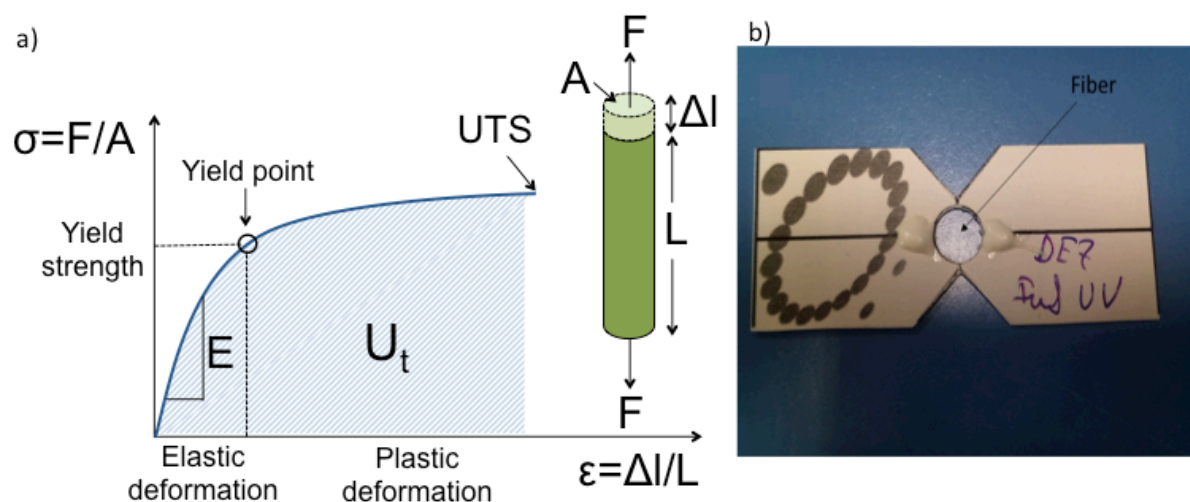


Figure 2.3: a) Illustration of a strain-stress curve b) Tensile test sample holder.

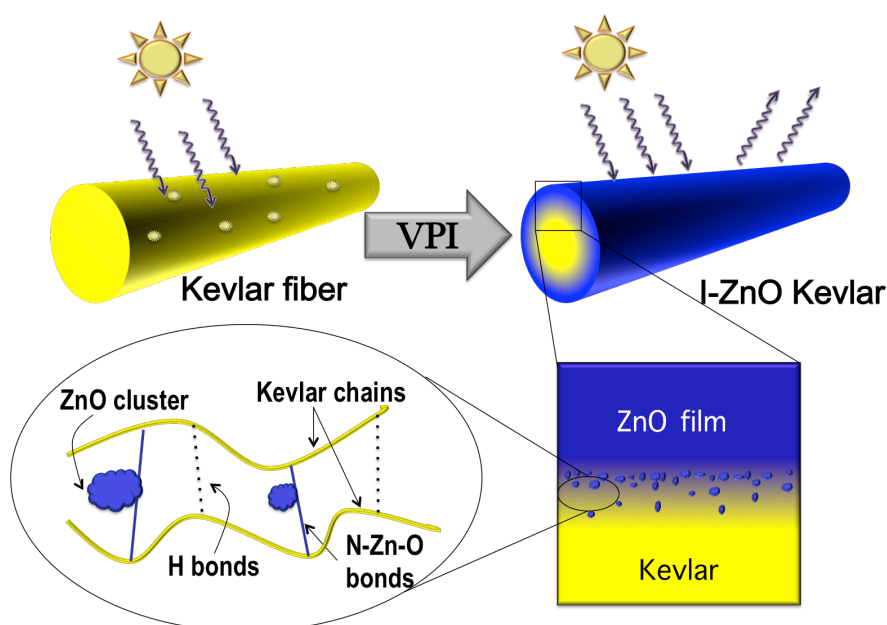
The measurements in this thesis were done in a BRUKER Universal Mechanical Tester with a resolution of 50  $\mu\text{N}$  and in accordance to the ASTM standard C1557-03 (2008). The fibres were fixed in a cardboard sample holder (Figure 2.3b), which has a punched hole of 6 mm diameter in the centre. After vertical alignment of the fibre across the hole, the sample holder is positioned in the mechanical tester with the fibre being un-strained. Finally, the sample holder is cut along the central guides and tensile force is applied while the strain is measured.

Further specific used methods are explained in the individual chapters.

## Chapter 3

### Improving Kevlar's stability through vapour phase infiltration of ZnO

In this chapter, the improvement of the thermal and UV stability of Kevlar through the infiltration and hybridization with ZnO is described. The vapour phase infiltration of ZnO into Kevlar fibres leads to the creation of a ZnO-Kevlar hybrid material in the subsurface area of the fibres. The structure of the hybrid, which is theoretically modelled and experimentally proven, consists of ZnO clusters grown among covalently cross-linked Kevlar chains. The infiltrated ZnO reacts with the polymeric chains, cross-linking them through N-Zn-O bonds and substituting the original hydrogen bonds. With this innovative route, Kevlar fibres are protected from thermal and UV-induced degradation without compromising their lightness and flexibility.



The work described in the present chapter is published in the journal *Chemistry of Materials* from the American Chemical Society (ACS). Graphs, figures and parts of the text of the publication are reused in this thesis with permission of the publisher.<sup>97</sup>

**Article:**

*Suppressing the thermal and ultraviolet sensitivity of Kevlar by infiltration and hybridization with ZnO. I. Azpitarte, A. Zuzuarregui, H. Ablat, L. Ruiz-Rubio, A. López-Ortega, S. D. Elliott and M. Knez. Chemistry of Materials, 2017, 29, 10068-10074*

### 3.1.- Introduction

Among the most important functionalities of natural materials are the mechanical properties, which in the course of billions of years of evolution have been optimized in various ways in order to fulfil the needs of a species in a specific environment. The optimization may involve structural features, such as the honeycomb structures<sup>98,99</sup>, structural and compositional features, such as bones or shells<sup>100,101</sup>, or dominantly compositional features. The last of these usually involves the incorporation of metals, such as Zn, Cu and Mn, into protein matrices, which result in exceptional improvement of the strength or hardness of the protein<sup>4-6</sup>. It is reasonable to assume that intentional incorporation of metals into artificial soft matter may also have positive effects on its mechanical properties. Especially vapour phase processing has been shown to greatly improve the toughness of some biopolymers (such as spider silk<sup>18</sup>, collagen<sup>40</sup>, cellulose<sup>41</sup>) through inclusion of very simple metal organic molecules into proteins or polysaccharides. However, the impact of this strategy on high-strength synthetic polymers of technological importance has never been reported.

Polymeric fibres with high strength are often called upon whenever a material with extraordinary mechanical performance is needed. Among such polymers, Kevlar is most prominent for its great mechanical toughness without the need of complex processing. Kevlar shows liquid crystal-like behaviour, such as great tensile strength, strong energy absorption and thermal insulation. Such outstanding properties in a material with great flexibility and low weight have made Kevlar the material-of-choice in many application fields including personal protection, sports equipment and aerospace.

In many of these applications Kevlar is exposed to harsh environmental conditions, including high temperature, UV radiation, and/or moisture which often degrade its mechanical properties<sup>79,80,102-104</sup>. In order to prevent the loss of mechanical properties, various approaches have been evaluated, most of them based on coating Kevlar fibres with a resin or a metal oxide<sup>93,95,105-107</sup>. The drawback of such coatings is on the one hand the extra weight of the resin and on the other hand the reduced flexibility upon coatings with brittle metal oxides. Therefore,

development of new routes for protection of Kevlar from thermal and UV-induced degradation along with preservation of its weight and flexibility, are in high demand.

In this chapter, we present a new approach for the stabilization of the mechanical properties of Kevlar fibres based on vapour phase infiltration of the fibre with ZnO. We use vapour phase infiltration (VPI)<sup>18,108</sup> to infiltrate zinc oxide into Kevlar in analogy to many naturally occurring hybrid biomaterials. We compare the properties of ZnO-infiltrated fibres with those of ZnO-coated fibres to demonstrate the advantages of this new approach.

## 3.2.- Experimental

### 3.2.1.- Sample preparation

The examined Kevlar fibres were obtained from the woven commercially used in bulletproof vests (Kevlar 29). The fibres had diameters of 10  $\mu\text{m}$  and were cut to lengths of 3 cm for the experiments.

The modification of the samples was performed in a commercial ALD reactor (Savannah S100, Cambridge NanoTech Inc). Both infiltration and coating of the fibres were carried out at 150°C under a constant nitrogen gas flow of 20 standard cubic centimetres per minute (sccm). Diethyl zinc (DEZ,  $\text{Zn}(\text{Et})_2$ , Strem Chemicals) was used as the zinc source and demineralized water as the oxygen source. The coated fibres (C-ZnO) were prepared following a typical ALD process with a cycle consisting of Pulse(DEZ, 0.08s)/Purge( $\text{N}_2$ , 30s)/Pulse( $\text{H}_2\text{O}$ , 0.08s)/Purge( $\text{N}_2$ , 30s). In contrast, the infiltrated fibres (I-ZnO) were prepared by VPI. A VPI cycle consisted of Pulse(DEZ, 0.08s)/Exposure(30s)/Purge( $\text{N}_2$ , 30s)/Pulse( $\text{H}_2\text{O}$ , 0.08s)/Exposure(30s)/Purge( $\text{N}_2$ , 30s). In both cases, the number of repetitive ALD/VPI cycles was 200.

### 3.2.2- Characterization

TEM characterization and EDS analysis were carried out with a FEI Titan microscope using 300 kV in STEM mode and an EDAX SDD detector.

Density functional theory (DFT) was applied to compute the electronic structure of oligomers of Kevlar and ZnO-infiltrated Kevlar in vacuum. The Perdew–Burke–Ernzerhof (PBE) exchange-correlation functional<sup>109</sup> was used with the SV(P) basis set (split valence with polarization at all non-hydrogen atoms) as implemented in TURBOMOLE<sup>110</sup> with the resolution of the identity (RI) approximation for Coulomb integrals<sup>111</sup> accompanied by the corresponding auxiliary basis sets<sup>112</sup>. The “m4” integration grid of the module RIDFT was used<sup>113,114</sup>. Geometries were freely optimized using redundant internal coordinates<sup>115</sup> until gradients were  $<10^{-6}$  Hartree/Bohr. Optimized structures were visualized with Materials Studio version 7.0. The computed system was composed of a total of 8 rings of Kevlar in the gas phase. Two adjacent oligomers, each consisting of four covalently bound monomers, were connected via three hydrogen bonds. This meant that the two central monomers of each oligomer, along with the central hydrogen bond, are likely to experience an environment representative of the polymer chain. Computing the structure in the gas phase meant that the geometry of the oligomers with and without ZnO could be freely optimized without imposing any particular periodic lattice. To model the infiltrated sample, the H of all three hydrogen bonds were replaced with [Zn(OH)] cross-links. The theoretical part of the work was performed by the group of Dr. Simon Elliott at the Tyndall National Institute in Cork, Ireland.

The XRD patterns of the samples were measured with a PANalytical X'Pert Pro diffractometer with Cu- $K_{\alpha}$  radiation. For an easier measurement, woven fabric Kevlar pieces were analysed, instead of individual fibres.

The FTIR spectra were carried out in a Perkin Elmer Frontier spectrometer with an ATR sampling stage. All spectra were measured with 20 scans from 520 to 4000  $\text{cm}^{-1}$  at 4  $\text{cm}^{-1}$  resolution. Each sample was measured 5 times and the results averaged.

The thermal stabilities of the samples were analysed using a DTG-60 Shimadzu Thermobalance. The samples (5-10 mg) were heated from room temperature to 700°C. The scanning rate was 10°C  $\text{min}^{-1}$  and all measurements were carried out under nitrogen atmosphere. The thermo gravimetric analyses were

performed by Dr. Leire Ruiz-Rubio in the Macromolecular Chemistry Laboratory of the Basque Public University (UPV).

The tensile tests were done with a BRUKER Universal Mechanical Tester with a resolution of 50  $\mu\text{N}$  and in accordance to the ASTM standard C1557-03 (2008). To determine the stability of the fibres under UV light the samples were exposed to light with a wavelength of 365 nm for 24 hours. Subsequently the strain-stress curves were measured and compared with the mechanical properties of unexposed fibres.

### 3.3.- Results and discussion

In order to evaluate the efficiency of the infiltration process we compared cross-sections of ZnO-infiltrated Kevlar fibres (I-ZnO) and ZnO-coated Kevlar fibres (C-ZnO). Figure 3.1 shows the TEM images and EDS colour maps of the cross-sectioned area of both samples.

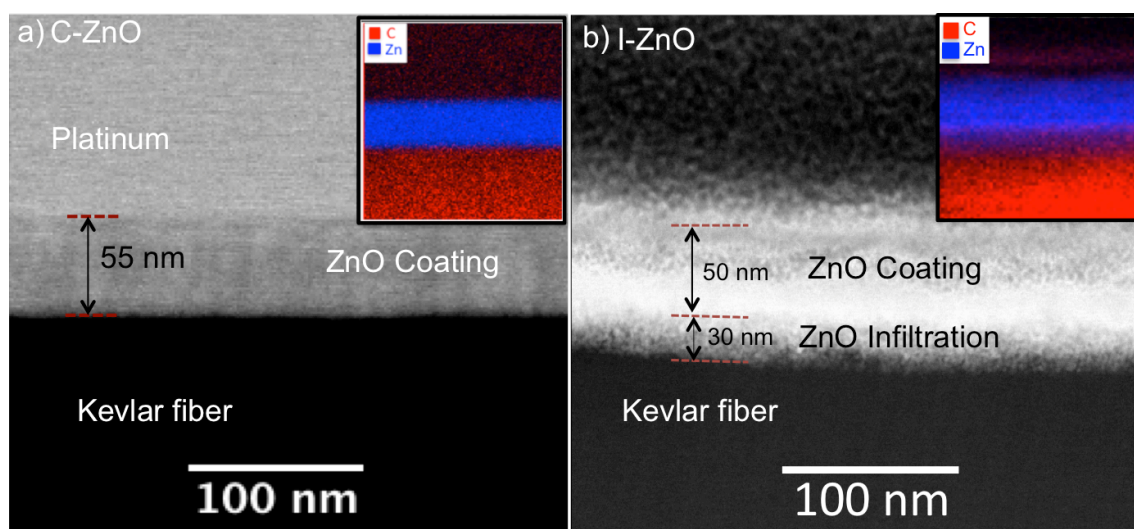


Figure 3.1: TEM images of cross-sections of a) C-ZnO and b) I-ZnO fibres. Insets show EDS colour maps with the carbon signal coded red and the zinc signal coded blue.

The TEM image shows that, even if the aim of the VPI processing is the ZnO infiltration into Kevlar, an unavoidable ZnO layer is created on top of the VPI processed sample. This is a consequence of VPI being an ALD-derived technique, thus a coating will always occur in parallel to the infiltration. However, a clear

difference between the coated and the infiltrated sample is shown, specifically at the interface between the ZnO layer and the fibre surface. In the case of C-ZnO, this interface is sharp and clear, while in the case of I-ZnO, it is blurred with a gradual decay of the Zn signal down to 30 nm depth below the surface of Kevlar. In this subsurface area, the Zn appears distributed as a ZnO network embedded into the polymer. Therefore, successful infiltration of Kevlar fibres with ZnO through VPI is confirmed.

Based on the literature, we expected the infiltrated ZnO to interact with the Kevlar chains creating a hybrid metal oxide-polymer material. Previous studies of ZnO ALD<sup>116,117</sup> indicate that DEZ adsorbs to Lewis basic sites (such as carbonyl O or amide N of Kevlar) and that transfer of the most acidic proton (here the amide NH) causes an ethyl ligand to be eliminated as ethane. The remaining ligand is eliminated in the H<sub>2</sub>O pulse, producing an OH group on Zn. In standard ALD, this hydroxyl group would react during next DEZ pulse, acting as a nucleus for the growth of a cluster or film of ZnO.

Based on that, substitution of the amide-H<sup>+</sup> of Kevlar with [Zn(OH)]<sup>+</sup> was expected in the case of the I-ZnO Kevlar sample. The probability of such chemical reactions between the used precursors and the polymer backbone were modelled by density functional theory (DFT). A system of two adjacent Kevlar strands, with 4 aromatic rings in each one, was used as model for the calculations. As shown in Figure 3.2a, the initial reaction between the infiltrated DEZ/water and Kevlar (simulating the first VPI cycles) consisted of the replacement of the amide protons with [Zn(OH)]<sup>+</sup>. It can be seen that the inter-chain H-bonds have been substituted with an ionocovalent N-Zn(OH)-O cross-linkage. This substitution causes an increase of the interchain distance, as the computed bond lengths for N-H and H-O were 1.03 Å and 2.09 Å, respectively, and changed to N-Zn and Zn-O bonds with 1.94 Å and 2.08 Å lengths. The creation of the Zn-O bond is accompanied by the stretching of the amide C=O bond, which changes from 1.24 Å to 1.27 Å. The computed reaction energy (including the evolution of ethane) is -115 kJ/mol per Zn atom, relative to the energies of DEZ and H<sub>2</sub>O in the gas phase.

When the reaction between this initial cross-linked model and DEZ/water was computed, simulating continued processing with VPI cycles, two energetically

similar reaction pathways were possible, namely (i) continued crosslinking through the replacement of H-bonds with new ionocovalent linkages and (ii) growth of ZnO clusters at each existing Zn(OH) nucleus within the system. For one cycle of the latter process, we computed an energy gain of -113,5 kJ/mol per Zn (relative to the energies of gas-phase DEZ and H<sub>2</sub>O, including evolution of ethane), which is close to the energy gain upon cross-linking (-99,8 kJ/mol). We therefore foresee that the final structure after repeated VPI cycles is likely to consist of a hybrid material composed of both nanoclusters of ceramic ZnO and covalently cross-linked Kevlar chains.

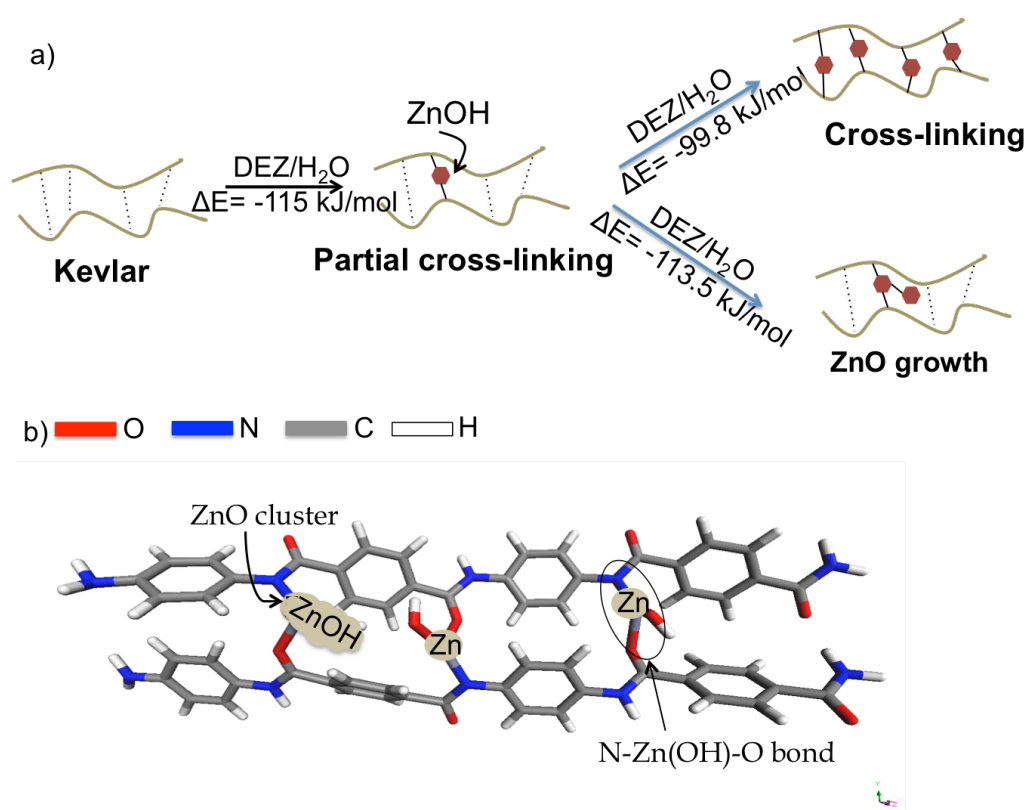


Figure 3.2: a) Schematic of the proposed reaction pathways of Kevlar with DEZ and H<sub>2</sub>O resulting from the energetically most favoured DFT-calculated chemical interactions b) Structure of the cross-linked I-ZnO Kevlar oligomer computed with DFT.

In order to corroborate the theoretically modelled structure, we performed XRD analysis of the samples. The XRD patterns of the samples are shown in Figure 3.3. Two main diffraction peaks can be observed in the pristine Kevlar XRD pattern, at 20.6° and 22.9°. These peaks correspond to the (110) and (200) crystal planes,

respectively, which are parallel to the axis of the polymeric chain<sup>118,119</sup>. The positions of the peaks and their full width at half maximum (FWHM) have been summarized in Table 3.1.

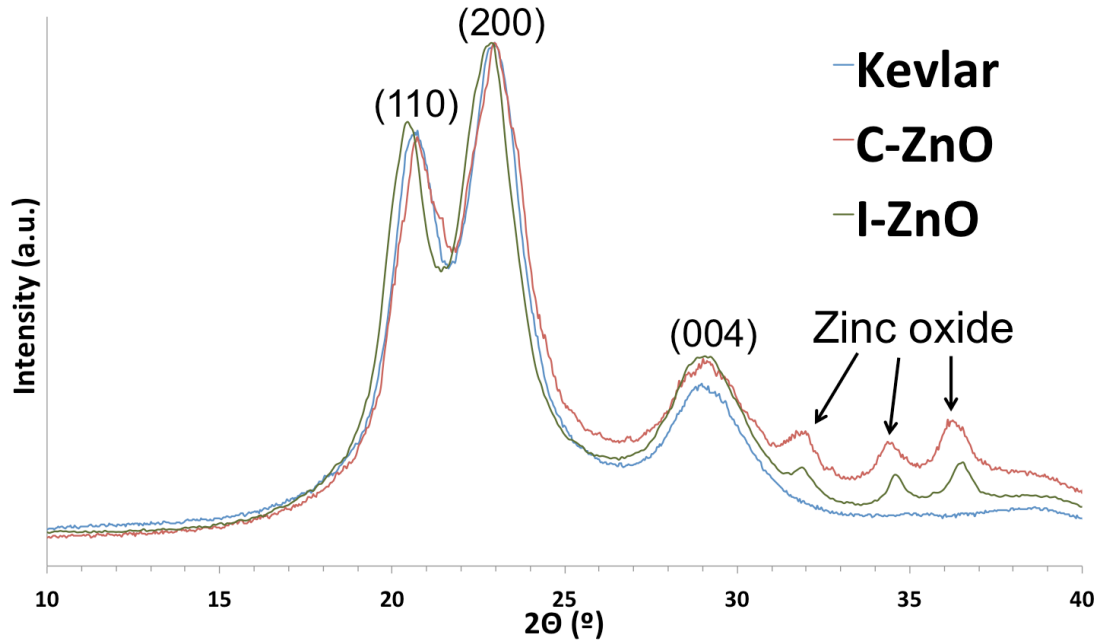


Figure 3.3: XRD patterns of pristine Kevlar, ZnO-infiltrated Kevlar (I-ZnO) and ZnO-coated Kevlar (C-ZnO) samples.

In the case of the I-ZnO sample, due to the infiltration of ZnO into Kevlar, a shift of both peaks towards smaller angles was observed. This shift indicates that the planes parallel to the polymeric chain stretch, confirming the theoretically predicted intercalation of ZnO between the polymeric chains. However, in the coated samples a different behaviour of the diffraction peaks was observed. Only a small shift towards larger angles occurred, which likely resulted from compressive stress induced by the inorganic coating on top of the sample. Besides, the FWHM of the coated sample increased, indicating a decrease of the crystallite size. The reduction of the crystallite size may arise from the scission of the superficial Kevlar chains resulting from the strong reactivity of the precursor and the heat evolution during the strongly exothermic reaction with water. The same effect should be observed in the I-ZnO samples, as the VPI process results not only in ZnO infiltration but also in a ZnO film on top of the sample. However, this effect is largely compensated

through cross-linking of the polymer chains with Zn in the case of the infiltrated sample.

Table 3.1: Change of the position and FWHM of the XRD peaks.

	Peak 1 (110)		Peak 2 (200)	
	Position (°)	FWHM	Position (°)	FWHM
Kevlar	20.6	0.83	22.9	0.90
C-ZnO	20.6	0.86	23.0	0.99
I-ZnO	20.4	0.82	22.7	0.90

In order to seek more experimental verification of the computed structure, we measured ATR-FTIR spectra of the samples (Figure 3.4a). No significant differences were observed between C-ZnO and native Kevlar, indicating that no significant changes were induced in the chemical structure of Kevlar upon coating with ZnO. In the case of the I-ZnO sample, if the model of cross-linking the polymer chains with Zn holds true, the changes in the bonding structure upon infiltration with ZnO should be reflected in the FTIR spectra (Figure 3.4a). It should be noted that the mole fraction of the modified area of Kevlar after infiltration is very small and the signal of the unmodified Kevlar from the bulk of the fibres is overwhelming. Therefore the spectra will have significant contribution from unmodified Kevlar. Nevertheless, a shift was observed from most of the amide peaks, confirming that the infiltrated Zn interacts with the amide groups. The individual wavenumbers of these peaks are depicted in the Table 3.2 for easier comparison.

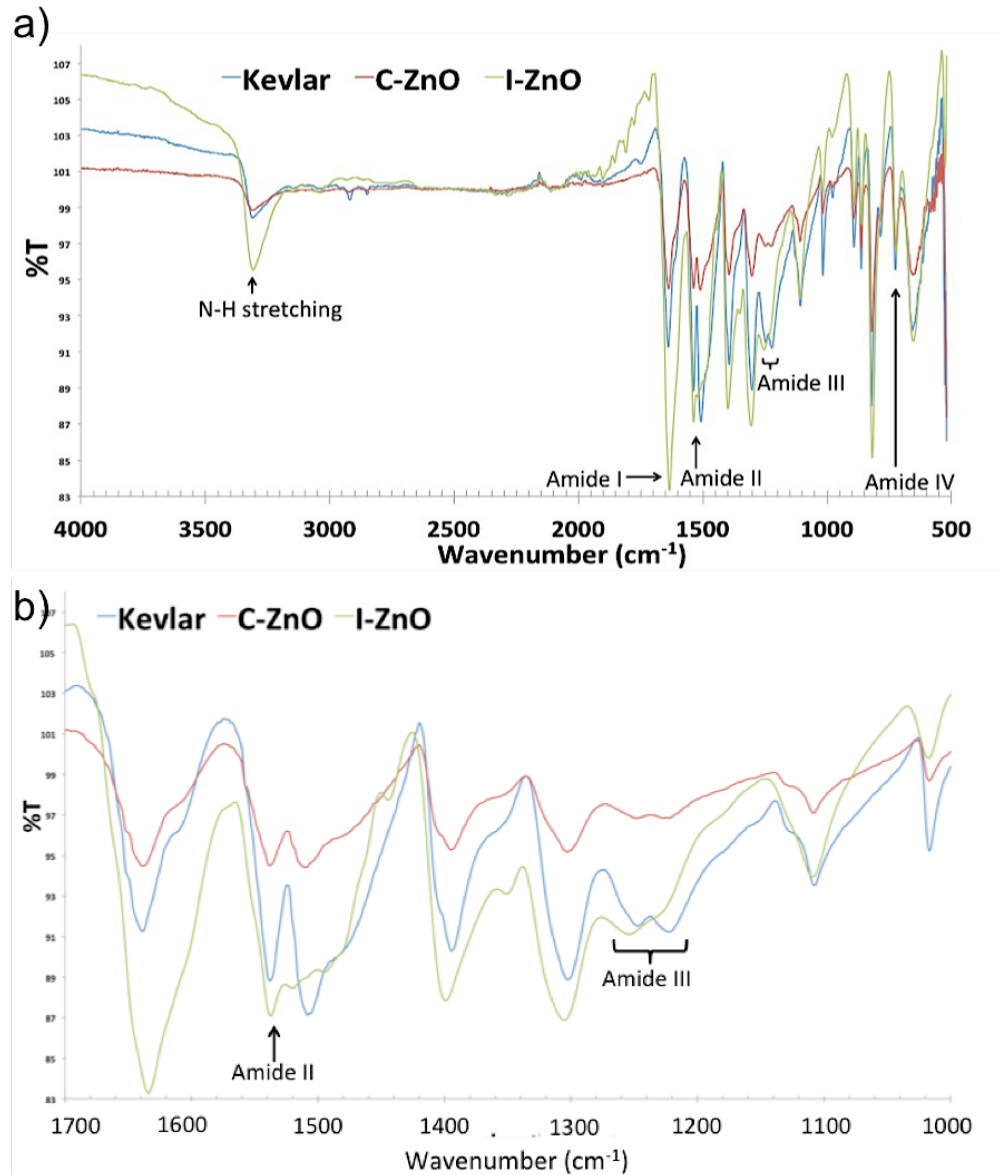


Figure 3.4: a) ATR-FTIR spectra of the various investigated samples. The peaks related to the amides are labelled; b) Magnification of the area showing the Amide II and III vibration peaks.

Table 3.2: Position of the FTIR amide-related peaks.

Peak	Kevlar	C-ZnO	I-ZnO
<b>N-H stretching</b>	3310	3311	3306
<b>Amide I</b>	1641	1641	1636
<b>Amide II</b>	1539	1540	1539
<b>Amide III</b>	1249 1222	1250 1224	1254 1227
<b>Amide IV</b>	727	726	721

The broadening (full width at half maximum (FWHM) increase by  $6\text{ cm}^{-1}$ ) and red shift of the N-H stretching band after infiltration clearly show an interaction of the precursor with the amide. The theoretically predicted stretching of the C=O bond is reflected in the experimentally observed redshift of the Amide I peak (a signature of stretching of C=O). The Amide II and Amide III peaks show a clear deformation compared to the peaks of the untreated Kevlar (Figure 3.4b) in addition to the blue shift of Amide III. These peaks correspond to the coupling of two vibrational modes, N-H bending and the C-N stretching and are commonly used to determine the secondary structure of proteins<sup>120-122</sup>, which can be applied to Kevlar in a similar way. The shift and shape change of the Amide II and III peaks must result from the change in the intermolecular interaction of the polymer chains and their spatial conformation, which is induced by the infiltration of ZnO into the polymer fibre. If further considering the red shift of Amide I and the blue shift of Amide III, which is dominated by the C-N stretching, this implies that a binding of Zn to the O in C=O will have a stabilizing effect on the C-N bond. In summary, the spectroscopic data is in agreement with the theoretically predicted cross-linked structure.

Once the structure of the ZnO-Kevlar hybrid was determined, we analysed the effect of the hybridization on the thermal and UV stability of Kevlar.

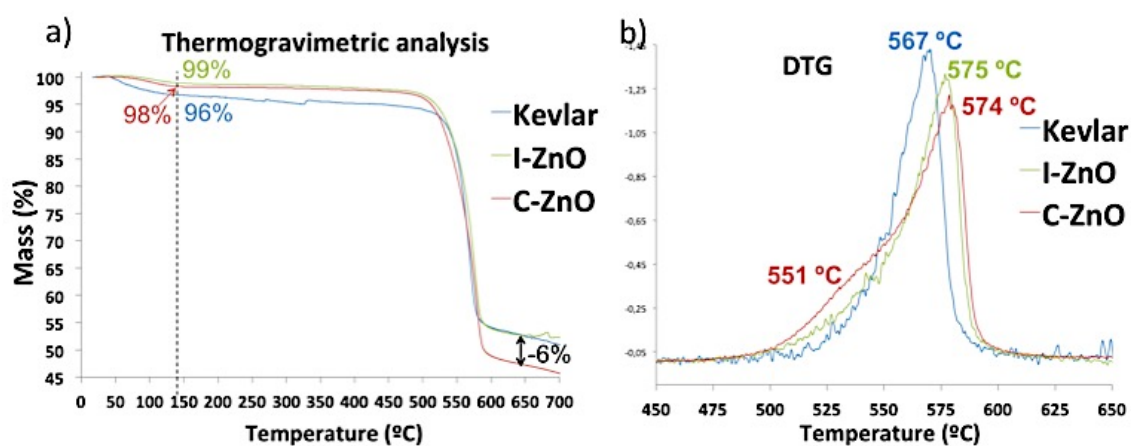


Figure 3.5: a) Thermogravimetric analyses showing the mass loss of each sample as a function of temperature, b) Derivative thermogravimetric plots showing the main degradation temperature of each sample. The temperature values of the C-ZnO sample correspond to the maxima of the deconvoluted peaks.

Regarding the thermal stability, as a result of the N-Zn-O bonding, an increase of the degradation temperature was expected. A more quantitative picture can be extracted from the thermogravimetric analysis (TGA) and differential thermogravimetry (DTG) measurements shown in Figure 3.5. Untreated Kevlar lost about 4% of the initial mass at 150°C (corresponding to the processing temperature) and the decomposition of the polymer occurred at 567°C, which is in good agreement with previous studies<sup>123</sup>. The mass loss at 150°C of both ZnO-treated samples is similar and slightly lower than the loss observed from the untreated Kevlar. The main decomposition of these samples occurred at slightly higher temperatures (around 575°C) than of the untreated samples. However, in the case of the C-ZnO sample a shoulder at 551°C is observed, which is not seen in the I-ZnO sample. This shoulder indicates that an additional decomposition process starts prior to the main decomposition, which may follow a different degradation mechanism. A very likely scenario is that upon coating with ZnO the water molecules contained within the Kevlar fibres get trapped by the coating and cannot be released at 150°C as it occurs with untreated Kevlar. An evidence for this can be seen from the TGA curves of the samples in the early stage of heating, between 50°C and 150°C, where the untreated Kevlar shows a continuous mass loss corresponding to the absorbed water molecules evaporation, while the ZnO treated samples do not. At higher temperatures the pressure of the water vapour will rise, causing the ZnO coating cracking, potentially hand in hand with a recrystallization of the ZnO. Indeed, in our earlier work we showed that temperatures of around 500°C are sufficient to recrystallize ALD-deposited ZnO on polymeric fibres<sup>124</sup>. The high temperatures and the presence of released water molecules will cause the C-ZnO Kevlar to start decomposing already at 520°C<sup>78,125</sup>. The FTIR spectra of the decomposition gases released at 520°C, shown in Figure 3.6, support this scenario, as it can be observed that just the C-ZnO sample started to degrade at 520°C. This additional degradation step of the C-ZnO may be responsible for the final loss in mass of 6%. The presence of smaller molecular fragments that result from chain scission, as indicated by XRD, may contribute to the enhanced mass loss and earlier induction of the degradation in the coated sample.

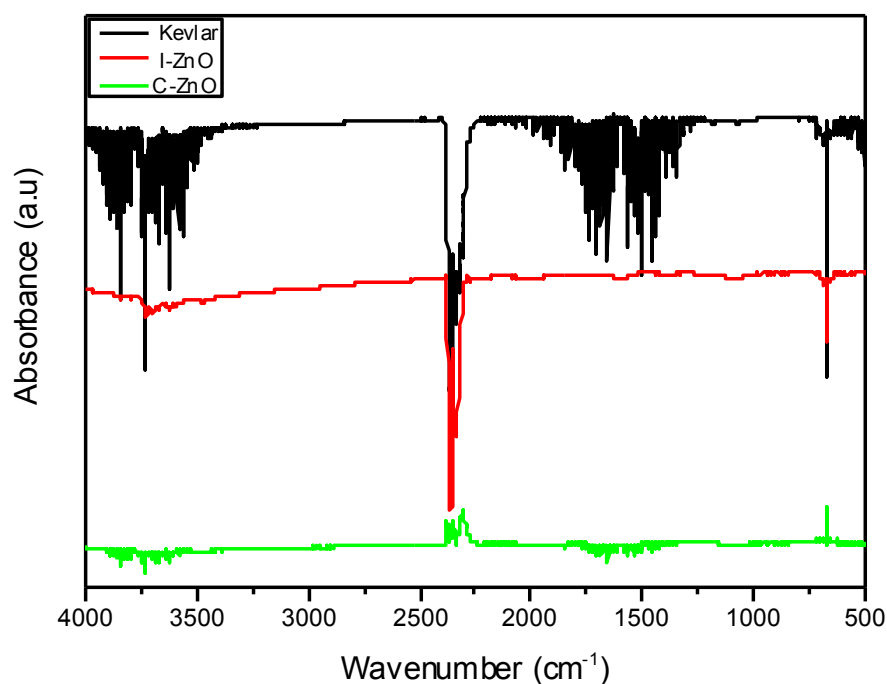


Figure 3.6: FTIR spectra of the evolving gases upon decomposition at 520 °C. In the case of untreated and I-ZnO samples, the absorbance is negative as no gases are released.

In the I-ZnO fibres the delayed water molecule release was less expressed. The reason may be that a significant amount of water molecules within the Kevlar is consumed by the DEZ during the infiltration process, thus the degradation process occurs in a largely inert atmosphere. Therefore, it is confirmed that the infiltration and hybridization of Kevlar with ZnO enhances the thermal stability of the polymer.

As mentioned in section 1.4 of this thesis, exposing Kevlar to high temperatures for long periods of time has an enormous impact on its mechanical properties. In order to verify whether or not the observed increase in thermal stability of I-ZnO Kevlar is also reflected in its mechanical properties, we performed tensile tests. From the obtained stress-strain curves, we calculated the toughness modulus (area under the strain-stress curve) of the samples, which are summarized in Figure 3.7. As a reference, an untreated Kevlar sample was maintained at 150 °C for 7h, which should simulate the environmental conditions the fibres experience during the coating or infiltration processes. As expected, this thermal treatment had a large impact in the toughness modulus of Kevlar, as only 75% of the initial modulus was retained after 7h. Similar results were obtained with the C-ZnO

sample, indicating that the ZnO layer on top of the fibres was not sufficient to avoid thermal degradation. However, the infiltrated sample retained 91% of the initial modulus, confirming its enhanced thermal stability as observed in the TGA measurements.

After assessing the benefit of the infiltration on the thermal sensitivity, we analysed the UV sensitivity of the samples. We exposed the fibres to UV light for 24h and performed the tensile tests. A comparison of the modulus of toughness before and after exposure to UV light (Figure 3.7) showed the high sensitivity of Kevlar to such irradiation.

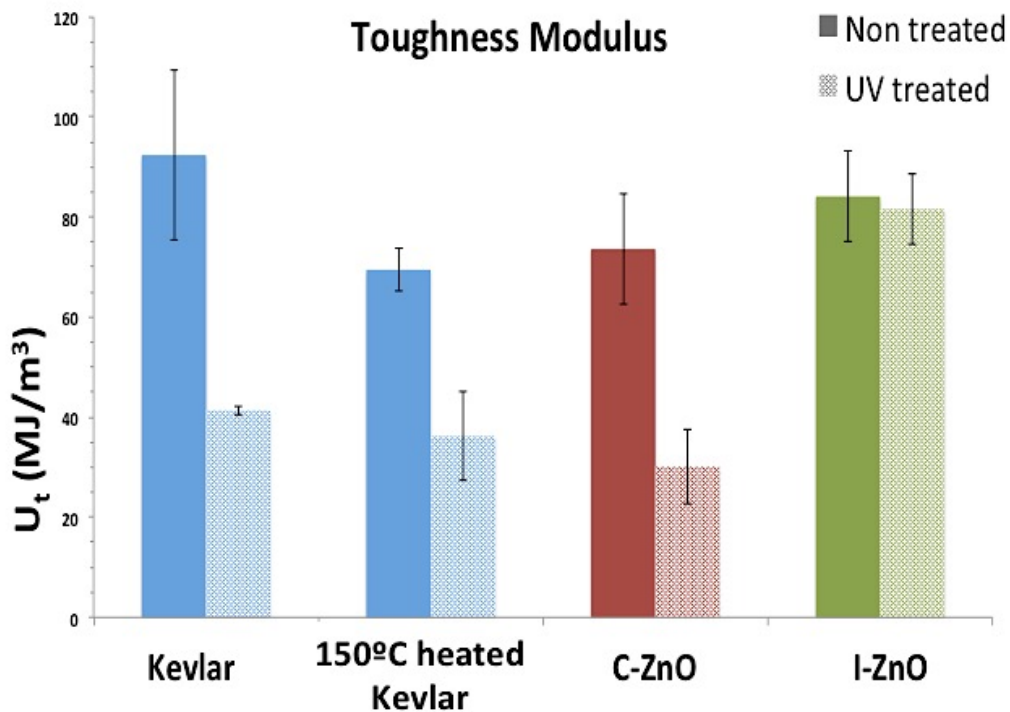


Figure 3.7: Modulus of toughness of the various processed samples before and after UV irradiation.

The modulus of toughness of both untreated and heated Kevlar decreased by nearly 50%. The destructive effect of UV light on the mechanical properties is a direct consequence of molecular decomposition reactions that take place on the fibres' surfaces<sup>80,103,126</sup>. The UV light induces hydrogen bond cleavage, chain scission and oxidation of terminal groups of the polymer. Those primarily affect the amide groups and lead to a degradation of the superficial hydrogen bonds, resulting in

surface etching. This effect may be enhanced if elevated temperatures are combined with UV irradiation. The superficial degradation reactions can be observed from the FTIR spectra of the Kevlar samples before and after the irradiation. Even though no evolution of a new peak was observed after irradiation, the intensity of the amide-related peaks changed significantly. For a clearer comparison, the spectra were normalized and the change on the intensities has been summarized in Table 3.3.

Table 3.3: Change of the intensities of the amide-related peaks after UV irradiation.

Sample	Intensity variations after UV irradiation (%)			
	N-H <sub>st</sub>	Amide I	Amide II	Amide III
Kevlar	-7	2	2	-3
Heated Kevlar	-160	2	4	-6
C-ZnO	-5	7	2	-2
I-ZnO	-1	0	1	0

The reduction of the intensity of the N-H stretching and Amide III bands, together with the increased intensity of the Amide I and II bands, as observed in the untreated Kevlar, arise from the cleavage of H-bonds between adjacent chains and a homolytic splitting of C-N and N-H bonds<sup>80,125,127</sup>. The heated Kevlar sample showed the same tendency but the change in the intensities, especially of the N-H stretching peak, was considerably larger. In this case, the UV-induced H-bond cleavage and chain scission reactions were combined with a thermally induced H-bond cleavage. This was in good agreement with the tensile tests where the modulus of toughness of heated Kevlar after UV irradiation was even lower than in the case of untreated Kevlar.

In the case of C-ZnO fibres, an even stronger loss of the modulus of around 65% was observed (Figure 3.7), indicating that the degradation reactions were further enhanced by the ZnO coating. ZnO is known to strongly absorb UV light. The coating was therefore expected to shield the fibres from UV light and prevent radiation-induced degradation. However, for a quantitative UV blocking a film of around 100 nm thickness is typically needed<sup>86,128</sup>. Since our films had only approximately half of that thickness, the UV blocking of the ZnO coating is not expected to be efficient. Furthermore, under UV illumination and in presence of

water molecules, the ZnO coating acted as a photocatalyst, creating oxygen-containing radicals that can attack the polymeric backbone. Such photocatalytic side reaction will rapidly degrade the polymer in the vicinity of the metal oxide and in this way lower the modulus of toughness. In fact, we observed the most significant loss in the modulus of toughness from coated samples after UV irradiation. The different degradation mechanism of the C-ZnO sample was also expressed in the FTIR spectra (Table 3.2). Unlike pristine and heated Kevlar, where the changes in the N-H peak are most dominant, in this case the biggest change occurs in the Amide I peak. The increased intensity of the C=O stretching peak (Amide I) is accompanied by a shift towards higher wavenumbers as a consequence of the oxidation of the amide groups.

In contrast, the infiltration with ZnO effectively suppressed UV induced degradation; the I-ZnO fibres retained 90% of the initial modulus of toughness (Figure 3.7). The UV protection is also reflected in the FTIR spectrum (Table 3.2), as almost no change in the intensities of the amide-related peaks was observed. This stabilization may be explained as follows. On the one hand chain-scission reactions become less probable in the case of polymer chains that are cross-linked and stabilized with Zn. Especially with the Zn binding to amide groups, those will experience chemical stabilization and potentially shield the amide bonds from reactive molecules. On the other hand the infiltrated ZnO is buried in the subsurface area of the fibre without contact to water molecules, thus suppressing radical formation as source for the UV-induced photocatalytic degradation observed in the C-ZnO sample. Most likely both effects played a partial role here and apply simultaneously.

### **3.4.- Conclusions**

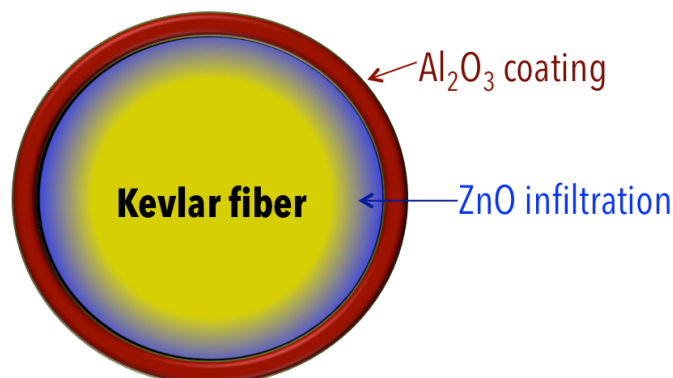
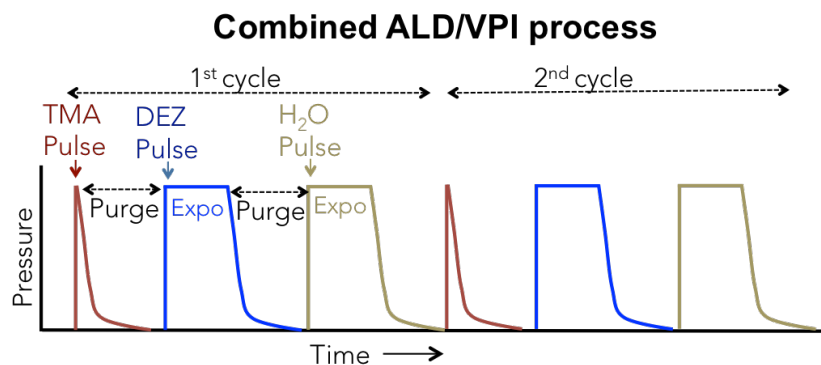
The stability of Kevlar fibres against thermal and UV irradiation-induced degradation has been significantly improved through vapour phase infiltration of Kevlar with ZnO. As a consequence of the infiltration, a hybrid organic-inorganic material of around 30 nm thickness is created in the subsurface area of the Kevlar fibres. The structure of the hybrid material, which is determined by theoretical models calculated with DFT, consists of infiltrated ZnO, which is covalently cross-

linking Kevlar chains and further growing inside the polymeric matrix. The shift in the vibration peaks of the amide groups observed in the FTIR spectrum indicates that the infiltrated ZnO reacts with the amide group, which is in agreement with the theoretical model. Thanks to the creation of the hybrid material the decomposition temperature of Kevlar is increased by nearly 10°C and 90% of its modulus of toughness is retained even after 24h of UV irradiation, outperforming the stability of Kevlar as known by now. Thus, this new route offers the possibility to improve the stability of such high-strength polymers without markedly compromising their characteristic lightness. In addition, this vapour phase technique avoids the post processing treatments that are commonly required after use of organic solvents.

## Chapter 4

### Combined ALD/VPI process for multiscale functionalization of Kevlar

In this chapter, a newly developed combined ALD/VPI process is described, which is used for simultaneous toughening and UV protection of Kevlar fibres. This new combined process allows simultaneous coating of Kevlar fibres with  $\text{Al}_2\text{O}_3$  and infiltration with ZnO within the same run. As elaborated in the previous chapter, the Kevlar-ZnO hybrid material synthesized in the subsurface area of the fibres suppresses the UV sensitivity of the polymer. The evolution of this process towards additional coating with  $\text{Al}_2\text{O}_3$  enhances the modulus of toughness of the fibres by 10%, eventually resulting in reinforced and UV resistant Kevlar fibres, as described in more detail in this chapter.





## 4.1.- Introduction

In the previous chapter, we demonstrated that the thermal and UV sensitivity of Kevlar can be suppressed by infiltration of ZnO through a modification of ALD, namely, Vapour Phase Infiltration (VPI). Apart from the desired infiltration, the VPI of ZnO into Kevlar also resulted in unavoidable coating of the polymer with ZnO. However, we found that this ZnO coating had a negative impact on the stability of the fibres and only 90% of the modulus of toughness was retained in this way. Therefore, if the ZnO coating could be suppressed or substituted with a non-photocatalytic material, the performance of the ZnO infiltrated Kevlar fibres might be improved.

The development of a process for polymeric fibres to be infiltrated with a metal oxide and coated with another metal oxide in a single vapour phase processing step is very challenging. However, such combination of two different metal oxides infiltrating/coating the polymeric substrate could lead to a rapid and simple synthesis of multifunctional polymers, which could include functionalities that are difficult to obtain in other ways.

In this chapter, we demonstrate a new process, which integrates both coating and infiltration with two different materials. Through this combination of ALD/VPI Kevlar fibres are coated with Al<sub>2</sub>O<sub>3</sub> and infiltrated with ZnO within the same process. The mechanical properties and UV stability of these fibres are studied and compared to Al<sub>2</sub>O<sub>3</sub>-coated and infiltrated fibres. Thanks to this new strategy, Kevlar's modulus of toughness is increased by 10% and its sensitivity to UV-induced degradation is completely eliminated at the same time.

## 4.2.- Experimental

### 4.2.1.-Sample preparation

Kevlar fibres were obtained from the woven commercially used in bulletproof vests (Kevlar 29). The fibres had diameters of 10 µm and were cut to lengths of 3 cm for the experiments.

All modifications of the samples were performed in a commercial ALD reactor (Savannah S100, Cambridge NanoTech Inc). Both infiltration and coating of the fibres were carried out at 150°C under a constant nitrogen gas flow of 20 standard cubic centimetres per minute (sccm). Trimethylaluminum (TMA,  $\text{Al}(\text{CH}_3)_3$ , Strem Chemicals) was used as the aluminium source, Diethylzinc (DEZ,  $\text{Zn}(\text{C}_2\text{H}_5)_2$ , Strem chemicals) was used as zinc source, and demineralized water as the oxygen source. The coated fibres were prepared following a typical ALD process with a cycle consisting of Pulse(TMA, 0.08s)/Purge( $\text{N}_2$ , 30s)/ Pulse( $\text{H}_2\text{O}$ , 0.08s)/Purge( $\text{N}_2$ , 30s). In contrast, the infiltrated fibres were prepared by VPI. Here, the substrate was exposed to the precursors for defined periods of time before purging, thereby allowing diffusion of the precursors into the polymer. A VPI cycle consisted of Pulse(TMA, 0.08s)/ Exposure(30s)/ Purge( $\text{N}_2$ , 30s)/ Pulse( $\text{H}_2\text{O}$ , 0.08s)/ Exposure(30s)/ Purge( $\text{N}_2$ , 30s). Finally, for the preparation of the sample coated with alumina and infiltrated with ZnO a combination of ALD and VPI was used. Each cycle consisted of Pulse(TMA, 0.08s)/ Purge( $\text{N}_2$ , 30s)/ Pulse(DEZ, 0.08s)/ Exposure(30s)/ Purge( $\text{N}_2$ , 30s)/ Pulse( $\text{H}_2\text{O}$ , 0.08s)/ Exposure(30s)/ Purge( $\text{N}_2$ , 30s). In all cases, the number of repetitive ALD/VPI cycles was 200.

#### 4.2.2.- Characterization

TEM characterization and EDS analysis were carried out with a FEI Titan microscope using 300 kV in STEM mode and an EDAX SDD detector.

The FTIR spectra of the samples were acquired with a Perkin Elmer Frontier spectrometer with an ATR sampling stage. All spectra were measured collecting 20 scans in the range from 520 to 4000  $\text{cm}^{-1}$  with 1  $\text{cm}^{-1}$  resolution. Each sample was measured 5 times and the results were averaged.

The XRD patterns of the samples were measured with a PANalytical X'Pert Pro diffractometer with  $\text{Cu-K}_\alpha$  radiation. For an easier measurement, woven fabric Kevlar pieces were analysed, instead of individual fibres.

The tensile tests were done with a BRUKER Universal Mechanical Tester with a resolution of 50  $\mu\text{N}$  and in accordance to the ASTM standard C1557-03 (2008). To determine the stability of the fibres under UV light the samples were exposed to

light with a wavelength of 365 nm for 24 hours. Subsequently the strain-stress curves were measured and compared with the mechanical properties of unexposed fibres.

The morphology of the fibres after the tensile tests was analysed by SEM. The SEM micrographs were taken in an environmental scanning electron microscope Quanta 250 FEG with a large field detector (LFD). The ruptured fibres were glued to a carbon tape and the images were taken at 10 kV and 70 Pa.

### 4.3.- Results and discussion

In order to analyse the structure of the samples resulting from the different processes, we analysed their cross-sectioned areas with TEM (Figure 4.1). Alumina-coated Kevlar fibres (C- $\text{Al}_2\text{O}_3$ ) had a sharp and clear interface between the  $\text{Al}_2\text{O}_3$  thin film and the polymeric core (Figure 4.1a). Similarly, an alumina thin film was grown on the surface of the alumina infiltrated (I- $\text{Al}_2\text{O}_3$ ) sample. However, in this case the TMA additionally diffused into the polymer and formed a second, less dense  $\text{Al}_2\text{O}_3$  layer in the subsurface area of the polymer (Figure 4.1b). The sample prepared by the combined ALD/VPI process (TMA pulse) showed a more intriguing construction. Here, two different metal oxides were present,  $\text{Al}_2\text{O}_3$  as a thin film on the surface of the fibre and ZnO as the inorganic component of the hybrid material created in the subsurface area of the polymer (Figure 4.1c and 4.1d). This special stack was achieved by the combination of ALD and VPI in a novel single-stage process. Namely, the process starts with an ALD-type pulse of TMA, that is, a short pulse of the precursor without allowing exposure time, which is followed by a purge step. In this stage, the TMA covalently binds to the surface of the fibre but is not hydrolysed yet. It acts as inhibitor for the adsorption of the next precursor by occupying functional sites at the polymer surface. In the next step of the process a VPI-type of pulse of DEZ is applied, which includes exposure of the sample to DEZ for an extended time period. As the superficial functional groups are saturated with TMA, the DEZ diffuses into the fibre and reacts with the functional groups in the subsurface area of the polymer. The process is finished by a VPI pulse of water vapour, which reacts with both the anchored TMA and infiltrated DEZ. Upon reaction of water with TMA on the polymer surface, an  $\text{Al}_2\text{O}_3$  coating is created,

while the reaction with DEZ in the subsurface area forms a Kevlar-ZnO hybrid. The structure of this hybrid consists of ZnO clusters that covalently cross-link Kevlar chains through N-Zn-O bonds, as studied in the previous chapter of this thesis.

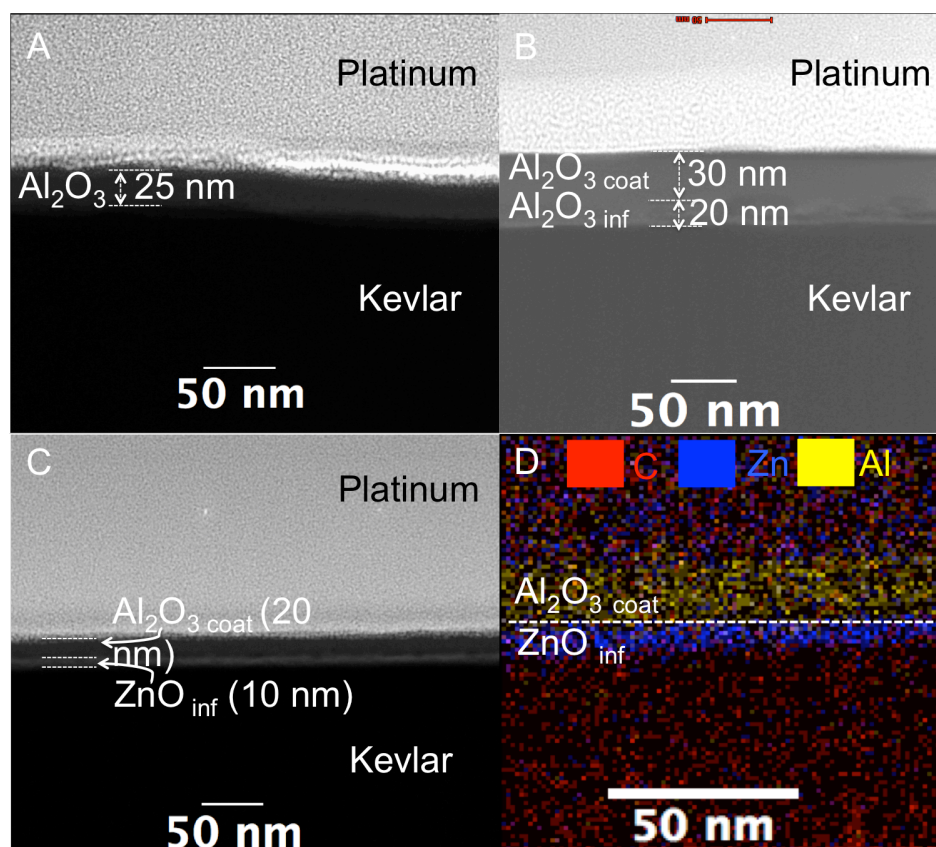


Figure 4.1: TEM images of FIB-prepared cross-sections of A) alumina-coated Kevlar (C-Al<sub>2</sub>O<sub>3</sub>), B) alumina-infiltrated Kevlar (I-Al<sub>2</sub>O<sub>3</sub>), and C) Kevlar coated with alumina and infiltrated with ZnO (TMA pulse). d) EDS colour map of the TMA pulse sample.

The chemical changes induced by the coating and infiltration processes were analysed by ATR-FTIR. The most pronounced differences among the characterised samples were seen in the fingerprint area of the FTIR spectra, specifically in the region between 950 and 1000 cm<sup>-1</sup> (Figure 4.2a), where stretching signatures of C-N, C-O and C-C bonds are found. A peak at 940 cm<sup>-1</sup> in the spectra of the C-Al<sub>2</sub>O<sub>3</sub> and I-Al<sub>2</sub>O<sub>3</sub> samples indicated the development of C-O single bonds, which was a result of the binding of the Lewis acid TMA to the oxygen of the C=O bond in the amide. An

additional peak developed around  $960\text{ cm}^{-1}$ , which can be assigned to C-C stretching, a result of newly developing C-C bonds. The intensity of that peak in the TMA pulse sample was low, likely showing a moderate level of chemical modification, while it is higher in the two  $\text{Al}_2\text{O}_3$ -coated and infiltrated samples. This new C-C bond results from the nucleophilic attack of the released methyl ligand of TMA on the carbonyl C of the C=O group in the amide. Such an attack will result in the splitting of the C-N bond in the amide in parallel to the formation of the C-C bond (Figure 4.2b). The native Kevlar and the TMA pulse sample showed a pronounced peak at  $980\text{ cm}^{-1}$ , a signature of the C-N bond, while this peak nearly vanished in the C- $\text{Al}_2\text{O}_3$  and I- $\text{Al}_2\text{O}_3$  samples. Therefore, it can be assumed that the alumina-treated samples are more strongly degrading the polymer chains.

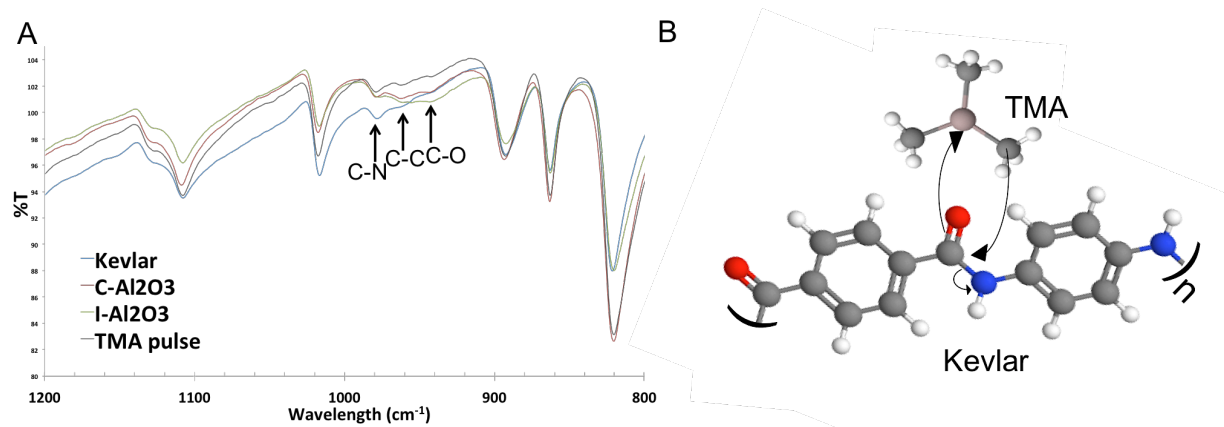


Figure 4.2: A) Fingerprint area ( $1200\text{-}800\text{ cm}^{-1}$ ) of the ATR-FTIR spectra of Kevlar fibres before and after coating and infiltration. B) Schematic view of the proposed reaction mechanism between Kevlar and TMA, based on the FTIR data.

The spectra at higher wavenumbers added further information. Shifts in the amide peaks confirmed that the infiltrated precursors interacted with the amide groups. The individual wavenumbers of these peaks are depicted in Table 4.1 for easier comparison.

Table 4.1: Position of the FTIR amide related peaks

	Kevlar	C-Al <sub>2</sub> O <sub>3</sub>	I-Al <sub>2</sub> O <sub>3</sub>	TMA pulse
N-H st	3310	3310	3308	3306
Amide I	1641	1642	1638	1639
Amide II	1539	1538	1540	1538
Amide III	1249	1251	1250	1251
	1222	1221	1224	1227

While the alumina coating (C-Al<sub>2</sub>O<sub>3</sub>) did not significantly alter the spectral signature of Kevlar, the other two samples showed chemical changes to the substrate. On the one hand both samples affect the N-H and C=O (Amide I) bonds, which constitute the hydrogen bonds between the polymer chains. However, the ZnO infiltration (TMA pulse sample) had a stronger impact on the N-H bonds than the Al<sub>2</sub>O<sub>3</sub> infiltration (I-Al<sub>2</sub>O<sub>3</sub> sample), while with the Amide I, the situation was reverse. This is in-line with the observations from the fingerprint area where Al was more efficiently binding to C=O than Zn, which on the other hand has a stronger impact on N-H than Al<sup>42</sup>. The blue-shifts of the Amide II and Amide III peaks indicate that both metals also interacted with the nitrogen, as those peaks are related to the C-N bond stretching. The shift was more strongly expressed after infiltration of ZnO, indicating once more stronger bonding of Zn to the N and a resulting alteration of the C-N bonding strength. Upon infiltration of Al<sub>2</sub>O<sub>3</sub>, the Al will more easily attack the carbonyl group and bind to the oxygen, converting the double bond into a single bond. The methyl group released from the TMA precursor upon binding of Al to O is a strong nucleophile and will likely bind to the carbonyl C. As a result, the C-N bonds will become cleaved. The shifts further indicate that covalent cross-linking of the Kevlar chains is more pronounced in the TMA pulse sample.

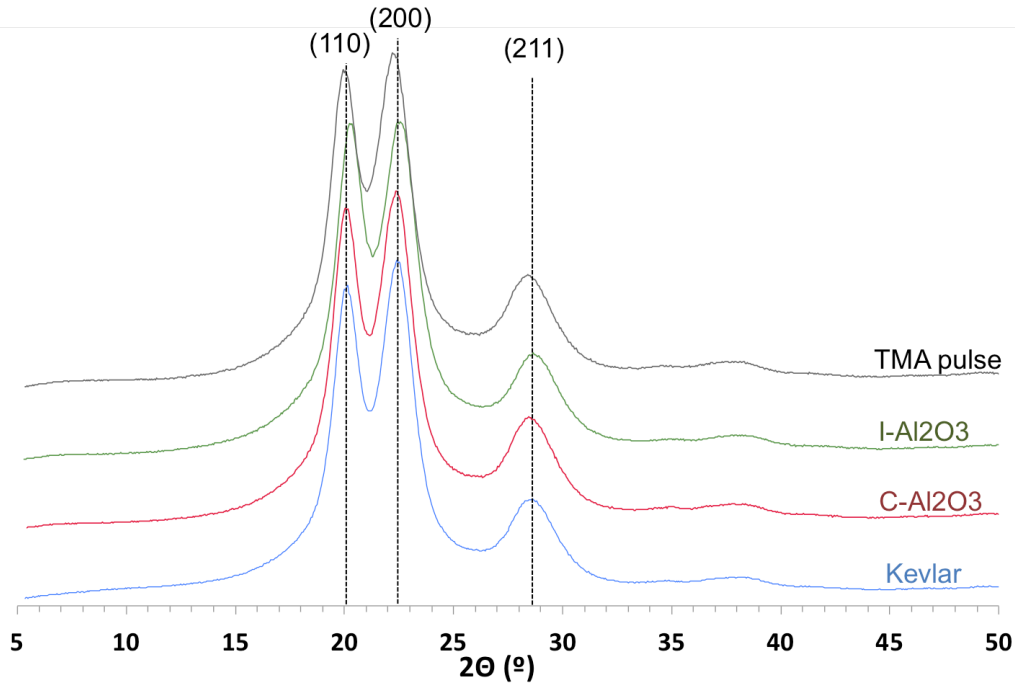


Figure 4.3: XRD diffraction patterns of the samples.

The crystallographic features of the samples by X-Ray diffraction (Figure 4.3) additionally confirmed the cross-linking ability of the infiltrated ZnO. Namely, the peaks indexed as [110] and [200] reflections of Kevlar shift to slightly lower angles after infiltration with ZnO, indicative of an increase of the interchain distance, likely resulting from insertion of ZnO into the material, thereby cross-linking the polymer chains. The shift of the [211] reflection points towards a decrease of the stacking density of the crystallites. In contrast, the C-Al<sub>2</sub>O<sub>3</sub> showed no alteration of the interchain spacing, but only a decrease in the stacking density. The I-Al<sub>2</sub>O<sub>3</sub> sample showed in both aspects opposite behaviour, namely a decrease of the interchain spacing and an increase in the packing density, which presumably results from the molecular distortion upon chain scission and re-packing of the molecules within the fibres.

In order to measure the impact of the different treatments on the mechanical properties of the fibres, we performed tensile tests and calculated the modulus of toughness. From Figure 4.4a it becomes obvious that in the first instance all processed samples showed an increase in the modulus of toughness as compared to native Kevlar. This effect can be ascribed to the alumina film created on top of each sample upon coating or infiltration. The inorganic coating stiffens the polymeric

fibre, which consequently increases the Young's modulus and the Ultimate Tensile Strength (UTS), resulting in an increased modulus of toughness. However, the stress-strain curves in Figure 4.4b show that the three treated samples performed differently. In the case of C- $\text{Al}_2\text{O}_3$ , the modulus of toughness increased by 13%, but the failure strain was significantly reduced in comparison to native Kevlar. In contrast, the infiltration of Kevlar with  $\text{Al}_2\text{O}_3$  (I- $\text{Al}_2\text{O}_3$ ) showed a somewhat different behaviour. The unavoidable alumina coating created during the infiltration process implies a similarity to the corresponding coated fibre. However, the strain-stress curve of this sample was similar to that of untreated Kevlar and the increase in the modulus of toughness was only 5%. One may expect that the formation of a hybrid phase of  $\text{Al}_2\text{O}_3$  and Kevlar in the subsurface area may further improve the mechanical properties of the fibre. However, given earlier evidence by the Parsons group<sup>129,130</sup> and our cross-sectional TEM investigations (Figure 4.1b), the precursor TMA, being a strong Lewis acid, is able to degrade the polymer and consequently form a porous  $\text{Al}_2\text{O}_3$  film at the interface of the coating and the bulk polymer. This porous film is likely an initially infiltrated and subsequently degraded part of the subsurface area of Kevlar. This spongy structure is more flexible than dense  $\text{Al}_2\text{O}_3$ , thus the I- $\text{Al}_2\text{O}_3$  sample dominantly reflects the characteristic high rupture strain of the Kevlar. However, no improvement in the Young's Modulus or UTS in comparison to the coated sample is observed, indicating that the alumina film is not tightly bound to the polymeric fibre.

The greatest improvement was observed from the TMA pulse sample, where the Toughness Modulus increased by 17%. This improvement results from the increase of the Young's Modulus and UTS and a higher failure strain. The sample consisted of ZnO infiltrated into the subsurface area of Kevlar and an additional coating with  $\text{Al}_2\text{O}_3$ . The greatly increased mechanical properties of this sample indicate that the Kevlar-ZnO hybrid acts as an ideal interface. It strongly binds the alumina film with the polymeric substrate and, at the same time, it is flexible enough to compensate the stress occurring from the differences in flexibility between the brittle inorganic coating and the flexible polymer.

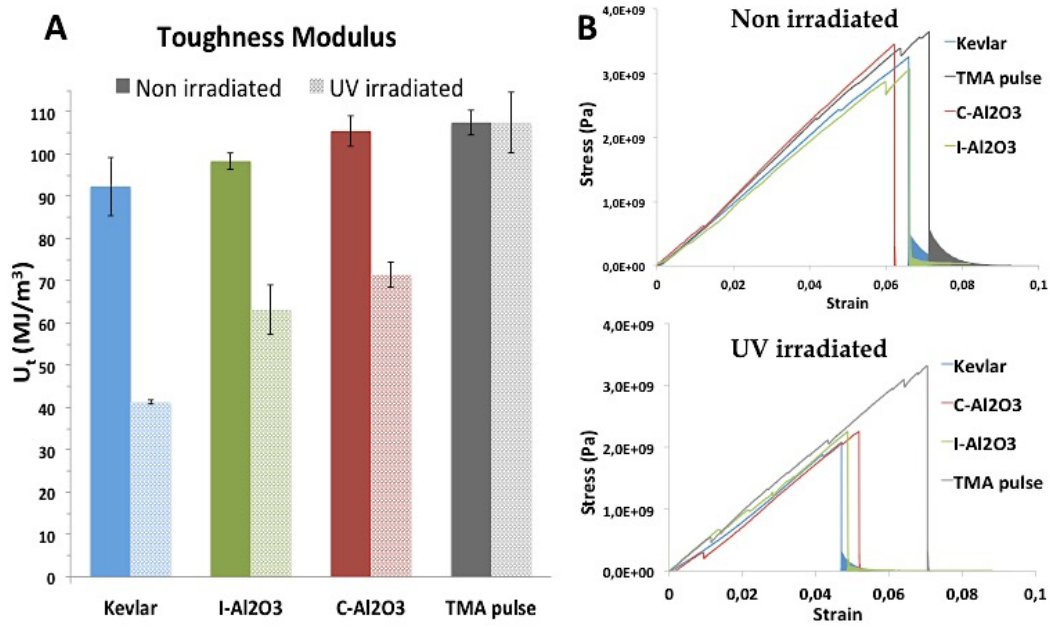


Figure 4.4: a) Modulus of toughness before and after irradiation with UV light, and b) Stress-strain curves before and after irradiation with UV light.

The mechanical properties of the coated and infiltrated samples were further analysed after exposing the fibres to UV light for 24 hours. From Figure 4.4a, we observed that the untreated Kevlar maintained only 45% of its modulus of toughness after exposure to UV light. The I-Al<sub>2</sub>O<sub>3</sub> and C-Al<sub>2</sub>O<sub>3</sub> samples showed higher UV resistance, maintaining 65% of their modulus of toughness. However, the UV light still had a significant impact on those fibres. The TMA pulse sample, however, showed significant improvement in resistance against UV light. In fact, a complete suppression of the UV sensitivity was observed with 100% of the Toughness Modulus being maintained even after exposure to UV light. The possibility to lower UV-induced degradation of Kevlar by infiltration with ZnO was already demonstrated in the previous chapter. The difference to the current sample is that in the previous approach the overall modulus of toughness of Kevlar was not improved, but merely the loss minimized. In contrast to those earlier investigated samples, the TMA pulse Kevlar fibres consist of infiltrated ZnO and an additional coating of Al<sub>2</sub>O<sub>3</sub>, which was achieved with a conceptually new synchronized coating-infiltration strategy. Advantage has been taken from the added value of two

materials, namely the infiltrated ZnO being an excellent UV-light absorber and the  $\text{Al}_2\text{O}_3$  coating enhancing the modulus of toughness.

Important information about the mechanical performance of a material can be extracted from the analysis of the fracture area. Figure 4.5 shows that the failure of Kevlar fibres is mainly caused by fibrillation and splitting along the fibre axis<sup>131,132</sup>. The rupture of the fibre starts at an imperfection on the surface. The longitudinal shear stresses, induced at the initial imperfection, cause longitudinal splitting of the first bundle of fibrils. The tensile modulus and strength are much higher than the shear modulus and strength, resulting in the crack developing under a steep angle. The break is further transmitted from one fibrillar unit to another until the filament fails completely<sup>133</sup>. The fracture area of the UV-irradiated sample, in contrast, showed negligible fibrillation. This fracture mode is characteristic of brittle materials and is explained by UV induced polymer chain scission reactions resulting in weakening of the tensile modulus and strength of the fibre. Thus, the initial crack develops perpendicular to the fibre axis until complete failure of the filament.

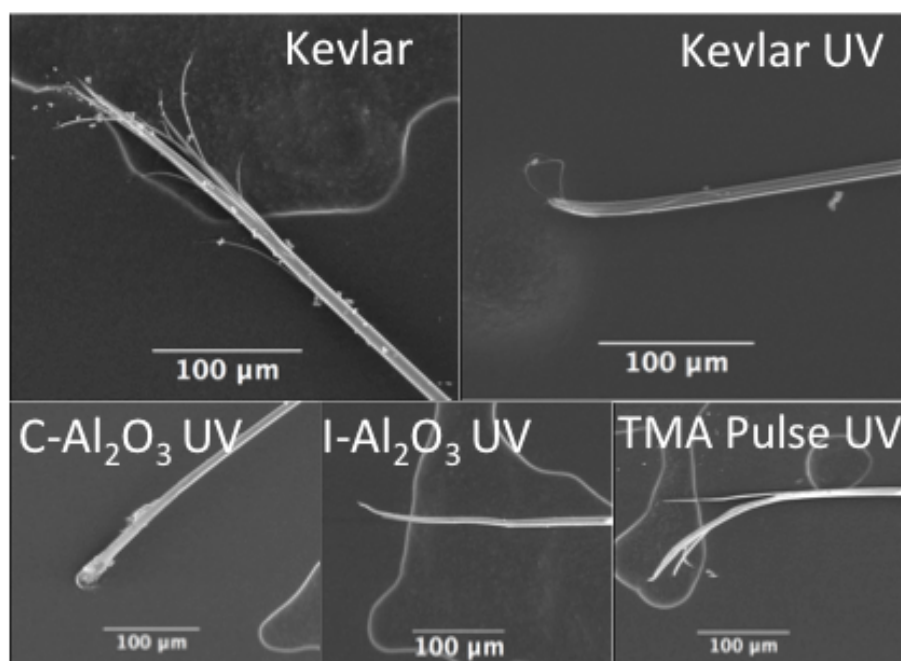


Figure 4.5: SEM images of the broken ends of native, coated and infiltrated Kevlar samples after irradiation with UV light in comparison to Kevlar before irradiation.

The same fracture mode was observed from the C- $\text{Al}_2\text{O}_3$  and I- $\text{Al}_2\text{O}_3$  Kevlar samples after UV exposure, indicating that the  $\text{Al}_2\text{O}_3$  coating does not prevent UV-

induced chain-scission reactions. In agreement with the analysis of the mechanical properties, the alumina infiltration obviously did not prevent the UV-induced degradation of Kevlar, thus the fibre showed the earlier mentioned brittle fracture mode. In contrast, the TMA pulse sample showed the fibrillar type of fracture characteristic as seen from native Kevlar after exposure to UV light. The longitudinal splitting and the fibrillation show that the combination of alumina coating and ZnO infiltration did not significantly embrittle the fibre.

Table 4.2: Change in the intensities of the amide-related peaks after UV irradiation

	Intensity variation after UV irradiation (%)			
	N-H st	Amide I	Amide II	Amide III
<b>Kevlar</b>	-7	2	2	-3
<b>C-Al<sub>2</sub>O<sub>3</sub></b>	-4	3	1	-3
<b>I-Al<sub>2</sub>O<sub>3</sub></b>	-5	0	-1	-4
<b>TMA pulse</b>	-1	0	1	0

To understand how the structure of different samples is affected by UV light, FTIR spectra of the samples were measured after UV irradiation. No significant changes were noted in the shifts of the peaks, but rather in the intensities. In Table 4.2 the intensities of the peaks of the irradiated samples were normalized and compared to those of the non-irradiated samples. Considering the measured mechanical properties, the UV light had the strongest impact on untreated Kevlar. The reduction of the intensity of the N-H stretching and Amide III bands, together with the increased intensity of the Amide I and II bands, indicate the cleavage of H-bonds between adjacent chains and a homolytic splitting of C-N and N-H bonds<sup>80,125,127</sup>. The degradation was to some extent suppressed upon coating or infiltration with Al<sub>2</sub>O<sub>3</sub>. The I-Al<sub>2</sub>O<sub>3</sub> samples were less sensitive to UV light than native Kevlar, which can be attributed to a parallel occurrence of chain scission and cross-linking of the polymer. However, the cross-linking did not completely compensate the effect of the chain-scission upon exposure to UV light. In the C-Al<sub>2</sub>O<sub>3</sub> samples, the polymer did not undergo serious alteration during the coating process and the metal oxide aims at absorbing the UV irradiation and protecting the

Kevlar fibres. However, a 25 nm thick alumina film deposited on top of the fibres is not sufficient to completely screen the UV radiation. Thus, the C-Al<sub>2</sub>O<sub>3</sub> and the I-Al<sub>2</sub>O<sub>3</sub> samples showed similar changes in the FTIR spectra after UV irradiation. The TMA pulse sample showed only negligible changes in the FTIR spectrum after UV irradiation, which was also reflected in the mechanical properties. On the one hand chain-scission reactions become less probable due to the high cross-linking level obtained by infiltrating ZnO, on the other hand the ZnO clusters buried inside the fibre will absorb UV light, thus preventing it from reaching the polymeric core.

#### 4.4. Conclusions

VPI or ALD can individually positively affect the mechanical properties of Kevlar. In this chapter we have shown the first approach to combine ALD and VPI into one hybrid process, which deposits Al<sub>2</sub>O<sub>3</sub> as thin film onto the polymer, while at the same time infiltrates ZnO into the polymer. In this way, a hybrid polymer-inorganic material with a binary inorganic fraction is created. The benefit of this approach is that the Al<sub>2</sub>O<sub>3</sub> thin film, deposited by ALD, enhances the modulus of toughness of the polymeric fibres, even exceeding the well-known extraordinary values of native Kevlar. Simultaneously, the sensitivity of the fibres to UV-light induced degradation is eliminated thanks to the hybridization of the polymer with ZnO. The hybrid coating-infiltration process is integrated and performed in a synchronous way and does not require any further specific adaptation of the ALD or VPI setup. Extension of this strategy to further precursor and substrate combinations gives rise to an optimistic view on exciting new developments in materials research and consequently applications with greatly performing new materials.

## Chapter 5

### Development and characterization of a Kevlar-ZnO hybrid conductive photocatalyst

#### 5.1.- Introduction

Flexible electronics define one key area of future technological devices. Here, functional polymers play an important role as the combination of low weight and mechanical flexibility makes polymers unavoidable within this technological concept. However, the electronic properties of polymers need to match the technological needs. Therefore, the past decades witnessed significant effort in synthesizing and optimizing organic conducting polymers (OCPs), such as doped  $\pi$ -conjugated polymers (polypyrrole, polyaniline, etc.). Current ideas for fabricating flexible electronic devices may be broken down into two major groups; printing devices on top of flexible polymer foils or functionalizing polymeric fibres. The second approach is lately gaining importance, as efficient and established industrial processes for producing large amounts of polymer fibres, as well as procedures for assembling those into textile, are available. This is a rather new research field and most of the approaches for functionalization of polymeric fibres relate to mechanical properties or blocking of UV light as explained in previous chapters. Integrating further physical properties into the fibres is of great desire but such approaches are still in their infancy with plenty of space for improvement.

An integration of electrical conductivity to top up the characteristic lightness, flexibility and good processability of Kevlar would make these fibres ideal candidates for fibre-based electronics. A variety of pathways for reaching this goal have been studied, including coating of Kevlar with metals<sup>93,134,135</sup>, metal oxides<sup>136</sup> or other polymers<sup>90,137-139</sup>. However, those approaches negatively impact the chemical and thermal stability or reduce the flexibility of the fibres. Strategies to maximize

both stability and electrical features of Kevlar fibres include coatings with metallic nanoparticles dispersed in a polymeric matrix<sup>88,89</sup> or with carbon nanotubes<sup>92</sup>. Such approaches appear promising in principle, but for enhanced durability the adhesion of the coating to the fibres requires optimization of the chemistry of the coating formulation, thus limiting the variation bandwidth and the potential applications. Furthermore, the amount of nanoparticles required to achieve good electrical conductivity is very high, which compromises the mechanical properties and seriously limits the up-scaling possibilities.

A fruitful strategy to induce conductivity in insulating polymer fibres may be based on vapour phase infiltration with a conducting material. As presented by Wang *et al.*<sup>70,71</sup>, VPI offers the possibility to dope conducting polymers in a solvent free post-processing route thanks to the infiltration of Lewis acids. However, it appears logical that this innovative doping route will only work on polymers with conjugated  $\pi$ -electron systems, similarly to traditional doping strategies. A variation of this doping strategy was also presented by the same group<sup>72</sup>, where unexpectedly high conductivity values were obtained through VPI of a metal oxide into a conducting polymer. They found that, apart from the intended polymer doping by the metal oxide, the nitrogen from the polymer acted as a dopant for the metal oxide. This discovery implies a radical change in the view of electrical functionalization of polymers as, contrary to previous strategies, it could be used to add conductivity also to insulating polymers.

Apart from flexible devices, polymeric fibres and textiles have been traditionally used as substrate for multicomponent catalytic systems<sup>140-142</sup> due to their characteristic flexibility and lightness. However, thanks to the development of OCPs and the study of their photocatalytic activity<sup>143</sup>, polymers are currently used in photocatalytic applications not as supporting material but also as the active photocatalyst. With the sunlight being the best natural light source, photocatalysts that operate with visible light are especially interesting. However, still most of the studied polymeric photocatalysts only work under UV radiation.

In the present work, we demonstrate the possibility to induce electrical conductivity into insulating Kevlar fibres by VPI of ZnO. The polymeric fibres infiltrated with ZnO show higher conductivity values compared to ZnO-coated

fibres and the values are stable even after bending the fibres. Besides, the conductivity can be tuned by controlling some processing parameters, such as the number of VPI cycles or the exposure time. The created ZnO-Kevlar hybrid material is not only electrically conducting but it also presents photocatalytic activity when exposed to visible light.

## 5.2.- Experimental

### 5.5.1.- Sample preparation

Individual fibres (for electrical characterization) and cut pieces of woven fabric (2 cm x 2 cm, for photocatalytic characterization) of Kevlar 29 were infiltrated with ZnO through VPI. The VPI processes were performed in a Savannah 100 (Cambridge Nanotech) ALD reactor. Diethyl zinc (DEZ, Strem chemicals) and purified water were used as zinc and oxygen sources, respectively. One cycle of the process consisted of: DEZ pulse for 0,08 s, followed by exposure of the substrate to the DEZ between 30 and 300 s, and purging with N<sub>2</sub> for 30 s, water pulse for 0,08 s, 30 s of each exposure and purging times. The cycle was repeated between 50 and 300 times. The precursors were kept at room temperature and the chamber temperature was 150 °C.

ALD coated samples were prepared as reference for the VPI-infiltrated samples. The preparation of the coated samples was done using the same parameters as in VPI, but omitting exposure times after precursor pulsing.

Individual fibres of Kevlar 29 were infiltrated with In<sub>2</sub>O<sub>3</sub> through VPI. The VPI processes were performed in a Savannah 100 (Cambridge Nanotech) ALD reactor. Trimethyl indium (TMI, Strem chemicals) and purified water were used as indium and oxygen sources, respectively. One cycle of the process consisted of: TMI pulse for 0,1 s, followed by exposure of the substrate to the TMI between 10 and 90 s, and purging with N<sub>2</sub> for 30 s, water pulse for 0,08 s, 30 s of each exposure and purging times. The cycle was repeated between 50 and 300 times. The precursors were kept at room temperature and the chamber temperature was 200 °C.

### 5.2.2.- Computational simulations

The computational calculations were carried out with the Perdew–Burke–Ernzerhof (PBE) exchange-correlation functional<sup>109</sup> and the SV(P) (double zeta valence basis set with polarization at all non-hydrogen atoms) basis set as implemented in TURBOMOLE<sup>110</sup> with the RI approximation for Coulomb integrals<sup>111</sup> accompanied by the corresponding auxiliary basis sets<sup>112</sup>. The “m4” integration grid of the module RIDFT was used<sup>113,114</sup>. Geometries were freely optimized using redundant internal coordinates<sup>115</sup> until gradients were  $< 10^{-6}$  Hartree. Optimized structures were visualised with Materials Studio suite version 7.0. This theoretical part of the work was performed by the group of Dr. Simon Elliott at the Tyndall national institute in Cork, Ireland.

### 5.2.3.- Spectroscopic analysis

The UV/Vis absorption spectra of the samples were recorded between 310-620 nm using a UV-Vis spectrophotometer (V-630 BIO, JASCO).

The nano-FTIR spectra were measured with a commercial nano-FTIR spectroscopy setup (Neaspec GmbH). The AFM was operated in dynamic mode, using a standard Au-coated tip (PPP\_NCST Au, Nanosensors), vertically vibrating at the cantilever resonance frequency ( $\Omega \approx 150$  kHz) with an amplitude around 60 nm. In order to isolate the signal due to the near-field interaction and suppress background contribution, the scattered signal was demodulated at the third harmonic of the tapping frequency,  $3\Omega$ . The mid IR broadband light was provided by a laser supercontinuum, which was tuned to emit a continuous spectrum between 1250 and 1800  $\text{cm}^{-1}$ , with an integrated output power of approximately 0.5 mW. The AFM tip was located in one of the arms of a Michelson interferometer, so that the demodulated signal  $I_3$  was recorded as a function of the reference mirror position  $d$ . The asymmetric spectrometer design allowed for both interferogram  $I_3(d)$  amplitude and phase recording.  $I_3(d)$  was then apodized using a three-term Blackman window and Fourier transformed, yielding to the complex spectrum  $E_3(\omega) = s_3(\omega)e^{i\phi_3(\omega)}$ . The nano-FTIR spectrum of each point was the average of 5 individual spectra, with a resolution of 8  $\text{cm}^{-1}$ . The total acquisition time was 8 minutes for each point. In order to normalize spectra, a clean gold surface spectrum  $E_{3,ref}(\omega) = s_{3,ref}(\omega)e^{i\phi_{3,ref}(\omega)}$  was recorded with the same resolution and acquisition time.

The referenced spectra, presented in the main text, are the result of the complex normalization  $a_3(\omega) = s_3(\omega)/s_{3,ref}(\omega)\sin(\phi_3 - \phi_{3,ref})$ . Ultramicrotome cuts for nano-FTIR analysis were done using a Leica UC6 ultramicrotome with a Diatome AFM diamond knife. The block face was prepared by taking final cuts at a thickness of 50 nm. The nano-FTIR measurements in this work were performed by Marta Autore from the Nanooptics group at CIC nanoGUNE.

#### 5.2.4- Electrical resistance measurements

Electrical resistance ( $R$ ) is a measure of an electrical current flow through a material. In general, the resistance of a material can be calculated based on Ohm's law:  $V = I.R$ ; where  $V$  is the voltage,  $I$  is the current and  $R$  the resistance. For measuring, a simple two-point resistance measurement can be performed, which consists of applying a current between the two electrodes and measuring the potential difference between them. This method acquires the total resistance of the circuit, including the contact resistance between sample and electrode, and therefore is used to characterize semiconductors or materials with a high resistance. In such cases, the contact resistance is negligible compared to the material's resistance and the measured value mainly reflects the resistance of the material.

The electrical resistance measurements in this thesis were done using the two-point method and in a voltage range between -2 V and 2 V with a KEITHLEY Semiconductor Characterization System 4200-SCS at room temperature and atmospheric pressure. For the measurements, ten individual fibres of each sample were fixed to a Kapton tape. As contacts, stripes of silver paint were applied perpendicular to the fibres with a distance of 2 mm between the stripes. With several equidistant stripes, different sections of the fibres could be measured and values of the different sections of the fibres and the 10 used identical fibres could be averaged. For the characterization of the photocurrent the samples were kept in dark environment overnight. Then, the samples were illuminated with a 150 W halogen lamp, a voltage of 10 V was applied, and the generated current measured.

#### 5.2.5.- Photocatalytic activity study

A catalyst is a substance that increases the rate of a chemical reaction by changing the reaction mechanism, but still leading to the same reaction product. In

presence of a catalyst the energy to reach the transition state of a reaction is reduced, allowing a more rapid chemical conversion. Typically, the catalyst reacts with the substrate forming a temporary intermediate product, which then reacts further and regenerates the initial catalyst in a repeated manner. Therefore, only little amount of a catalyst is needed, as it is not consumed during the reaction.

Catalysts are usually classified based on their phase: a homogeneous catalyst is in the same phase as the reactant, also called substrate, (usually gas or liquid phase) while a heterogeneous catalyst is in a different phase than the substrate (usually gaseous or liquid reactant adsorbed on a solid catalyst).

Generally, for the catalytic reaction to occur simply the presence of the catalyst is needed. However in some cases, the catalyst needs to be excited to create the intermediate product with the substrate. In these cases, an external stimulus is needed to trigger the catalytic reaction. Among others, this external stimulus can be electrical current (electrocatalysis) or light (photocatalysis).

Various methods can be used to measure the activity of a catalyst. The most common methods involve measuring the temporal change of the concentration of the substrate or the product during the catalytic reaction. If either the substrate or the product absorbs light in the UV-Vis region, this change in the concentration can be followed photometrically, that is, by UV-Vis spectroscopy. According to the Beer-Lambert law, the light a substance absorbs in a specific wavelength is proportional to the concentration of this substance ( $A = \epsilon \cdot l \cdot c$ ,  $A$  being the absorbance,  $\epsilon$  the molar absorptivity that depends on the wavelength,  $l$  the length of the light path and  $c$  the molar concentration of the absorbent). Thus, the UV-Vis absorption of a sample can be used to monitor the concentration of the absorber at different times of the progressing photocatalytic reaction.

The study of the photocatalytic activity in this thesis has been carried out under illumination with visible light. The light was generated with a xenon lamp and an optical filter cutting off wavelengths below 420 nm. For the experiments the degradation of a Rhodamine B (RhB) (Sigma, 95%) solution was followed and as spectrometer a NanoDrop 2000c from Thermo Scientific was used. The samples, cut pieces of woven Kevlar fabric (2 cm x 2 cm), were immersed into 30 mL of a Rhodamine B solution in water (10mg/L) and the solution was stirred in dark for 30

minutes before illumination to ensure an adsorption/desorption equilibrium of RhB to/from the sample. At regular time intervals, 750  $\mu\text{L}$  of the solution were removed and the absorption of Rhodamine B at 554 nm was measured. The decrease of the absorption values at this particular value was recorded over 120 minutes.

### 5.3.- Results and discussion

#### 5.3.1.- Band gap engineering through VPI

In order to judge the viability of the VPI hybridization to induce electrical conductivity into Kevlar fibres through infiltration of ZnO, we performed quantum chemical modelling based on DFT calculations for a better understanding of the electronic structure of the polymer. The model system consisted of 8 molecular units as depicted in Figure 5.1. Knowing that Kevlar is an electrical insulator, a band gap higher than 4 eV was expected. Thus, the HOMO/LUMO gap of 1.59 eV obtained in the theoretical model was astonishingly low. Two reasons might explain the difference between measured and predicted band gap; on the one hand, the band gap values calculated by DFT are commonly lower than the experimentally obtained values<sup>144,145</sup> and on the other hand, being a model limited to 8 rings only, the high order of the polymer chains and the interchain interactions present in the macroscopic fibres are not considered, which might act as barriers for electronic conduction.

As shown in Chapter 3 of this thesis, the chemical interactions and the structure of the resulting Kevlar-ZnO hybrid material were modelled. Figure 5.1 shows the structure of the hybrid obtained from the quantum chemical simulations, consisting of Kevlar chains covalently cross-linked through its amide groups and ZnOH. Besides, the benzenoid rings transform into quinoid rings and the bond length of C-O is 1.27 Å when bound to Zn, which is longer than the normal C=O bond length of 1.24 Å in Kevlar. The bond length of C-N in neighbourhood of the linked Zn changes only slightly from 1.41 Å to 1.40 Å, which indicates a weak double bond character. This change from N-H to N-Zn bonding is balanced by a redistribution of charge in the conjugated  $\pi$  systems of the Kevlar chains. The structure implies transfer of two electrons from each N-H to a  $\pi$  orbital of the imine-quinoid unit, making this the new HOMO, and transfer of two electrons from each

enolate-quinoid  $\pi$  orbital to O-Zn, which becomes the new LUMO. This is confirmed by the population analysis, which shows the positive charge of [ZnOH] being balanced by an increased negative charge on O and N. The calculated HOMO/LUMO gap after infiltration decreases to 1.17 eV. As for the case of the initial Kevlar model, the energy gap value is very likely to be underestimated in the hybrid material model. However, the calculated lowering of the position of the conduction band, resulting in the reduction of the band gap, is reliable.

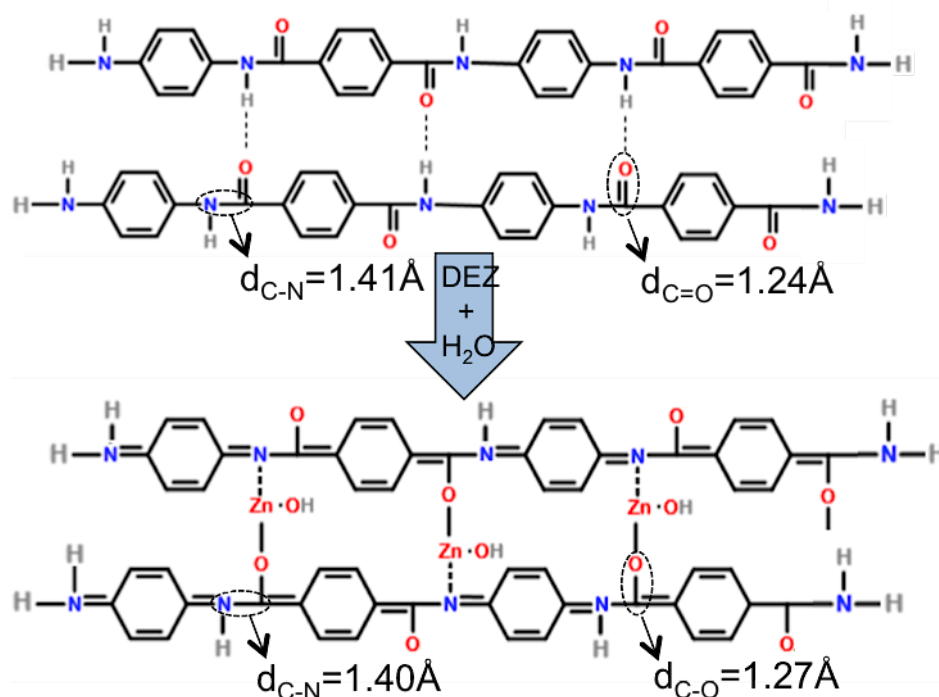


Figure 5.1: 8 molecular units system before and after ZnO infiltration as modelled by DFT.

The quantum chemical simulations indicated that VPI might be used to induce electrical conductivity into Kevlar fibres through the infiltration of ZnO. In order to verify this, we analysed the structure of the material resulting from the infiltration of Kevlar with ZnO and compared it to the theoretical model. The cross-linking of the Kevlar chains through O-Zn-N bonds observed in the modelled system is analysed and described in Chapter 3 of this thesis. However, the conversion of benzenoid rings into quinoid rings and the resulting reduction in the energy band gap required experimental verification. We compared Kevlar samples coated with ZnO by ALD (C-ZnO) and Kevlar samples infiltrated with ZnO by VPI (I-ZnO). Both samples were prepared under identical conditions (150 °C and 200

cycles) and with the same precursors (DEZ and water). An exposure step of 30 seconds for both precursors was used in the infiltration process while no exposure was used in the coating process.

From the UV-Vis absorption spectra of the untreated Kevlar, C-ZnO and I-ZnO, displayed in Figure 5.2, we observe that the coating with ZnO does not alter the polymer characteristics much. The spectrum of C-ZnO shows only a sharp absorption peak at 3.4 eV, which corresponds to the band gap of ZnO, and the absorption above 2.8 eV is slightly enhanced. The absorption spectrum of I-ZnO, however, shows some significant differences. A pronounced absorption peak develops at 3 eV and results in an enhanced absorption down to 2.2 eV in comparison to both untreated and coated Kevlar. Both, the new peak as well as the absorption in the lower energetic region, indicate a correlation between the calculated and fabricated materials, that is, the conduction band of Kevlar is lowered after infiltration with ZnO.

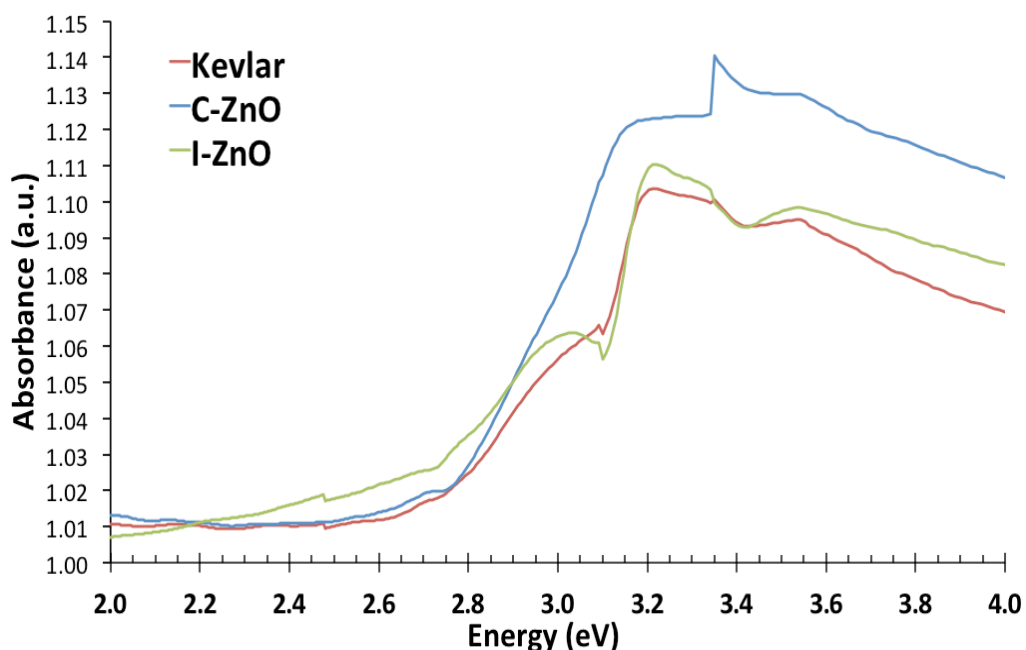


Figure 5.2: Experimental UV-Vis spectra of unmodified Kevlar (Kevlar, red line), ZnO coated Kevlar (C-ZnO, blue line) and ZnO infiltrated Kevlar (I-ZnO, red line).

Given the very shallow depth of infiltration and the majority of the Kevlar being unaffected after infiltration, identifying the quinoid structures in the I-ZnO

sample is not straightforward. Infrared spectroscopy is an ideal technique for distinguishing such molecular changes after infiltration, but in a routine FTIR measurement, the signal of the unmodified Kevlar will dominate, thus the methodology is not suitable in this case. Therefore, nano-FTIR was applied on microtomed slices of the Kevlar fibres in a scanning mode, which is capable of recording infrared spectra locally with a resolution of 10 nm. With this approach, we localized molecular changes near the surface area of the ZnO-infiltrated Kevlar. Figure 5.3 shows spectra of the I-ZnO sample in the near-surface area (infiltrated area) and in the bulk of the fibre (Kevlar).

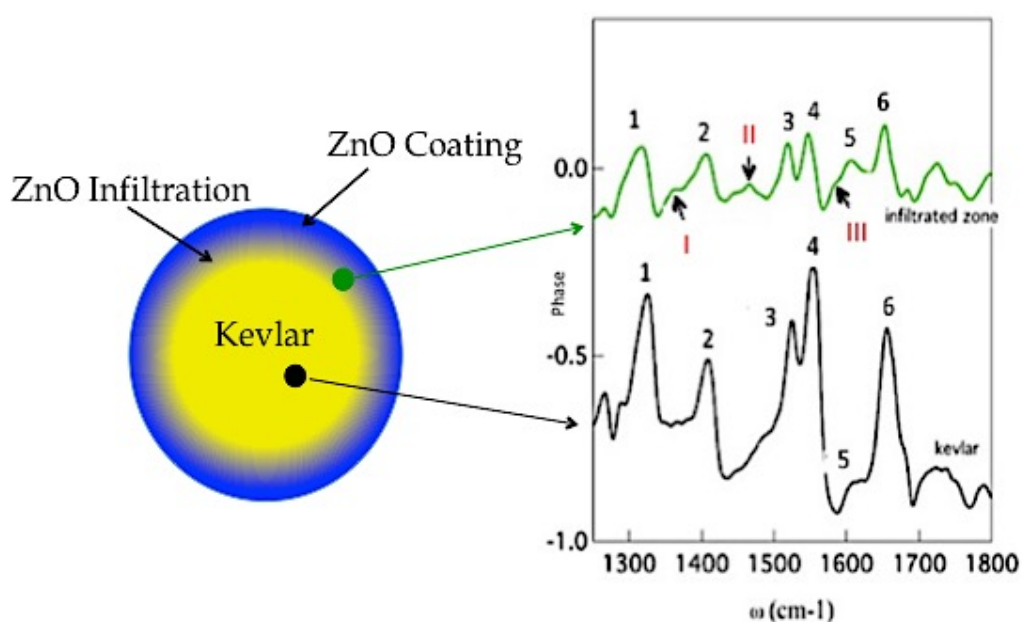


Figure 5.3: Scheme of the cross-sectioned area of an I-ZnO Kevlar fibre (left) showing the measurement points of the nano-FTIR spectra (right). The peaks are marked with numbers and correspond to the vibration modes shown in Table 5.1.

The spectra from the bulk of the I-ZnO fibre match very well the far field spectra of Kevlar and the vibration peaks calculated from the model by DFT, which are all summarized in Table 5.1. However, the spectra recorded in the infiltrated area show three new signatures appearing at 1361, 1465 and 1590  $\text{cm}^{-1}$  (indicated with I, II and III). These peaks match the vibrational modes of quinoid rings as calculated from the model system after ZnO infiltration (Table 5.1). Thus, the conversion of the benzenoid rings into quinoid rings is very likely identified by

nano-FTIR. Besides, the peaks related to the vibrations of the benzenoid rings are still observed in the nano-FTIR spectrum of the infiltrated area, meaning that both benzenoid and quinoid rings are simultaneously present in the Kevlar-ZnO hybrid.

Table 5.1: Molecular vibration peaks calculated by DFT from the modelled molecule before (1-6) and after (I-III) ZnO infiltration.

Peak	Vibration mode	Calculated wavenumber (cm <sup>-1</sup> )	nanoFTIR wavenumber (cm <sup>-1</sup> )
1	Benzenoid ring rocking	1252	1316
2	-C-C-N stretching	1355	1406
3	1,4-C <sub>6</sub> H <sub>4</sub> stretching	1520	1519
4	-N-H rocking	1542	1546
5	1,4-C <sub>6</sub> H <sub>4</sub> stretching	1650	1606
6	-C=O stretching	1687	1652
I	=N-C stretching	1342	1361
II	Quinoid ring breathing	1502	1465
III	Quinoid ring breathing	1588	1590

Once the lowering of the band gap and the appearance of the quinoid rings were experimentally proven, we measured the electrical conductivity of the fibres and its consistency upon deformation of the fibres. For that, the electrical resistance of untreated, C-ZnO and I-ZnO samples was measured before and after manually bending them. The manual bending consisted of fully folding the fibres to 180° and unfolding back to the initial position for three consecutive times. As explained in the previous chapters, a thin film of the infiltrated material is unavoidably deposited on top of the fibres during the VPI process. Therefore, the measured resistance of infiltrated fibres will include contribution of both the coating and the infiltration. Upon manually bending the fibres the brittle coating is expected to break and only the contribution of the infiltration to the resistance is measured.

Figure 5.4 shows the measured resistances for the three tested types of fibres. The resistance of the untreated Kevlar fibres was above the detection range of the equipment ( $\approx 10^{15} \Omega$ ) before and after bending them. In the case of C-ZnO, thanks to the ZnO film on top of the fibres, the resistance decreased to  $4 \times 10^{13} \Omega$ . However, after manually bending the fibres, the thin and brittle ceramic coating cracked. Thus, the conduction pathway through the semiconducting ZnO shell was interrupted and the resistance increased again exceeding the detection range. The experiments confirmed that no parasitic infiltration of ZnO occurred during coating, since the bent C-ZnO fibres showed similar electrical behaviour as untreated Kevlar. From those experiments we can conclude that coating Kevlar fibres with ZnO results in a reduction of the electrical resistance, but only as long as the fibres are not bent.

However, the resistance measurements of the I-ZnO fibres showed very different behaviour. Initially, the infiltrated fibres showed with  $2.87 \times 10^9 \Omega$  a significantly lower resistance than the coated fibres. As both C-ZnO and I-ZnO were processed for 200 cycles, the contribution of the ZnO coating to the resistance can be assumed as being similar for both samples. Therefore, the drop in resistance observed from the I-ZnO fibres, indicates that a new conduction path has been created upon VPI processing. After bending the fibres, the contribution of the coating was diminished and the remaining resistance was with  $6.20 \times 10^{11} \Omega$  still four orders of magnitude lower than that of untreated Kevlar. The resistance increase after bending I-ZnO was similar to the increase observed from the C-ZnO sample, further confirming that after bending the fibre the electrons cannot flow through the ZnO coating and its contribution to the resistance is neglectable. The remaining lower resistance value indicates that the electrons can flow through the new conduction path created by the infiltration of ZnO, even after bending the fibres.

The fabricated material system is very complex, which makes it very difficult to find detailed explanations on the nature of the new conduction path. In principle, we could consider three different materials being involved, namely the infiltrated ZnO, the altered Kevlar and the very interface between ZnO and Kevlar, potentially being nitrogen-doped ZnO. The infiltrated ZnO may contribute to the conductivity but cannot be the sole reason. The depth of infiltration of ZnO is on the same order of magnitude as the coating, but with significantly lower density, thus we could

expect a maximum contribution of the same order of magnitude as the coating. Thus, the notable reduction of the resistance observed after infiltration confirmed that the infiltrated ZnO is not the only material contributing to the conductivity. As discussed earlier, the DFT calculations indicate that upon interaction of DEZ with the molecular backbone of Kevlar benzenoid units may convert to quinoid units with the resulting molecule showing an increased negative charge on O and N and thus reduction of the energy band gap. These changes may induce an electronic conductivity in the polymer itself, thus the modified Kevlar could be part of the new conduction path. Finally, based on the synergetic mutual doping observed by Wang *et al.* in the ZnO infiltration of PANI, it could be assumed that the interaction of the infiltrated ZnO with the amide group of Kevlar results in a nitrogen doping of the infiltrated ZnO. However, those materials are not spatially separated, but intermixed, making it very difficult to identify individual contributions to the conductivity.

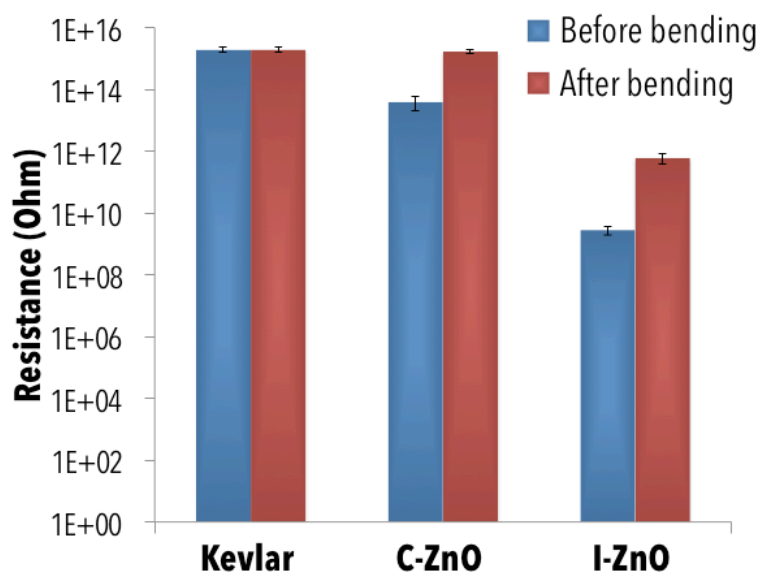


Figure 5.4: Comparison of electrical resistance of untreated, C-ZnO and I-ZnO Kevlar fibres before and after manually bending them.

### 5.3.2.- Tuning the resistance of the Kevlar-ZnO hybrid

As the contribution of the infiltration to the resistance was obvious, we analysed how the processing parameters affect the resistance of the I-ZnO Kevlar.

The infiltration process yields an amount of ZnO being incorporated into the substrate with each cycle. Accordingly, the infiltrated volume fraction of the oxide will depend on the number of cycles applied. We varied the number of infiltration cycles in order to optimize the electronic properties of the infiltrated Kevlar fibres and indeed identified a relation between the number of infiltration cycles and the resistance. Figure 5.5a shows the resistance of the fibres vs. the number of infiltration cycles before and after bending. While up to 100 infiltration cycles did not show any significant change in the electrical resistance of the Kevlar fibres, an increase to 200 and further to 300 cycles resulted in its dramatic decrease. Apparently, a ZnO infiltration threshold has to be overcome to achieve a significant decrease in the electrical resistance. Besides, the resistance rise after bending the 300 cycles sample is smaller than the rise in the 200 cycles sample, indicating an effective incorporation of a larger amount of infiltrated ZnO.

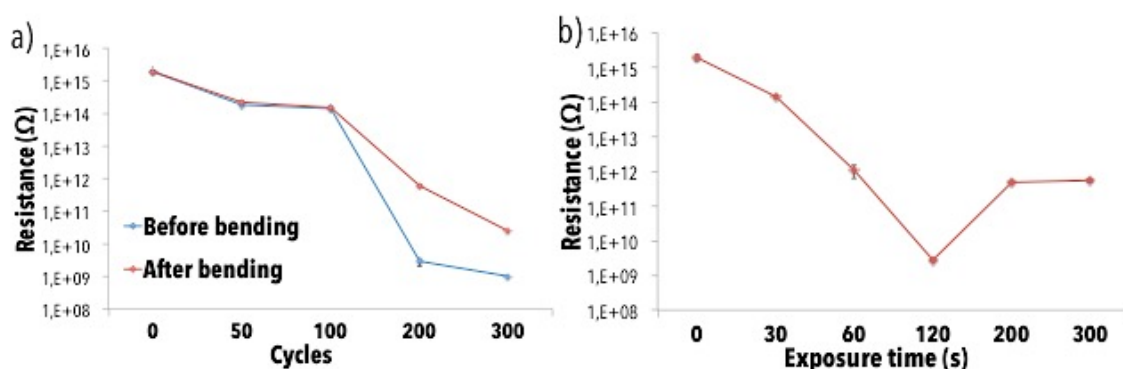


Figure 5.5: a) Effect of the number of VPI cycles on the resistance of I-ZnO Kevlar (exposure time maintained at 60 s) b) Effect of the exposure time on the resistance of I-ZnO Kevlar (200 cycles, after bending).

A further processing factor that may alter the electrical properties upon infiltration is the exposure time of the substrate to the precursors. In principle, higher exposure times allow for deeper infiltration of the precursors and, consequently, a thicker subsurface area of Kevlar becoming modified. Figure 5.5b shows the dependence of the resistance of I-ZnO Kevlar on different exposure times. As expected, increasing the exposure time up to 120 seconds reduces the resistance due to the presence of a thicker modified area in which electrons can flow. However,

with longer exposure times (200 and 300 seconds) the resistance increases again. Two possible reasons may explain the observed increase. On the one hand, the infiltrated material always presents a decreasing concentration gradient from the surface to the bulk of the substrate. Thus, the longer the exposure time, the deeper will the infiltration occur, but the less dense will the material be. After 200 and 300 seconds of exposure the density of the infiltrated ZnO might be too low to enable a flow of electrons. On the other hand, after long exposures times, the purging time is also increased to ensure the complete evacuation of the unreacted precursors. This could result in a lower than expected amount of infiltrated material.

Therefore, both the amount of infiltrated ZnO and the density of the material are of importance for the electrical properties. The amount is defined by the number of cycles and thus the material supplied in total, while the density will be altered with the exposure time and thus the diffusion depth of the precursors into the polymeric substrate.

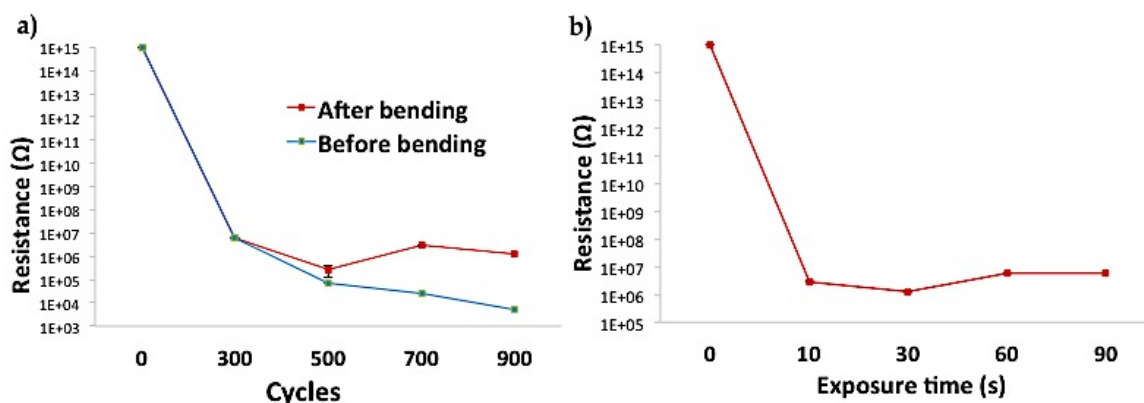


Figure 5.6: a) Effect of the number of VPI cycles on the resistance of In<sub>2</sub>O<sub>3</sub>-infiltrated Kevlar (exposure time was maintained at 30 s) b) Effect of the exposure time on the resistance of In<sub>2</sub>O<sub>3</sub>-infiltrated Kevlar (700 cycles, after bending).

Another possibility to tune the resistance of the samples is to select a different material for infiltration. In order to evaluate this pathway, instead of the semiconducting ZnO, conducting indium oxide (In<sub>2</sub>O<sub>3</sub>) was infiltrated. As expected from the conducting nature of the infiltrated oxide, a significant reduction of the resistance of the Kevlar fibres was observed already after 300 cycles of In<sub>2</sub>O<sub>3</sub>

infiltration. As shown in Figure 5.6a, also the resistance of the indium oxide infiltrated Kevlar fibres depended on the number of infiltration cycles. The resistance decreased almost linearly when increasing the number of infiltration cycles, reaching  $5.10^3$  Ohms after 900 cycles at its best. After bending the fibres, the contribution of the  $\text{In}_2\text{O}_3$  coating was eliminated and only the contribution of the  $\text{In}_2\text{O}_3$  infiltration was measured. Surprisingly, the samples after 300 and 500 infiltration cycles showed very similar resistances before and after bending. The stability of the electrical resistance to mechanical stress of these samples may arise from the amorphous nature of the coating. As shown in the XRD patterns in Figure 5.7, the sample after 500 infiltration cycles only showed peaks corresponding to the crystalline planes of Kevlar. However, from the 700 infiltration cycles sample new peaks were observed, which correspond to indium oxide crystal planes. With a low number of infiltration cycles (300 and 500 cycles), the  $\text{In}_2\text{O}_3$  film grown on top of the samples was obviously still very thin and amorphous, and therefore flexible enough to sustain mechanical bending without cracking. Thus, the electrons could flow through the coating. At higher numbers of infiltration cycles (700 and 900 cycles), the coating on top of the fibres was thicker and crystallites grew, resulting in enhanced brittleness. Manual bending caused the crystalline coating to crack, with the consequence of an increased resistance.

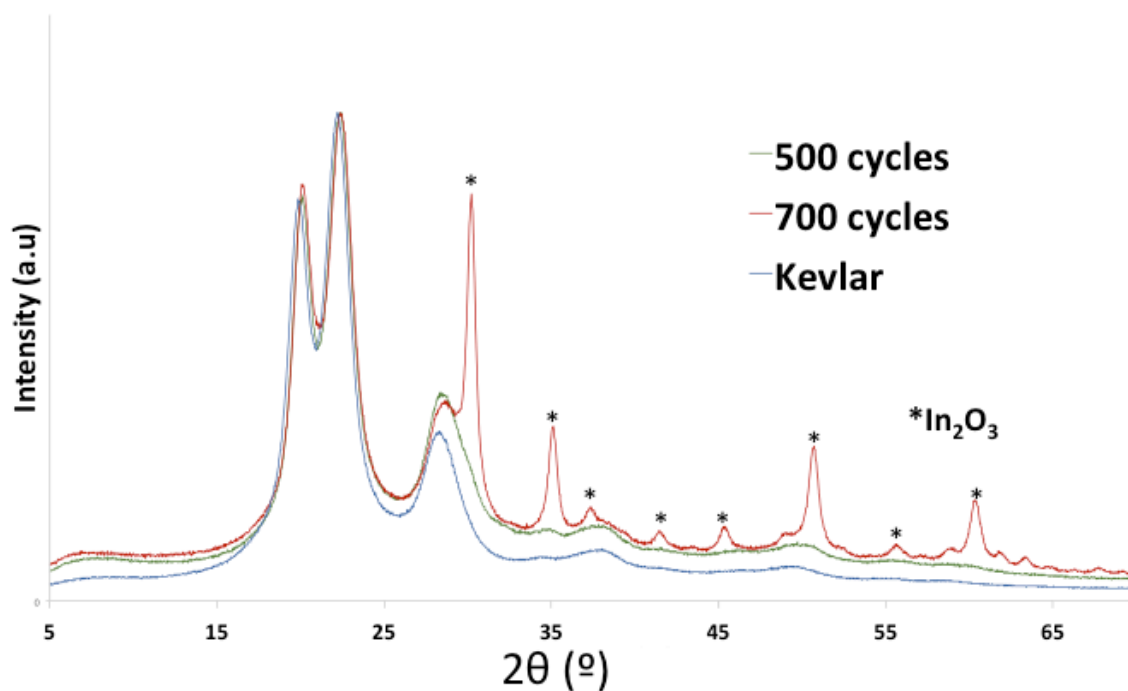


Figure 5.7: XRD patterns of the  $\text{In}_2\text{O}_3$ -infiltrated samples after different numbers of infiltration cycles.

Contrary to the case of the ZnO infiltration, changing the exposure time did almost not affect the resistance of the indium oxide infiltrated samples. The fibres prepared with exposure times varying from 10 to 90 seconds showed almost identical resistance after bending. As shown in Figure 5.8, the infiltration depth of the  $\text{In}_2\text{O}_3$  hardly changed with the exposure time. After increasing the exposure time by the factor of 9, that is from 10 s to 90 s, the infiltration depth increased by only 4 nm. Thus, as the amount of infiltrated indium oxide did not significantly vary, the resistance of the hybrid Kevlar- $\text{In}_2\text{O}_3$  was maintained constant.

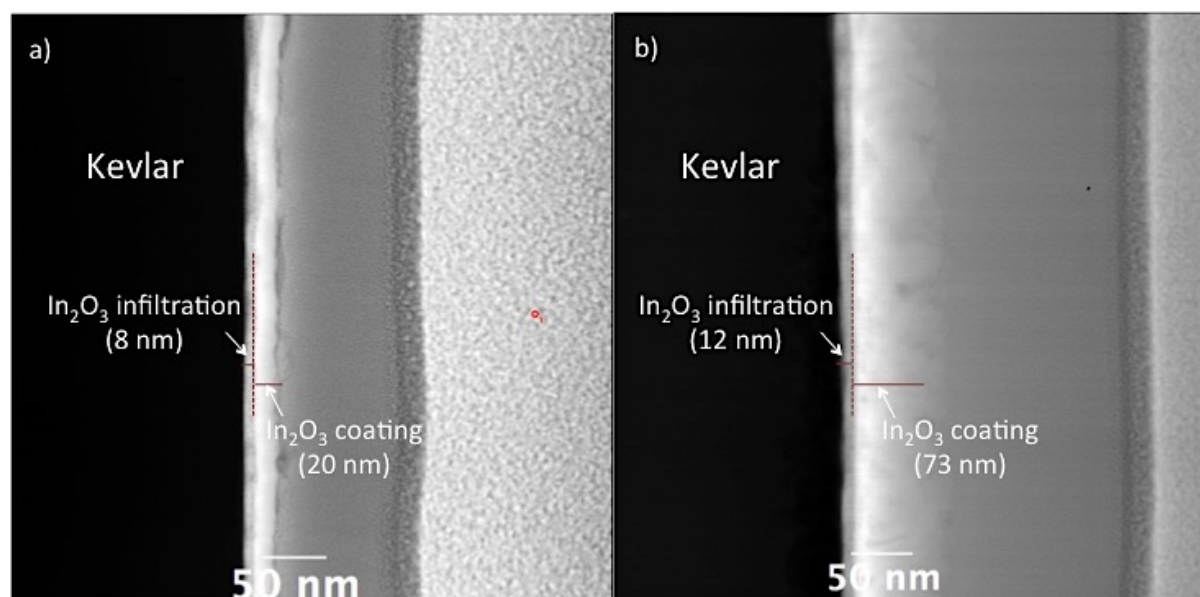


Figure 5.8: TEM images of the cross-sectioned area of the 700 cycles I-In<sub>2</sub>O<sub>3</sub> Kevlar fibres after following exposure times: a) 10 s and b) 90 s.

### 5.3.3.- Photoconductivity

When a semiconductor absorbs light with energy higher than the band gap energy, an increase in its conductivity occurs. The reason of the conductivity change is the creation of electron-hole pairs induced by absorption of light.

The photo response of ZnO has been widely studied because of its characteristic slow decay<sup>146,147</sup>. In general, a decay of the conductivity after cutting off the light is expected to be very rapid, due to the solid-state electron-hole recombination process. However, in the case of n-type metal oxides, such as ZnO or TiO<sub>2</sub>, the conduction decay occurs slowly, which is determined by surface effects (molecular adsorption and desorption processes). Due to the wide band gap of ZnO (3.37 eV), ultra violet light is needed to overcome this gap and induce conductivity. In the case of I-ZnO Kevlar fibres, the reduction of the band gap and change in the absorption spectra implies that the fibres may also interact with visible light, since the absorption of light after infiltration rose.

In order to analyse the effect of visible light on the electrical properties of the fibres, we measured the resistance of the samples after bending, while being illuminated with a visible light source. From Figure 5.9a one can see that there were no changes in the resistance of the untreated and C-ZnO Kevlar fibres upon

illumination. Thus, visible light is not energetic enough to excite neither the untreated nor the C-ZnO fibres.

However, the resistance of infiltrated fibres was further lowered by 3 orders of magnitude to  $6.23 \times 10^8 \Omega$  after illumination. Such a significant change in the electrical resistance indicates that the electronic configuration of I-ZnO fibres is very different to that of untreated Kevlar. As predicted by DFT modelling and further confirmed by the UV-Vis spectroscopy, with the infiltration of ZnO the band gap of Kevlar shifted to a regime where visible light is sufficiently energetic to create free charge carriers in the material. Considering the contribution of the ZnO coating being diminished after bending the fibres, one of the already mentioned three materials created during the infiltration of ZnO has to be responsible for the photocurrent generation under visible light. Among these materials, the infiltrated ZnO cannot be excited by visible light, as there is no reason to assume that its properties differ that seriously from bulk ZnO. Therefore, the material that was excited by visible light may be either the modified Kevlar or the interfacial nitrogen-doped ZnO. Similar to the case of characterization of the electrical resistance, it is difficult to identify the contribution of the individual components, as both materials are mixed.

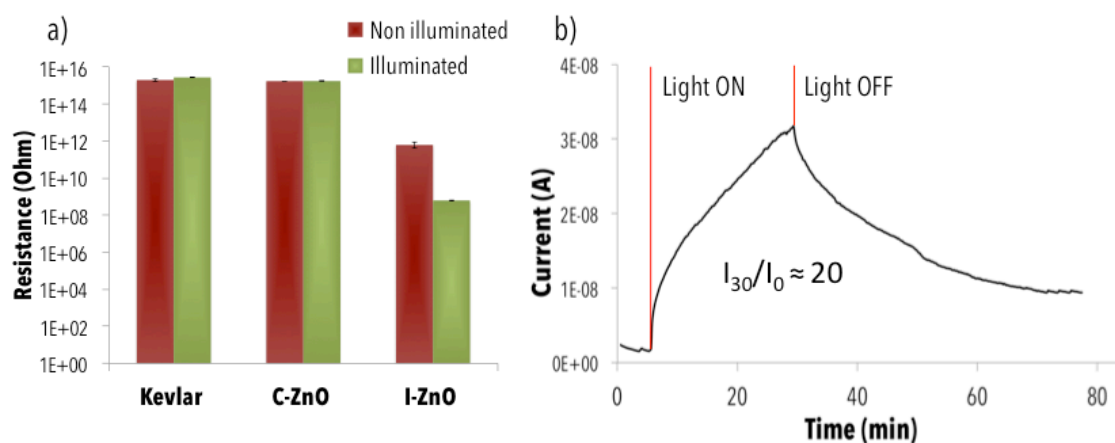


Figure 5.9: a) Comparison of electrical resistance of untreated, C-ZnO and I-ZnO Kevlar fibres in the dark and when illuminated with visible light. All samples were measured after bending. b) Photocurrent measurement of I-ZnO Kevlar fibres under visible light applying a bias voltage of 10V.

Figure 5.9b shows the time dependence of the current generated by I-ZnO Kevlar under visible light illumination. The photocurrent generated after 30 minutes of visible light illumination was around 20 times higher than the dark current with the same sample. This value is comparable to the photocurrent values obtained from ZnO nanoparticle films, however, illuminated with UV light at 278 nm wavelength<sup>148</sup>. The characteristic slow decay of ZnO was observed ( $\tau$  decay = 38 minutes) in the I-ZnO fibres and the current did not restore the initial values. This is an indication of free carriers being trapped by the molecular adsorption and desorption processes mentioned previously. For the embedded ZnO, those molecules may be the polymeric fractions of Kevlar surrounding the infiltrated ZnO, together with potentially in-diffusing small molecules, such as O<sub>2</sub> or similar.

#### 5.3.4.- Photocatalytic activity

The photocatalytic activity of semiconducting oxides is very interesting from the applications perspective and important for numerous approaches in environmental protection<sup>149,150</sup>. As a consequence of its high photosensitivity, nontoxic nature and the intrinsic wide band gap, ZnO is considered being excellent for such applications. Even though highly efficient ZnO-based photocatalysts have been reported, most of them only work upon illumination with UV light<sup>151,152</sup>. However, visible light responsive photocatalysts are highly desired as they can be more efficient by harvesting energy from a wider spectrum of the solar light.

As seen from the UV-Vis spectrum and the photoconductivity measurements, the I-ZnO Kevlar absorbs light in the visible region. In order to verify whether or not the I-ZnO samples could be used as photocatalysts operating with visible light, we studied the degradation of Rhodamine B under those conditions. Figure 5.10 shows the evolution of the Rhodamine B concentration over time upon illumination and in contact with the various catalysts.

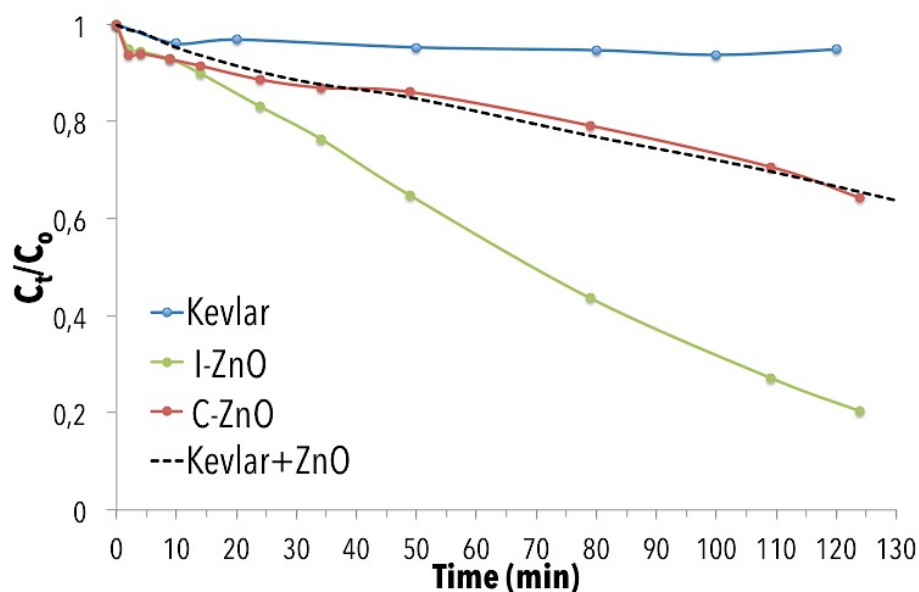


Figure 5.10: Degradation of Rhodamine B over time upon illumination with visible light and in contact with the various synthesized samples.

Untreated Kevlar did not show any catalytic activity under visible light illumination. For comparison, the photocatalytic activity of untreated Kevlar in presence of commercial ZnO powder was measured (dashed black line in Figure 5.10). In this case, some photocatalytic degradation of Rhodamine B occurred, and the concentration of the dye was reduced by around 30%. The C-ZnO Kevlar fibres showed similar results, confirming that the electronic structure of Kevlar and ZnO are similar to the previous case. The reason for the observed slight catalytic activity may be that due to the imperfection of the optical cut-off filter a small amount of UV light could reach the sample, which will be absorbed by the ZnO, thereby inducing a photocatalytic process. In contrast to those samples, a degradation of 80% of the Rhodamine B was obtained with I-ZnO. This huge difference in the photocatalytic activity of this sample confirmed not only that the band gap is shifted to the visible light region, but also that I-ZnO fibres are active as photocatalysts under those conditions.

We analysed the effect of the amount of infiltrated ZnO in the I-ZnO fibres on the degradation efficiency (Figure 5.11a). Similar to the case of electrical resistance measurements, we observed that there is a minimum amount of ZnO that needs to be infiltrated in order to obtain a significant increase in the catalytic activity.

Therefore, the I-ZnO fibres processed for 50 and 100 cycles showed a rather weak photocatalytic activity. The strongest catalytic activity was observed from the 200 cycles sample. The stability and durability of the I-ZnO Kevlar as photocatalyst was tested by measuring the catalytic activity of the 200 cycles sample 5 consecutive times. As shown in Figure 5.11b, no decrease in the catalytic activity was observed until the third test and the activity was reduced by 50% after 5 tests. This rapid loss of activity may be due to the dissolution of the infiltrated ZnO by the acidic (pH  $\approx$  4,5) Rhodamine B solution. If the infiltrated ZnO dissolves, the bonds and interactions between the ZnO and Kevlar chains disappear. As the photocatalytic activity using visible light arises from the band gap shift triggered by these interactions, dissolution of ZnO assumes a loss of the catalytic activity.

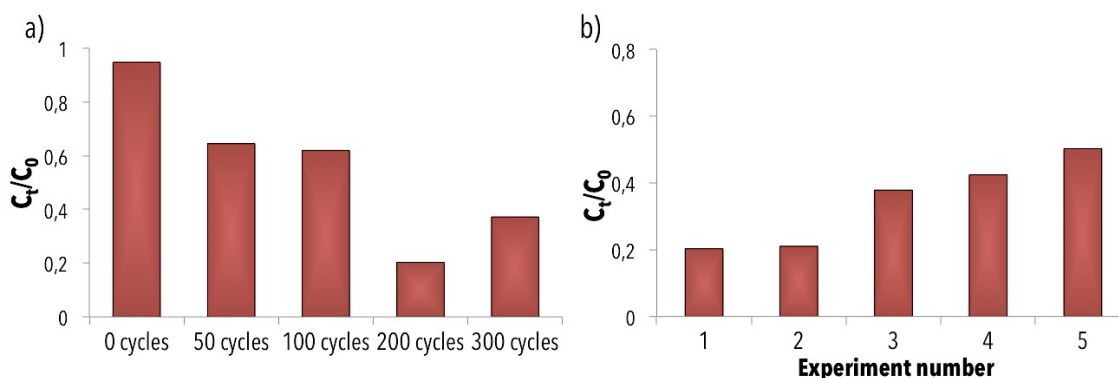


Figure 5.11: The photocatalytic activity of I-ZnO as a function of a) the number of infiltration cycles and b) the number of consecutive experiments (200 cycles sample).

## 5.4.- Conclusions

To summarize, we have demonstrated that VPI can successfully be used to alter the electronic properties of some insulating technical polymers. Using Kevlar as example, which besides simple coating approaches has by now proven to be largely resistant to functionalization, we showed that the polymer can be made conductive and that the conductivity is a result of the attack of the precursor on the polymer backbone. This modification changed the electronic situation by shifting charge density towards the polymer chain. The DFT-calculated model system confirmed such changes, which were experimentally identified by localizing quinoid structures

through nano-FTIR. The conductivity was strongly relying on the interface between the polymer and the inorganic phase, which can be derived from the comparison of coated and infiltrated fibres. Not only the infiltration results in higher conductivity, but also photocatalytic activity under visible light was demonstrated. The shift of the band gap towards lower energies made it possible to use the polymer-metal oxide hybrid as a photocatalyst for the degradation of Rhodamine B. Further optimization of both the process and the involved materials will be performed in order to reach levels of conductivity and photoactivity that are better suitable for integration of electronics into Kevlar-based textiles or materials, but plenty applications may already be approached with the current material system.



## Chapter 6

### Summary and outlook

This thesis presents different approaches for the functionalization of Kevlar fibres, which are based on vapour phase infiltration. The three main parts (chapters 3, 4 and 5) show how the infiltration and hybridization of Kevlar with a metal oxide leads to the introduction of new functionalities and improvement of the stability and mechanical properties of this polymer.

In the first part, Kevlar fibres were infiltrated with ZnO through VPI and the structure of the created ZnO-Kevlar material was theoretically and experimentally studied. It was shown that this hybrid material consisted of ZnO clusters grown among covalently cross-linked Kevlar chains. The effect of the hybridization on the thermal and UV stability of the fibres was studied showing an increase of almost 10 °C in the decomposition temperature and the complete suppression of the UV induced degradation, while maintaining 90% of the modulus of toughness. The results were compared with the ZnO-coated Kevlar fibres' results, showing that not the ZnO coating (which is present in both the coated and the infiltrated samples), but the infiltration and hybridization of Kevlar with ZnO were responsible for the observed improvement. Besides, the negative impact of the ZnO coating on the UV stability of the fibres was also demonstrated.

A novel combined ALD/VPI process was presented in the second part. Thanks to this combined process, it is possible to coat a polymeric substrate with a metal oxide, while infiltrating with another metal oxide. Using this ALD/VPI process Al<sub>2</sub>O<sub>3</sub> coated and ZnO infiltrated Kevlar fibres were prepared. Similar to the observations in the previous chapter, these fibres showed improved thermal and UV stability as a consequence of the ZnO-Kevlar hybrid created in the subsurface area. However, contrary to the previous case, the Al<sub>2</sub>O<sub>3</sub> coating increased the modulus of toughness of Kevlar by 10%. Therefore, thanks to unique combination of Al<sub>2</sub>O<sub>3</sub>

coating and ZnO infiltration, mechanically improved and UV resistant Kevlar fibres were created.

Finally, in the last part the electrical and photocatalytic properties of the ZnO-infiltrated Kevlar fibres were analysed. It was theoretically predicted and experimentally proven that due to the interaction between the ZnO and the polymer, the electronic band gap of Kevlar can be reduced. This reduction resulted in increased conductivity and photocurrent generation with visible light illumination. It was confirmed that the conductivity increase arose from the Kevlar-ZnO hybrid as considerable electron flow was maintained after intentional cracking of the exterior ZnO coating. The conductivity was tuned by the number of VPI cycles and by the exposure time. Besides, the shift of the band gap to the visible range was also confirmed by analysing the photocatalytic activity of the hybrid fibres under visible light illumination.

In conclusion, the potential of VPI for the functionalization of Kevlar has been proven and a new combined ALD/VPI process has been developed. The already outstanding mechanical properties of Kevlar have been improved and its main weakness, the thermal and UV sensitivity, have been suppressed. Besides, the electronic band gap of the polymer has been reduced, leading to electrical conductivity and photocatalytic activity under visible light. It can be foreseen that the results presented in this work could be improved and applied to other polymer-precursor combinations.

## Bibliography

1. H. Ghiradella.: Light and Color on the Wing: Structural Colors in Butterflies and Moths. *Appl. Opt.* **30**, 3492 (1991).
2. A. C. Mendes, E. T. Baran, R. L. Reis, and H. S. Azevedo.: Self-Assembly in Nature: Using the Principles of Nature to Create Complex Nanobiomaterials. *Wiley Interdiscip. Rev. Nanomedicine Nanobiotechnology* **5**, 582 (2013).
3. G. Kickelbick.: *Hybrid Materials: Synthesis, Characterization and Applications*; Jhon Wiley & Sons, (2007).
4. C. C. Broomell, M. A. Mattoni, F. W. Zok, and J. H. Waite.: Critical Role of Zinc in Hardening of Nereis Jaws. *J. Exp. Biol.* **209**, 3219 (2006).
5. C. C. Broomell, F. W. Zok, and J. H. Waite.: Role of Transition Metals in Sclerotization of Biological Tissue. *Acta Biomater.* **4**, 2045 (2008).
6. B. W. Cribb, A. Stewart, H. Huang, R. Truss, and B. Noller.: Unique Zinc Mass in Mandibles Separates Drywood Termites from Other Groups of Termites. *Naturwissenschaften* **95**, 433 (2008).
7. Y. Politi, M. Priewasser, E. Pippel, P. Zaslansky, J. Hartmann, S. Siegel, C. Li, F. G. Barth, and P. Fratzl.: A Spider's Fang: How to Design an Injection Needle Using Chitin-Based Composite Material. *Adv. Funct. Mater.* **22**, 2519 (2012).
8. S. W. Werneke, C. Swann, L. A. Farquharson, K. S. Hamilton, and A. M. Smith.: The Role of Metals in Molluscan Adhesive Gels. *J. Exp. Biol.* **210**, 2137 (2007).
9. H. Zhao, C. Sun, R. J. Stewart, and J. H. Waite.: Cement Proteins of the Tube-Building Polychaete *Phragmatopoma Californica*. *J. Biol. Chem.* **280**, 42938 (2005).
10. E. Carrington, and J. M. Gosline.: Mechanical Design of Mussel Byssus: Load Cycle and Strain Rate Dependence. *Am. Malacol. Bull.* **18**, 135 (2004).
11. H. Van Olphen.: Maya Blue : A Clay-Organic Pigment ? *Science (80-. )*. **154**, 645 (1966).
12. J. J. Boon, F. Hoogland, and K. Keune.: Chemical Processes in Aged Oil Paints

- Affecting Metal Soap Migration and Aggregation. *AIC Paint. Spec. Gr. Postprints* **19**, 18 (2007).
13. K. Keune, and J. J. Boon.: Analytical Imaging Studies of Cross-Sections of Paintings Affected by Lead Soap Aggregate Formation. *Stud. Conserv.* **52**, 161 (2007).
  14. L. A. Belfiore, P. Das, and F. Bosse.: Polymers and Their Complexes with Palladium Chloride. *Polym. Phys.* **34**, 2675 (1996).
  15. L. A. Belfiore, E. Indra, and P. Das.: Multi-Functional Coordination Crosslinks in Poly(Vinylamine) Complexes with Cobalt Chloride. *Macromol. Symp.* **114**, 35 (1997).
  16. H. Berke.: The Invention of Blue and Purple Pigments in Ancient Times. *Chem. Soc. Rev.* **36**, 15 (2007).
  17. W. Xu, K. B. Thapa, Q. Ju, Z. Fang, and W. Huang.: Heterogeneous Catalysts Based on Mesoporous Metal-Organic Frameworks. *Coord. Chem. Rev.* No. October(2017).
  18. S.-M. Lee, E. Pippel, U. Gösele, C. Dresbach, Y. Qin, C. V. Chandran, T. Braäuniger, G. Hause, and M. Knez.: Greatly Increased Toughness of Infiltrated Spider Silk. *Science (80-. )*. **324**, 488 (2009).
  19. T. Suntola, and J. Antson.: Method for Producing Compound Thin Films. 4058430, 1977.
  20. N. P. Dasgupta, X. Meng, J. W. Elam, and A. B. F. Martinson.: Atomic Layer Deposition of Metal Sulfide Materials. *Acc. Chem. Res.* **48**, 341 (2015).
  21. B. S. Lim, A. Rahtu, and R. G. Gordon.: Atomic Layer Deposition of Transition Metals. *Nat. Mater.* **2**, 749 (2003).
  22. J. Hamalainen, M. Ritala, and M. Leskela.: Atomic Layer Deposition of Noble Metals and Their Oxides. *Chem. Mater.* **26**, 786 (2014).
  23. R. W. Johnson, A. Hultqvist, and S. F. Bent.: A Brief Review of Atomic Layer Deposition: From Fundamentals to Applications. *Mater. Today* **17**, 236 (2014).
  24. M. Leskelä, and M. Ritala.: Atomic Layer Deposition Chemistry: Recent Developments and Future Challenges. *Angew. Chemie - Int. Ed.* **42**, 5548 (2003).
  25. S. M. George.: Atomic Layer Deposition: An Overview. *Chem. Rev.* **110**, 111 (2010).

26. M. Leskelä, and M. Ritala.: Atomic Layer Deposition (ALD): From Precursors to Thin Film Structures. *Thin Solid Films* **409**, 138 (2002).
27. T. Yoshimura, S. Tatsuura, and W. Sotoyama.: Polymer Films Formed with Monolayer Growth Steps by Molecular Layer Deposition. *Appl. Phys. Lett.* **59**, 482 (1991).
28. S. M. George, B. Yoon, and A. A. Dameron.: Surface Chemistry for Molecular Layer Deposition of Organic and Hybrid Organic–Inorganic Polymers. *Acc. Chem. Res.* **42**, 498 (2009).
29. M. Ritala, and J. Niinistö.: Industrial Applications of Atomic Layer Deposition. *ECS Trans.* **25**, 641 (2009).
30. W. Niu, X. Li, S. K. Karuturi, D. W. Fam, H. Fan, S. Shrestha, L. H. Wong, and A. I. Y. Tok.: Applications of Atomic Layer Deposition in Solar Cells. *Nanotechnology* **26**, (2015).
31. R. Matero, M. Ritala, M. Leskelä, T. Salo, J. Aromaa, and O. Forsén.: Atomic Layer Deposited Thin Films for Corrosion Protection. *J. Phys. IV* **9**, 493 (1999).
32. J. Lu, K.-B. Low, Y. Lei, J. A. Libera, A. Nicholls, P. C. Stair, and J. W. Elam.: Toward Atomically-Precise Synthesis of Supported Bimetallic Nanoparticles Using Atomic Layer Deposition. *Nat. Commun.* **5**, 1 (2014).
33. M. J. Weber, A. J. M. Mackus, M. A. Verheijen, C. van der Marel, and W. M. M. Kessels.: Supported Core/Shell Bimetallic Nanoparticles Synthesis by Atomic Layer Deposition. *Chem. Mater.* **24**, 2973 (2012).
34. T. M. A.-F. and G. N. Diefeng Gu, Helmut Baumgart.: Synthesis of Nested Coaxial Multiple- Walled Nanotubes by Atomic Layer. *ACS Nano* **4**, 753 (2010).
35. H. Shin, D. K. Jeong, J. Lee, M. M. Sung, and J. Kim.: Formation of TiO<sub>2</sub> and ZrO<sub>2</sub> Nanotubes Using Atomic Layer Deposition with Ultraprecise Control of the Wall Thickness. *Adv. Mater.* **16**, 1197 (2004).
36. N. Pinna, and M. Knez.: *Atomic Layer Deposition of Nanostructured Materials*; Wiley-VCH, (2012).
37. M. Knez.: Diffusion Phenomena in Atomic Layer Deposition. *Semicond. Sci. Technol.* **27**, (2012).
38. C. Z. Leng, and M. D. Losego.: Vapor Phase Infiltration (VPI) for Transforming Polymers into Organic–Inorganic Hybrid Materials: A Critical

- Review of Current Progress and Future Challenges. *Mater. Horiz.* **4**, 747 (2017).
39. S. M. Lee, E. Pippel, O. Moutanabbir, J. H. Kim, H. J. Lee, and M. Knez.: In Situ Raman Spectroscopic Study of Al-Infiltrated Spider Dragline Silk under Tensile Deformation. *ACS Appl. Mater. Interfaces* **6**, 16827 (2014).
40. S. Lee, E. Pippel, O. Moutanabbir, I. Gunkel, T. Thurn-albrecht, and M. Knez.: Improved Mechanical Stability of Dried Collagen Membrane after Metal Infiltration. *Appl. Mater. Interfaces* **2**, 2436 (2010).
41. K. E. Gregorczyk, D. F. Pickup, M. G. Sanz, I. A. Irakulis, C. Rogero, and M. Knez.: Tuning the Tensile Strength of Cellulose through Vapor-Phase Metalation. *Chem. Mater.* **27**, 181 (2015).
42. L. Zhang, A. J. Patil, L. Li, A. Schierhorn, S. Mann, U. Gösele, and M. Knez.: Chemical Infiltration during Atomic Layer Deposition: Metalation of Porphyrins as Model Substrates. *Angew. Chemie Int. Ed.* **48**, 4982 (2009).
43. S. M. Lee, V. Ischenko, E. Pippel, A. Masic, O. Moutanabbir, P. Fratzl, and M. Knez.: An Alternative Route towards Metal-Polymer Hybrid Materials Prepared by Vapor-Phase Processing. *Adv. Funct. Mater.* **21**, 3047 (2011).
44. C. D. McClure, C. J. Oldham, and G. N. Parsons.: Effect of Al<sub>2</sub>O<sub>3</sub> ALD Coating and Vapor Infusion on the Bulk Mechanical Response of Elastic and Viscoelastic Polymers. *Surf. Coatings Technol.* **261**, 411 (2015).
45. K. Dusoë, X. Ye, K. Kisslinger, A. Stein, S.-W. Lee, and C.-Y. Nam.: Ultra-High Elastic Strain Energy Storage in Metal-Oxide-Infiltrated Patterned Hybrid Polymer Nanocomposites. *Nano Lett.* **17**, 7416 (2017).
46. B. Gong, Q. Peng, J. S. Jur, C. K. Devine, K. Lee, and G. N. Parsons.: Sequential Vapor Infiltration of Metal Oxides into Sacrificial Polyester Fibers: Shape Replication and Controlled Porosity of Microporous/Mesoporous Oxide Monoliths. *Chem. Mater.* **23**, 3476 (2011).
47. C.-Y. Nam, A. Stein, and K. Kisslinger.: Direct Fabrication of High Aspect-Ratio Metal Oxide Nanopatterns via Sequential Infiltration Synthesis in Lithographically Defined SU-8 Templates. *J. Vac. Sci. Technol. B, Nanotechnol. Microelectron. Mater. Process. Meas. Phenom.* **33**, 06F201 (2015).
48. E. C. Dandley, P. C. Lemaire, Z. Zhu, A. Yoon, L. Sheet, and G. N. Parsons.: Wafer-Scale Selective-Area Deposition of Nanoscale Metal Oxide Features

- Using Vapor Saturation into Patterned Poly(Methyl Methacrylate) Templates. *Adv. Mater. Interfaces* **4**, 1 (2017).
49. B. Gong, D. H. Kim, and G. N. Parsons.: Mesoporous Metal Oxides by Vapor Infiltration and Atomic Layer Deposition on Ordered Surfactant Polymer Films. *Langmuir* **28**, 11906 (2012).
50. Y. Wang, Y. Qin, A. Berger, E. Yau, C. He, L. Zhang, U. Gösele, M. Knez, and M. Steinhart.: Nanoscopic Morphologies in Block Copolymer Nanorods as Templates for Atomic-Layer Deposition of Semiconductors. *Adv. Mater.* **21**, 2763 (2009).
51. Q. Peng, Y. C. Tseng, S. B. Darling, and J. W. Elam.: Nanoscopic Patterned Materials with Tunable Dimensions via Atomic Layer Deposition on Block Copolymers. *Adv. Mater.* **22**, 5129 (2010).
52. Q. Peng, Y. C. Tseng, S. B. Darling, and J. W. Elam.: A Route to Nanoscopic Materials via Sequential Infiltration Synthesis on Block Copolymer Templates. *ACS Nano* **5**, 4600 (2011).
53. J. J. Kim, H. S. Suh, C. Zhou, A. U. Mane, B. Lee, S. Kim, J. D. Emery, J. W. Elam, P. F. Nealey, P. Fenter, and T. T. Fister.: Mechanistic Understanding of Tungsten Oxide In-Plane Nanostructure Growth *via* Sequential Infiltration Synthesis. *Nanoscale* **10**, 3469 (2018).
54. O. M. Ishchenko, S. Krishnamoorthy, N. Valle, J. Guillot, P. Turek, I. Fechete, and D. Lenoble.: Investigating Sequential Vapor Infiltration Synthesis on Block-Copolymer-Templated Titania Nanoarrays. *J. Phys. Chem. C* **120**, 7067 (2016).
55. J. Yin, Q. Xu, Z. Wang, X. Yao, and Y. Wang.: Highly Ordered TiO<sub>2</sub> Nanostructures by Sequential Vapour Infiltration of Block Copolymer Micellar Films in an Atomic Layer Deposition Reactor. *J. Mater. Chem. C* **1**, 1029 (2013).
56. J. W. Choi, Z. Li, C. T. Black, D. P. Sweat, X. Wang, and P. Gopalan.: Patterning at the 10 Nanometer Length Scale Using a Strongly Segregating Block Copolymer Thin Film and Vapor Phase Infiltration of Inorganic Precursors. *Nanoscale* **8**, 11595 (2016).
57. Y. She, J. Lee, B. T. Diroll, B. Lee, S. Aouadi, E. V. Shevchenko, and D. Berman.: Rapid Synthesis of Nanoporous Conformal Coatings via Plasma-

- Enhanced Sequential Infiltration of a Polymer Template. *ACS Omega* **2**, 7812 (2017).
58. Y.-C. Tseng, Q. Peng, L. E. Ocola, D. A. Czaplewski, J. W. Elam, and S. B. Darling.: Enhanced Polymeric Lithography Resists via Sequential Infiltration Synthesis. *J. Mater. Chem.* **21**, 11722 (2011).
59. Y.-C. Tseng, Q. Peng, L. E. Ocola, D. A. Czaplewski, J. W. Elam, and S. B. Darling.: Etch Properties of Resists Modified by Sequential Infiltration Synthesis. *J. Vac. Sci. Technol. B* **29**, 06FG01 (2011).
60. Y. C. Tseng, Q. Peng, L. E. Ocola, J. W. Elam, and S. B. Darling.: Enhanced Block Copolymer Lithography Using Sequential Infiltration Synthesis. *J. Phys. Chem. C* **115**, 17725 (2011).
61. A. Rahman, M. Liu, and C. T. Black.: Block Copolymer Self Assembly for Design and Vapor-Phase Synthesis of Nanostructured Antireflective Surfaces. *J. Vac. Sci. Technol. B* **32**, 06FE02 (2014).
62. D. Berman, S. Guha, B. Lee, J. W. Elam, S. B. Darling, and E. V. Shevchenko.: Sequential Infiltration Synthesis for the Design of Low Refractive Index Surface Coatings with Controllable Thickness. *ACS Nano* **11**, 2521 (2017).
63. H. I. Akyildiz, M. Lo, E. Dillon, A. T. Roberts, H. O. Everitt, and J. S. Jur.: Formation of Novel Photoluminescent Hybrid Materials by Sequential Vapor Infiltration into Polyethylene Terephthalate Fibers. *J. Mater. Res.* **29**, 2817 (2014).
64. H. I. Akyildiz, K. L. Stano, A. T. Roberts, H. O. Everitt, and J. S. Jur.: Photoluminescence Mechanism and Photocatalytic Activity of Organic-Inorganic Hybrid Materials Formed by Sequential Vapor Infiltration. *Langmuir* **32**, 4289 (2016).
65. L. E. Ocola, D. J. Gosztola, A. Yanguas-Gil, H.-S. Suh, and A. Connolly.: Photoluminescence of Sequential Infiltration Synthesized ZnO Nanostructures. *SPIE Proc.* **9755**, 97552C (2016).
66. L. E. Ocola, A. Connolly, D. J. Gosztola, R. D. Schaller, and A. Yanguas-Gil.: Infiltrated Zinc Oxide in Poly(Methyl Methacrylate): An Atomic Cycle Growth Study. *J. Phys. Chem. C* **121**, 1893 (2017).
67. S. Obuchovsky, I. Deckman, M. Moshonov, T. Segal Peretz, G. Ankonina, T. J.

- Savenije, and G. L. Frey.: Atomic Layer Deposition of Zinc Oxide onto and into P3HT for Hybrid Photovoltaics. *J. Mater. Chem. C* **2**, 8903 (2014).
68. M. Moshonov, and G. L. Frey.: Directing Hybrid Structures by Combining Self-Assembly of Functional Block Copolymers and Atomic Layer Deposition: A Demonstration on Hybrid Photovoltaics. *Langmuir* **31**, 12762 (2015).
69. Y. Yu, Z. Li, Y. Wang, S. Gong, and X. Wang.: Sequential Infiltration Synthesis of Doped Polymer Films with Tunable Electrical Properties for Efficient Triboelectric Nanogenerator Development. *Adv. Mater.* **27**, 4938 (2015).
70. W. Wang, C. Chen, C. Tollan, F. Yang, Y. Qin, and M. Knez.: Efficient and Controllable Vapor to Solid Doping of the Polythiophene P3HT by Low Temperature Vapor Phase Infiltration. *J. Mater. Chem. C* **5**, 2686 (2017).
71. W. Wang, F. Yang, C. Chen, L. Zhang, Y. Qin, and M. Knez.: Tuning the Conductivity of Polyaniline through Doping by Means of Single Precursor Vapor Phase Infiltration. *Adv. Mater. Interfaces* **4**, 1 (2017).
72. W. Wang, C. Chen, C. Tollan, F. Yang, M. Beltrán, Y. Qin, and M. Knez.: Conductive Polymer-Inorganic Hybrid Materials through Synergistic Mutual Doping of the Constituents. *ACS Appl. Mater. Interfaces* **9**, 27964 (2017).
73. M. Panar, P. Avakian, R. C. Blume, K. H. Gardner, T. D. Gierke, H. H. Yang, and E. I. P. De Nemours.: Morphology of Poly ( p-Phenylene Terephthalamide ) Fibers. *J. Polym. Sci. Polym. Phys. Ed.* **21**, 1955 (1983).
74. E. G. Chatzi, and J. L. Koenig.: Morphology and Structure of Kevlar Fibers: A Review. *Polym. Plast. Technol. Eng.* **26**, 229 (1987).
75. Y. Rao, A. J. Waddon, and R. J. Farris.: The Evolution of Structure and Properties in Poly ( p -Phenylene Terephthalamide ) Fibers. *Polymer (Guildf)*. **42**, 5925 (2001).
76. M. R. Roenbeck, E. J. Sandoz-Rosado, J. Cline, V. Wu, P. Moy, M. Afshari, D. Reichert, S. R. Lustig, and K. E. Strawhecker.: Probing the Internal Structures of Kevlar® Fibers and Their Impacts on Mechanical Performance. *Polym. (United Kingdom)* **128**, 200 (2017).
77. D. Ahmed, Z. Hongpeng, K. Haijuan, L. Jing, M. Yu, and Y. Muhuo.: Microstructural Developments of Poly (p-Phenylene Terephthalamide) Fibers during Heat Treatment Process: A Review. *Mater. Res.* **17**, 1180 (2014).

78. DuPont.: *KEVLAR Aramid Fiber: Technical Guide*; (2011).
79. N. J. Abbott, J. G. Donovan, and M. M. Schoppee.: *The Effect of Temperature and Strain Rate on the Tensile Properties of Kevlar and PBI Yarns*; (1974).
80. H. Zhang, J. Zhang, J. Chen, X. Hao, S. Wang, X. Feng, and Y. Guo.: Effects of Solar UV Irradiation on the Tensile Properties and Structure of PPTA Fiber. *Polym. Degrad. Stab.* **91**, 2761 (2006).
81. C. X. Wang, M. Du, J. C. Lv, Q. Q. Zhou, Y. Ren, G. L. Liu, D. W. Gao, and L. M. Jin.: Surface Modification of Aramid Fiber by Plasma Induced Vapor Phase Graft Polymerization of Acrylic Acid . I . Influence of Plasma Conditions. *Appl. Surf. Sci.* **349**, 333 (2015).
82. B. Song, L. Meng, and Y. Huang.: Surface Modification of PBO Fiber through Oxygen Plasma Induced Vapor Phase Grafting of Acrylic Acid. *Mater. Lett.* **83**, 118 (2012).
83. P. Katangur, P. K. Patra, and S. B. Warner.: Nanostructured Ultraviolet Resistant Polymer Coatings. *Polym. Degrad. Stab.* **91**, 2437 (2006).
84. S. Kathirvelu, L. D'Souza, and B. Dhurai.: UV Protection Finishing of Textiles Using ZnO Nanoparticles. *Indian J. Fibre Text. Res.* **34**, 267 (2009).
85. A. Gupta.: Improving UV Resistance of High Strength Fibers, North Carolina State University, (2005).
86. X. Xiao, X. Liu, D. Fang, C. Zhang, L. Xia, and W. Xu.: Highly Anti-UV Properties of Silk Fiber with Uniform and Conformal Nanoscale TiO<sub>2</sub> Coatings via Atomic Layer Deposition. *Appl. Mater. Interfaces* **7**, 21326 (2015).
87. W. G.G., C. T.E., and I. P.C.: Putting Function into Fashion: Organic Conducting Polymer Fibres and Textiles. *Fibers Polym.* **8**, 135 (2007).
88. E. Gasana, P. Westbroek, J. Hakuzimana, K. De Clerck, G. Priniotakis, P. Kiekens, and D. Tseles.: Electroconductive Textile Structures through Electroless Deposition of Polypyrrole and Copper at Polyaramide Surfaces. *Surf. Coatings Technol.* **201**, 3547 (2006).
89. J. Lee, H. Kwon, J. Seo, S. Shin, J. H. Koo, C. Pang, S. Son, J. H. Kim, Y. H. Jang, D. E. Kim, and T. Lee.: Conductive Fiber-Based Ultrasensitive Textile Pressure Sensor for Wearable Electronics. *Adv. Mater.* **27**, 2433 (2015).
90. D. Kincal, A. Kumar, A. D. Child, and J. R. Reynolds.: Conductivity Switching

- in Polypyrrole-Coated Textile Fabrics as Gas Sensors. *Synth. Met.* **92**, 53 (1998).
91. B. Engineering.: *Conjugated Polymer-Based Conductive Fibers for Smart Textile Applications*; Vol. 46.
  92. C. Xiang, W. Lu, Y. Zhu, Z. Sun, Z. Yan, C. C. Hwang, and J. M. Tour.: Carbon Nanotube and Graphene Nanoribbon-Coated Conductive Kevlar Fibers. *ACS Appl. Mater. Interfaces* **4**, 131 (2012).
  93. B. K. Little, Y. Li, V. Cammarata, and B. R.: Metallization of Kevlar Fibres with Gold. *Appl. Mater. Interfaces* **3**, 1965 (2011).
  94. Y. Gao, K. Sim, S. Sun, Z. Chen, J. Song, and C. Yu.: Crack-Insensitive Wearable Electronics Enabled Through High-Strength Kevlar Fabrics. **1**, 1 (2015).
  95. X. Zhao, K. Hirogaki, I. Tabata, S. Okubayashi, and T. Hori.: A New Method of Producing Conductive Aramid Fibers Using Supercritical Carbon Dioxide. *Surf. Coatings Technol.* **201**, 628 (2006).
  96. I. Amenabar, S. Poly, W. Nuansing, E. H. Hubrich, A. A. Govyadinov, F. Huth, R. Krutokhvostov, L. Zhang, M. Knez, J. Heberle, A. M. Bittner, and R. Hillenbrand.: Structural Analysis and Mapping of Individual Protein Complexes by Infrared Nanospectroscopy. *Nat. Commun.* **4**, (2013).
  97. I. Azpitarte, A. Zuzuarregui, H. Ablat, L. Ruiz-Rubio, A. López-Ortega, S. D. Elliott, and M. Knez.: Suppressing the Thermal and Ultraviolet Sensitivity of Kevlar by Infiltration and Hybridization with ZnO. *Chem. Mater.* **29**, 10068 (2017).
  98. X. Xu, L. Heng, X. Zhao, J. Ma, L. Lin, and L. Jiang.: Multiscale Bio-Inspired Honeycomb Structure Material with High Mechanical Strength and Low Density. *J. Mater. Chem.* **22**, 10883 (2012).
  99. N. Reddy, and Y. Yang.: Structure and Properties of Chicken Feather Barbs as Natural Protein Fibers. *J. Polym. Environ.* **15**, 81 (2007).
  100. J.-Y. Rho, L. Kuhn-Spearing, and P. Zioupos.: Mechanical Properties and the Hierarchical Structure of Bone. *Med. Eng. Phys.* **20**, 92 (1998).
  101. R. B. Martin.: Determinants of the Mechanical Properties of Bones. *J. Biomech.* **24**, 79 (1991).
  102. C. Y. Yue, G. X. Sui, and H. C. Looi.: Effects of Heat Treatment on the

- Mechanical Properties of Kevlar-29 Fibre. *Compos. Sci. Technol.* **60**, 421 (2000).
103. M. A. Said, B. Dingwall, and A. Gupta.: Investigation of Ultra Violet ( UV ) Resistance for High Strength Fibers. *Adv. Sp. Res.* **37**, 2052 (2006).
104. Y. Wang, and Y. M. Xia.: Experimental and Theoretical Study on the Strain Rate and Temperature Dependence of Mechanical Behaviour of Kevlar Fibre. *Compos. Part A Appl. Sci. Manuf.* **30**, 1251 (1999).
105. R. Orban.: New Metal-Coated Fibers and Fabric Lead to Novel, Practical Products. *J. Ind. Text.* **18**, 246 (1989).
106. D. Price, and D. Allman.: Hydrothermal Synthesis of Zinc Oxide Nanowires on Kevlar Using ALD and Sputtered ZnO Seed Layers. *MRS Proc.* **1178**, 6 (2009).
107. S. E. Atanasov, C. J. Oldham, K. A. Slusarski, J. Taggart-Scarff, S. A. Sherman, K. J. Senecal, S. F. Filocamo, Q. P. McAllister, E. D. Wetzel, and G. N. Parsons.: Improved Cut-Resistance of Kevlar® Using Controlled Interface Reactions during Atomic Layer Deposition of Ultrathin (<50 Å) Inorganic Coatings. *J. Mater. Chem. A* **2**, 17371 (2014).
108. K. Gregorczyk, and M. Knez.: Hybrid Nanomaterials through Molecular and Atomic Layer Deposition: Top down, Bottom up, and in-between Approaches to New Materials. *Prog. Mater. Sci.* **75**, 1 (2016).
109. D. S. Sholl, and J. A. Steckel.: *Density Functional Theory; A Practical Introduction*; Jhon Wiley & Sons, (2002).
110. F. Furche, R. Ahlrichs, C. Hättig, and W. Klopper.: Turbomole. *Wiley Interdiscip. Rev. Comput. Mol. Sci.* **4**, 91 (2014).
111. R. Ahlrichs.: Efficient Evaluation of Three-Center Two-Electron Integrals over Gaussian Functions. *Phys. Chem. Chem. Phys.* **6**, 5119 (2004).
112. F. Weigend.: Accurate Coulomb-Fitting Basis Sets for H to Rn. *Phys. Chem. Chem. Phys.* **8**, 1057 (2006).
113. O. Treutler, and R. Ahlrichs.: Efficient Molecular Numerical Integration Schemes. *J. Chem. Phys.* **102**, 346 (1995).
114. K. Eichkorn, F. Weigend, O. Treutler, and R. Ahlrichs.: Auxiliary Basis Sets for Main Row Atoms and Transition Metals and Their Use to Approximate Coulomb Potentials. *Theor. Chem. Acc.* **97**, 119 (1997).

- 
115. C. Y. Peng, P. Y. Ayala, H. B. Schlegel, and M. J. Frisch.: Using Redundant Internal Coordinates to Optimize Equilibrium Geometries and Transition States. *J. Comput. Chem.* **17**, 49 (1996).
116. J. T. Tanskanen, C. Hägglund, and S. F. Bent.: Correlation Growth Characteristics in Atomic Layer Deposition with Precursor Molecular Structure: The Case of Zinc Tin Oxide. *Chem. Mat.* **556**, 186 (2014).
117. T. Weckman, and K. Laaonen.: Atomic Layer Deposition of Zinc Oxide: Diethyl Zinc Reactions and Surface Saturation from First-Principle. *J. Phys. Chem. C* **120**, 21460 (2016).
118. Q. Shi, L. Ni, Y. Zhang, X. Feng, Q. Chang, J. Meng, X. Li, S. Yuan, J. Li, M. Tian, J. Lin, and B. V. Bruggen.: Poly(p-Phenylene Terephthamide) Embedded in a Polysulfone as the Substrate for Improving Compaction Resistance and Adhesion of a Thin Film Composite Polyamide Membrane. *J. Mater. Chem. A* **5**, 13610 (2017).
119. P. Wang, K. Wang, J. Zhang, and G. Luo.: Preparation of Poly(p-Phenylene Terephthalamide) in a Microstructured Chemical System. *Rsc Adv.* **5**, 64055 (2015).
120. S. Cai, and B. R. Singh.: Identification of Beta -Turn and Random Coil Amide III Infrared Bands for Secondary Structure Estimation of Proteins. *Biophys. Chem.* **80**, 7 (1999).
121. S. Cai, and B. R. Singh.: A Distinct Utility of the Amide III Infrared Band for Secondary Structure Estimation of Aqueous Protein Solutions Using Partial Least Squares Methods. *Biochemistry* **43**, 2541 (2004).
122. B. R. Singh, D. B. Deoliveira, F. Fu, and M. P. Fuller.: Fourier Transform Infrared Analysis of Amide III Bands of Proteins for the Secondary Structure Stimulation. *Biomol. Spectrosc. III* **1890**, 47 (1993).
123. G. M. Cai, and W. D. Yu.: Study on the Thermal Degradation of High Performance Fibers by TG/FTIR and Py-GC/MS. *J. Therm. Anal. Calorim.* **104**, 757 (2011).
124. G. Kim, S. Lee, M. Knez, and P. Simon.: Single Phase ZnO Submicrotubes as a Replica of Electrospun Polymer Fiber Template by Atomic Layer Deposition. *Thin Solid Films* **562**, 291 (2014).

125. X. Liu, and W. Yu.: Evaluating the Thermal Stability of High Performance Fibers by TGA. *J. Appl. Polym. Sci.* **99**, 937 (2006).
126. H. Wang, H. Xie, Z. Hu, D. Wu, and P. Chen.: The Influence of UV Radiation and Moisture on the Mechanical Properties and Micro-Structure of Single Kevlar Fibre Using Optical Methods. *Polym. Degrad. Stab.* **97**, 1755 (2012).
127. X. Liu, W. Yu, and N. Pan.: Evaluation of High Performance Fabric Under Light Irradiation. *J. Appl. Polym. Sci.* **120**, 552 (2011).
128. W. Chen, X. Qian, X. He, and J. Liu.: Enhanced Ultraviolet Resistance of Kevlar Fibers with TiO<sub>2</sub> Films. *Reliab. Maintainab. Saf. 9th Int. Conf.* 1267 (2011).
129. G. N. Parsons, S. E. Atanasov, E. C. Dandley, C. K. Devine, B. Gong, J. S. Jur, K. Lee, C. J. Oldham, Q. Peng, J. C. Spagnola, and P. S. Williams.: Mechanisms and Reactions during Atomic Layer Deposition on Polymers. *Coord. Chem. Rev.* **257**, 3323 (2013).
130. J. C. Spagnola, B. Gong, S. A. Arvidson, J. S. Jur, S. A. Khan, and G. N. Parsons.: Surface and Sub-Surface Reactions during Low Temperature Aluminium Oxide Atomic Layer Deposition on Fiber-Forming Polymers. *J. Mater. Chem.* **20**, 4213 (2010).
131. L. Konopasek, and J. W. S. Hearle.: Tensile Fatigue Behaviour of Para-Orientated Aramid Fibres and Their Fracture Morphology. *J. Appl. Polym. Sci.* **21**, 2791 (1977).
132. Y. W. Mai, and F. Castino.: Fracture Toughness of Kevlar-Epoxy Composites with Controlled Interfacial Bonding. *J. Mater. Sci.* **19**, 1638 (1984).
133. A. R. Bunsell.: The Tensile and Fatigue Behaviour of Kevlar-49 (PRD-49) Fibre. *J. Mater. Sci.* **10**, 1300 (1975).
134. T. G. Mcnaughton, and K. W. Horch.: Metallized Polymer Fibers as Leadwires and Intrafascicular Microelectrodes. *J. Neurosci. Methods* **70**, 103 (1996).
135. A. Schwarz, J. Hakuzimana, A. Kaczynska, J. Banaszczyk, P. Westbroek, E. McAdams, G. Moody, Y. Chronis, G. Priniotakis, G. De Mey, D. Tseles, and L. Van Langenhove.: Gold Coated Para-Aramid Yarns through Electroless Deposition. *Surf. Coatings Technol.* **204**, 1412 (2010).
136. Y. Qin, X. Wang, and Z. L. Wang.: Microfibre-Nanowire Hybrid Structure for Energy Scavenging. *Nature* **451**, 809 (2008).

137. Y. Li, X. Y. Cheng, M. Y. Leung, J. Tsang, X. M. Tao, and M. C. W. Yuen.: A Flexible Strain Sensor from Polypyrrole-Coated Fabrics. *Synth. Met.* **155**, 89 (2005).
138. P. N. Bartlett, P. B. M. Archer, and S. K. Ling-Chung.: Conducting Polymer Gas Sensors Part I: Fabrication and Characterization. *Sensors and Actuators* **19**, 125 (1989).
139. J. Wu, D. Zhou, C. O. Too, and G. G. Wallace.: Conducting Polymer Coated Lycra. *Synth. Met.* **155**, 698 (2005).
140. F. Kayaci, C. Ozgit-Akgun, I. Donmez, N. Biyikli, and T. Uyar.: Polymer-Inorganic Core-Shell Nanofibers by Electrospinning and Atomic Layer Deposition: Flexible Nylon-ZnO Core-Shell Nanofiber Mats and Their Photocatalytic Activity. *ACS Appl. Mater. Interfaces* **4**, 6185 (2012).
141. B. Gong, Q. Peng, J. S. Na, and G. N. Parsons.: Highly Active Photocatalytic ZnO Nanocrystalline Rods Supported on Polymer Fiber Mats: Synthesis Using Atomic Layer Deposition and Hydrothermal Crystal Growth. *Appl. Catal. A Gen.* **407**, 211 (2011).
142. H. R. Pant, D. R. Pandeya, K. T. Nam, W. il Baek, S. T. Hong, and H. Y. Kim.: Photocatalytic and Antibacterial Properties of a TiO<sub>2</sub>/Nylon-6 Electrospun Nanocomposite Mat Containing Silver Nanoparticles. *J. Hazard. Mater.* **189**, 465 (2011).
143. B. Muktha, G. Madras, T. N. Guru Row, U. Scherf, and S. Patil.: Conjugated Polymers for Photocatalysis. *J. Phys. Chem. B* **111**, 7994 (2007).
144. X. Zheng, A. J. Cohen, P. Mori-Sánchez, X. Hu, and W. Yang.: Improving Band Gap Prediction in Density Functional Theory from Molecules to Solids. *Phys. Rev. Lett.* **107**, 1 (2011).
145. U. Salzner, J. B. Lagowski, P. G. Pickup, and R. A. Poirier.: Design of Low Band Gap Polymers Employing Density Functional Theory-Hybrid Functionals Ameliorate Band Gap Problem. *J. Comput. Chem.* **18**, 1943 (1997).
146. Y. Takahashi, M. Kanamori, A. Kondoh, H. Minoura, and Y. Ohya.: Photoconductivity of Ultrathin Zinc Oxide Films. *J. Appl. Phys.* **33**, 6611 (1994).
147. G. Heiland.: Photoconductivity of Zinc Oxide as a Surface Phenomenon. *J. Phys. Chem. Solids* **22**, 227 (1961).

148. Q. Zhu, and C. Xie.: Thickness Dependent Photoelectric Responses of ZnO Nanoparticle Films. In *Contributed Papers from Materials Science & Technology (MS&T) 2015*; (2015); pp 1697–1704.
149. J. Yu, and X. Yu.: Hydrothermal Synthesis and Photocatalytic Activity of Zinc Oxide Hollow Spheres. *Environ. Sci. Technol.* **42**, 4902 (2008).
150. W. Ho, J. C. Yu, and S. Lee.: Low-Temperature Hydrothermal Synthesis of S-Doped TiO<sub>2</sub> with Visible Light Photocatalytic Activity. *J. Solid State Chem.* **179**, 1171 (2006).
151. L. Zheng, Y. Zheng, C. Chen, Y. Zhan, X. Lin, Q. Zheng, K. Wei, and J. Zhu.: Network Structured SnO<sub>2</sub>/ZnO Heterojunction Nanocatalyst with High Photocatalytic Activity. *Inorg. Chem.* **48**, 1819 (2009).
152. J. Mu, C. Shao, Z. Guo, Z. Zhang, M. Zhang, P. Zhang, B. Chen, and Y. Liu.: High Photocatalytic Activity of ZnO-Carbon Nanofiber Heteroarchitectures. *ACS Appl. Mater. Interfaces* **3**, 590 (2011).

## List of publications

1. K. E. Gregorczyk, D. F. Pickup, M. G. Sanz, **I. A. Irakulis**, C. Rogero, and M. Knez.: Tuning the Tensile Strength of Cellulose through Vapor-Phase Metalation. *Chem. Mater.* **27**, 181 (2015).
2. L. Ruiz-Rubio, **I. Azpitarte**, N. García-Huete, J. M. Laza, J. L. Vilas, and L. M. León.: Solvent and Relative Humidity Effect on Highly Ordered Polystyrene Honeycomb Patterns Analyzed by Voronoi Tessellation. *J. Appl. Polym. Sci.* **133**, 1 (2016).
3. **I. Azpitarte**, A. Zuzuarregui, H. Ablat, L. Ruiz-Rubio, A. López-Ortega, S. D. Elliott, and M. Knez.: Suppressing the Thermal and Ultraviolet Sensitivity of Kevlar by Infiltration and Hybridization with ZnO. *Chem. Mater.* **29**, 10068 (2017).
4. M. Fenero, J. Palenzuela, **I. Azpitarte**, M. Knez, J. Rodríguez, and R. Tena-Zaera.: Laponite-Based Surfaces with Holistic Self-Cleaning Functionality by Combining Antistatics and Omniphobicity. *ACS Appl. Mater. Interfaces* **9**, 39078 (2017).
5. **I. Azpitarte**, and M. Knez.: Vapor Phase Infiltration: From a Bioinspired Process to Technologic Application, a Prospective Review. *MRS Commun.* **1** (2018).



## Acknowledgements

I am deeply grateful to my supervisor Prof. Mato Knez for all his kindness, help and support. Thank you very much for believing in me since the beginning and for being always willing to listen to my crazy ideas. You were always able to cheer me up in the toughest moments. A ten minutes talk with you has always been enough for not giving up. I would not be writing these final lines without your support. You taught me plenty of things, not only about science but also about life. This thesis is as mine as yours.

I would also like to thank Dr. Ana Zuzuarregui for all the help and enthusiasm at the first steps of my thesis. Laborategian pasatutako ordu luzeak arintzea eskertzen dizut. Zugatik ez balitz, ez nituzke laginak prestatzen eta propietate mekanikoak neurtzen emandako arratsalde luzeak gaindituko. Eskerrik asko irakatsitako guztiagatik eta eskainitako laguntzagatik.

I am really thankful to Dr. Leire Ruiz-Rubio for being always willing to help me. Has sido una persona clave en mi carrera desde mucho antes del doctorado. Me siento afortunada de haber contado con tu ayuda y apoyo desde el principio y no sé como agradecerle todo lo que has hecho por mí.

I am also grateful to past and present members of the nanomaterials group for the great working atmosphere in the lab. I have to specially mention Mikel Beltrán and Sarai Garcia for the good moments we have shared in the lab. Gracias Mikel por ser el mejor técnico que podía haber tenido. Siempre dispuesto a ayudar en todo lo que podías, has solucionado todos los inconvenientes que me han surgido. Y a ti Sarai gracias por las risas y conversaciones en el laboratorio y sobre todo gracias por estar siempre dispuesta a sentarte a tomar un café y escucharme. Eta Unai Carmona doktorea, ezin dot lankideetaz berba ein zu aipatu barik. Nanogunen pasatako urteak ezin dotaz zu barik imaginatu. Eskerrik asko regaliz infusio baten konpanion

eukindako momentu on guztiengatik. Eskerrik asko momentu txarretan gauzak erlatibizatzen erakusteagatik eta, batez be, eskerrik asko nire lagune izategatik.

I also have to thank all nanopeople community for the great time I have had with all of you. The conversations and moments we have shared in the “hamaiketako” always made my day.

Atal hau ezin dot amaitu, hartzen doten erabakia hartuta ere, beti ni laguntzeko prest dauzenak aipatu barik. Nire familia. Aita, Ama eta Irati badakit doktoretza egiten pasatu dotezan urte hauetan zuentzako ere momentu gogorak egon direla. Eskerrik asko beti nire erabakiak babesteagatik, behar izan dotenean hor egoteagatik. Eskerrik asko niretzat zaila zan momentuetan ere, nitan sinisteagatik. Eskerrik asko honarte heltzen lagundu izanagatik. Zuri Izadi, noiz bait irakurriko dozun esperantzarekin, eskerrik asko zure besarkada bategaz dana konpontzeagatik. Azkenik, nire momentu txar gehienak ikusi eta jasan arren, hor jarraitzen deuenari. Mikel zuri, zelan eskertu dana beltz ikusten nebanean ere irribarre bat atarateko gai izatea. Eskerrik asko nire gora-beherak jasateagatik eta beti aurrera jarraitzeko indarra emoteagatik.

Eskerrik asko bihotz-bihotzez.

